OMI Algorithm Theoretical Basis Document

Volume IV

OMI Trace Gas Algorithms

Edited by
K. Chance
Smithsonian Astrophysical Observatory
Cambridge, MA, USA

ATBD-OMI-02, Version 1.0, September 2001

Table of Contents

PREFACE **5**
Background *5*
Purpose of the ATBD *5*
Contents of the ATBDs *5*
Summary *6*

1. OVERVIEW **7**
1.1. NO_2, HCHO, BrO, AND OClO 8
1.2. SO_2 11
1.3. REFERENCES 13

2. NO_2 ..... **15**
2.1. INTRODUCTION 15
2.2. ALGORITHM DESCRIPTION 16
2.2.1. Slant column measurements 17
Radiance fitting by DOAS *17*
Reference spectra *18*
Fitting window *20*
2.2.2. Air mass factors and vertical column abundances 21
Air mass factor calculations *21*
Binning and smoothing *22*
Correction of the vertical column for polluted conditions *23*
2.2.3. Outputs 24
2.2.4. Validation 25
2.3. ERROR ANALYSIS 25
2.4. ACKNOWLEDGMENTS 26
2.5. REFERENCES 27
2.A. APPENDIX A: AIR MASS FACTORS OVER CLOUDED SCENES 29
2.A.1. Effects of clouds and aerosols 29
2.A.2. Definitions 29
2.A.3. Unpolluted and polluted profiles 30
2.A.4. Application 30
2.A.5. Cloudless case 30
2.A.6. Clouds 31
2.A.7. Temperature correction 32
2.B. APPENDIX B: ERROR ANALYSIS DETAILS 33
2.B.1. Slant column density 33
2.B.2. Air Mass Factor 34
2.C APPENDIX C: DATA PRODUCTS TABLE AND DATA PRODUCT DEPENDENCIES 36

3. HCHO **37**
3.1. SLANT COLUMN MEASUREMENTS 38
3.1.1. Nonlinear least-squares fitting 39
3.1.2. Re-calibration of wavelength scales 40
3.1.3. Reference spectra 41
3.1.4. Common-mode correction 43
3.1.5. Radiance fitting: BOAS (baseline option) 43
3.1.6. Radiance fitting: DOAS (non-baseline option) 44
3.2. AIR MASS FACTORS AND VERTICAL COLUMN ABUNDANCES 44
3.3. ERROR ESTIMATES 45
3.4. OUTPUTS 46

3.5. VALIDATION 46
3.6. REFERENCES 47

4. SO_2 49
4.1. INTRODUCTION 49
4.1.1. Volcanic SO_2 50
4.1.2. Anthropogenic SO_2 50
4.1.3. Volcanic ash measurements 50
4.2. SELECTION OF OPTIMUM SPECTRAL REGION 51
4.3. DETAILED DESCRIPTIONS OF THE SO_2 ALGORITHM 52
4.3.1. Inversion strategy 52
4.3.2. Forward model 53
4.3.3. Inversion technique 54
4.4. ERROR ANALYSIS 55
4.4.1. Checking consistency of the forward model with the measurements 55
4.4.2. Estimating retrieval error 55
4.4.3. Correction for Ring effect 57
4.4.4. Correction for volcanic ash 57
4.5. OUTPUTS 57
4.6. VALIDATION 58
4.7. REFERENCES 59

5. BRO 61
5.1. SLANT COLUMN MEASUREMENTS 62
5.1.1. Nonlinear least-squares fitting 62
5.1.2. Re-calibration of wavelength scales 63
5.1.3. Reference spectra 64
5.1.4. Common-mode correction 64
5.1.5. Radiance fitting: BOAS (baseline option) 65
5.1.6. Radiance fitting: DOAS (non-baseline option) 66
5.2. AIR MASS FACTORS AND VERTICAL COLUMN ABUNDANCES 66
5.3. ERROR ESTIMATES 67
5.4. OUTPUTS 68
5.5. VALIDATION 68
5.6. REFERENCES 68

6. OCLO 71
6.1. SLANT COLUMN MEASUREMENTS 71
6.1.1. Nonlinear least-squares fitting 71
6.1.2. Re-calibration of wavelength scales 72
6.1.3. Reference spectra 73
6.1.4. Common-mode correction 73
6.1.5. Radiance fitting: BOAS (baseline option) 74
6.1.6. Radiance fitting: DOAS (non-baseline option) 75
6.2. AIR MASS FACTORS AND VERTICAL COLUMN ABUNDANCES 75
6.3. ERROR ESTIMATES 75
6.4. OUTPUTS 76
6.5. VALIDATION 76
6.6. REFERENCES 77

Preface

Preface to the four OMI-EOS Algorithm Theoretical Basis Documents (ATBDs) for the Ozone Monitoring Instrument (OMI), to be launched mid-2003 on NASA's EOS-Aura satellite

Background

OMI-EOS is a Dutch-Finnish ozone monitoring instrument that will fly on NASA's Aura Mission, part of the Earth Observation System (EOS). Since Aura's purpose is to carry out extensive studies of the Earth's atmosphere, OMI's measurements of ozone columns and profiles, aerosols, clouds, surface UV irradiance, and the trace gases NO_2, SO_2, HCHO, BrO, and OClO fit well into the Aura mission goals. A wide-swath, nadir-viewing, near UV-visible spectrograph, OMI draws heavily on European experience in the atmospheric research instruments GOME (on ERS-2), SCIAMACHY (to be launched later in 2001 on Envisat), and GOMOS (also onboard Envisat).

Purpose of the ATBD

This set of four OMI-EOS Algorithm Theoretical Basis Documents (ATBDs), is intended to present a detailed picture of the instrument and the retrieval algorithms used to derive atmospheric information from the instrument's measurements, so that there is a clear understanding of the results, within the community of OMI scientists, within the Aura Science Team, and among the atmospheric community at large. Each of the chapters of the four ATBDs is written by scientists responsible for the development of the algorithms presented.

These ATBDs will be presented to a group of expert reviewers recruited mainly from the atmospheric research community outside Aura. The results — critiques and recommendations — of the reviewers study of the ATBD will be presented at an Aura meeting, currently scheduled for 5 November 2001. Since changes to the instrument and the Level 0 to 1B processing have a potential for significant cost and schedule impact, the first ATBD is presented for purposes of comment and information. However, progression to the writing of acceptable, operational software for the algorithms for which the data products will be archived in the DAAC (Distributed Active Archive Centre) at NASA's EOSDIS in the other three ATBDs, depends on the approval of the ATBD by the Aura Mission Scientist.

Contents of the ATBDs

ATBD 1 contains a general description of the instrument and its measurement modes. In addition, there is a presentation of the Level 0 to 1B algorithms which convert instrument counts to calibrated radiances, ground and in-flight calibration, and the flight operations needed to collect science data. It is critical that this is well understood by the developers of the higher level processing, as they must know exactly what has been accounted for (and how), and what has not been considered in the Level 0 to 1B processing.

ATBD 2 covers the ozone products. Although OMI is nadir-viewing, this does not limit its output to vertical columns. Rather, because its output is a continuous, moderate-resolution spectrum that includes the range of ozone absorption, it is possible to develop an algorithm for vertical profile as well. The continuous spectrum also makes it possible to use a DOAS (Differential Optical Absorption Spectroscopy) technique developed in connection with GOME, flying on ERS-2. At the same time, an improved version of the TOMS total ozone column algorithm — developed and used successfully over 3 decades — will be used on OMI data. Rounding out the group of four algorithms in this ATBD is a separate, independent estimate of

tropospheric column ozone, using an improved version of the Tropospheric Ozone Residual (TOR) and cloud slicing methods developed for TOMS.

ATBD 3 presents retrieval algorithms for producing the aerosols, clouds, and surface UV radiation products. Retrieval of aerosol optical thickness and aerosol type is presented. Aerosols are of interest because they play an important role in tropospheric pollution and climate change.

The cloud products include cloud top height and effective cloud fraction, both of which are essential, for example, in retrieving the trace gas vertical columns accurately. Effective cloud fraction is obtained by comparing measured reflectance with the expected reflectance from a cloudless pixel and reflectance from a fully cloudy pixel with a Lambertian albedo of 0.8.

On the other hand, two complementary algorithms are presented for cloud-top height (or pressure). One uses a DOAS method, applied to the O_2–O_2 absorption band around 477 nm, while the other uses the filling-in of selected Fraunhofer lines in the range 352-398 nm due to rotational Raman scattering.

Surface UV irradiance is important because of its damaging effects on human health, and on terrestrial and aquatic ecosystems. OMI will extend the long, continuous record produced by TOMS.

ATBD 4 presents the retrieval algorithms for the "additional" trace gases that OMI will be able to monitor: NO_2, SO_2, HCHO, BrO, and OClO. These gases are of interest both because of their respective roles in atmospheric chemistry, as well as their potential for pollution. Extensive experience with GOME has produced spectral fitting techniques used in these newly developed retrieval algorithms, each adapted to the specific characteristics of OMI and the particular molecule in question.

Summary

Individually, the four OMI-EOS ATBDs present in detail how each of OMI's data products are produced. Together they demonstrate the important contributions OMI makes to addressing Aura's scientific questions.

P.F. Levelt (KNMI, The Netherlands)	*Principal Investigator*
G.H.J. van den Oord (KNMI, The Netherlands)	*Deputy PI*
E. Hilsenrath (NASA/GSFC, USA)	*Co-PI*
G.W Leppelmeier (FMI, Finland)	*Co-PI*
P.K. Bhartia (NASA/GSFC, USA)	*US ST Leader*

1. Overview

K. Chance, T.P. Kurosu, and L.S. Rothman
Smithsonian Astrophysical Observatory
Cambridge, MA, USA

OMI - the Ozone Monitoring Instrument on EOS Aura - provides ozone measurements to complement the other species measurements from Aura, following on the heritage of the TOMS and SBUV instruments. In addition, it provides enhanced information on the vertical distribution of atmospheric ozone, including the tropospheric burden, clouds, radiation, and surface UV information, and measurements of a number of additional trace gases. The data products for the trace gases NO_2, HCHO, SO_2, BrO, and OClO are the subject of this volume of the OMI Algorithm Theoretical Basis Document (ATBD).

The OMI trace gases have all been measured from the ground using UV/visible spectroscopy. NO_2 and SO_2 were measured from space, by the SAGE and the TOMS/SBUV instruments, respectively, using discrete wavelength bands. Measurements of the entire suite of molecules were proposed for the SCIAMACHY and GOME instruments, measuring the full UV/visible spectrum at moderate resolution [*Chance et al.*, 1991; *Burrows et al.*, 1993]. All species have now been successfully measured in the nadir geometry by the GOME instrument: NO_2 vertical column abundances are retrieved operationally, while the other gases (and additional determinations of NO_2, including total column abundances and tropospheric abundances) are retrieved in research by a number of European (*e.g., Burrows et al*., [1999]) and U.S. groups (*e.g.,* the SAO). Anticipated trace gas data products from OMI are summarized in Table 1.

Table 1.1 OMI Trace Gas Data Product Summary

Product	Temporal Resolution	Horizontal Resolution::Coverage[1]
NO_2 vertical column (cm^{-2})	Once/day	26×48 km::GD
HCHO vertical column (cm^{-2})	Once/day	13×24 km::GD
SO_2 vertical column (cm^{-2})	Once/day	13×48 km::GD
BrO vertical column (cm^{-2})	Once/day	13×24 km::GD
OClO slant column (cm^{-2})	Once/day	26×48 km::V
[1]G represents global coverage, D daylight, and V vortex		

In this chapter we summarize the procedures used to obtain slant column densities (N_s) and vertical column densities (N_v) for NO_2, HCHO, SO_2, BrO, and OClO from measured OMI spectral radiances and irradiances. The back scattered radiances and solar irradiances, along with ancillary data are used as inputs to the algorithms. Column density values will be archived for each OMI pixel location and will constitute the basic level 2 outputs from the algorithms. Troposphere columns will also be included as outputs, wherever they are determined to contribute significantly to the total.

OMI makes nadir measurements of the Earth's back scattered ultraviolet radiation at spectral resolution of ~0.42 nm in the UV-1 channel (which may be used for part of the SO_2

retrieval), ~0.45 nm in the UV-2 channel, the spectral region where HCHO, BrO, and OClO are measured and the bulk of the SO_2 information is obtained, and ~0.63 nm in the visible channel, where NO_2 is measured. OMI spatial resolution is selectable among a global mode and spectral and spatial zoom-in modes. In global mode, for the UV-2 and visible channels, the spatial resolution is 13 km along-track·24 km across-track at nadir. The full swath width is 2594 km. In both zoom-in modes, the spatial resolution is 13·13 km^2 at nadir. In the spectral zoom-in mode, the wavelength range is reduced to 306-364 nm plus 350-432 nm. For the spatial zoom-in mode all wavelengths are present, but the swath width is reduced to 725 km. The smaller ground pixels in the zoom-in modes will greatly improve our ability to measure smaller atmospheric features, such as enhanced tropospheric NO_2 and HCHO and details of SO_2 sources. Most importantly for geophysics, the OMI instrument will have complete spatial coverage, for the global and the spectral zoom-in modes, with reasonably-sized ground pixels. In contrast, the standard GOME swath provides 40 km along-track·320 km across-track spatial resolution, with 3-day global coverage [*European Space Agency*, 1995].

Trace gas slant column densities are determined by measuring the vibrational structure in molecular electronic bands that occur within the OMI wavelength range: **NO_2** $\tilde{A}\ ^2B_1 \leftarrow \tilde{X}\ ^2A_1$; **HCHO** $\tilde{A}\ ^1A'' \leftarrow \tilde{X}\ ^1A_1$; **$SO_2$** $\tilde{A}\ ^1B_1 \leftarrow \tilde{X}\ ^1A_1$; **BrO** $A\ ^2\Pi_{3/2} \leftarrow X\ ^2\Pi_{3/2}$; and **OClO** $\tilde{A}\ ^2A_2 \leftarrow \tilde{X}\ ^2B_1$. Extensive rotational structure is present in the spectra of HCHO, SO_2, and BrO, but it is not resolvable at the OMI resolution. The OClO band exhibits a gradual onset of broadening by predissociation in the OMI wavelength region, although it is not resolved by OMI in the wavelength window where the absorption is sufficiently strong to be measured.

Trace gas retrieval algorithms are basically of two types, distinguished by those which can normally be analyzed assuming that the scattering and broadband (i.e., O_3 Hartley band) interfering absorption contributions to the measured radiance may be approximated as constant over the spectral fitting window, so that the slant column fitting and the erection to determine vertical column abundances may be separated (NO_2, HCHO, BrO, and OClO) and that which must often take into account the variation of these contributions over the spectral fitting window during the retrieval process (SO_2). For each of the gases measured, the data product is determined from a wavelength window that is optimized for the particular gas. Experience with fitting GOME spectra, as well as with other atmospheric field measurements of spectra, is that attempts to fit wider spectral windows comprehensively for multiple species determinations often leads to inferior results.

1.1. NO_2, HCHO, BrO, and OClO

The intrinsic atmospheric spectrum measured by OMI can be approximated as

$$I(\lambda) = AE(\lambda)e^{-N_{s1}\sigma_1(\lambda)} \cdots e^{-N_{sn}\sigma_n(\lambda)} + Higher\text{-}OrderTerms\ , \qquad [1\text{-}1]$$

where I is the back scattered radiance, A is the albedo (including scattering contributions), E is the Fraunhofer source spectrum (irradiance), the N_{si} are column abundances over the measurement path line-of-sight (``slant column abundances''), the σ_i are absorption cross sections, and the higher-order terms (hereafter *"HOT"*) may be modeled as a polynomial to account for wavelength dependence of the albedo.

The first step in each of the trace gas algorithms for these four molecules is to determine the slant column abundances, for the desired product as well as for the interfering species. This may be accomplished by several methods, including direct fitting of I by synthesizing it beginning with E, fitting to the logarithm of I/E, and fitting to a high-pass filtered version of the logarithm of I/E:

$$H\left[ln(I/E)\right] = -H(-c_1\sigma_1) - \cdots - H(-c_n\sigma_n) + HOT \qquad [1\text{-}2]$$

where H denotes the (optional) high-pass filtering.

Rayleigh scattering is the major contribution to the radiative transfer problem that must be addressed to determine vertical column abundances from slant column abundances, as described below. The analysis to determine slant column abundances must also take into account the fact that, for the wavelength range of OMI trace gas measurements, 4% of the Rayleigh scattering is inelastic (the "Ring effect") and is thus Raman scattered by the predominantly N_2 and O_2 molecular scatterers. This results in an additional spectral component, which, to the lowest approximation, is the convolution of the Fraunhofer and rotational Raman spectra. (The effects of higher-order corrections must be evaluated in detail during algorithm development for the individual trace gases. These include multiple scattering and the modification of the Fraunhofer source spectrum by absorption of atmospheric gases before Raman scattering has occurred.) Ring effect corrections are included as additional fitting terms:

$$I(\lambda) = AE(\lambda)e^{-N_{s1}\sigma_1(\lambda)}\cdots e^{-N_{sn}\sigma_n(\lambda)} + c_{R_1}\sigma_{R_1} + c_{R_2}\sigma_{R_2} + HOT \qquad [1\text{-}3]$$

$$H\left[ln(I/E)\right] = -N_{s1}H(\sigma_1) - \cdots - N_{sn}H(\sigma_n) + c_{R1}H(\sigma_{R1}/F) + c_{R2}H(\sigma_{R2}/F) + HOT, \qquad [1\text{-}4]$$

where two Ring effect correction terms σ_{R1}, σ_{R2} are shown (either one or two terms will generally be included, the second term being a correction for absorption by atmospheric gases - usually O_3 - before the Rayleigh scattering has occurred). The higher-order terms in this case include further terms in the expansion of $\ln[(I + c_R\,\sigma_R) / E]$.

Experience with the fitting of GOME back scattered UV/visible spectra has shown that it may be desirable to include improved wavelength calibration directly in fitting algorithms. The spectral correlation between $I(\lambda)$ and $E(\lambda)$ in the individual fitting windows is substantially improved over the wavelength calibration obtained in the level 0-1 processing [*Caspar and Chance*, 1997], which leads to significant improvement in the trace gas fitting. Additionally, the algorithms include modeling of the instrument transfer function and fitting to low-frequency closure terms to account for the wavelength dependence of the albedo as well as instrument imperfections [*Langley and Abbot*, 1900].

The selection of the optimal fit window must maximize the sensitivity of the retrieval to the target absorption signatures, while minimizing errors from geophysical and instrument-related spectral features. A summary of the important considerations in selecting a wavelength range for the window include:

- Locating regions of maximum amplitude in the structures of the cross sections for the target gas;
- Avoiding overlap with strong atmospheric spectral features from interfering species, including parts of the Raman scattering (Ring) spectrum;
- Avoiding regions containing spectral structures of instrumental origin;
- Choosing as wide a window as possible to maximize the number of sampling points;
- Selecting a region of the target spectrum that minimizes sensitivity of the measurement to the temperature (especially true for NO_2).

The level 2 trace gas data products are all vertical column abundances, except in case of OClO, which is expected to occur only at high solar zenith angles and is currently only envisaged as a slant column data product. The amplitudes of the spectral structures measured

along the OMI line-of-sight determine the fitting to obtain slant column abundances. These must be corrected to take into account measurement geometry, the dilution in the spectra caused by Rayleigh scattering of the Fraunhofer source spectrum (for most measurement geometries, a major effect of Rayleigh scattering is to reduce the effect path of the back scattered light measured at the satellite in comparison to the geometric path, although in a few circumstances Rayleigh scattering may increase the effective path and thus amplify the signal) and obscuration by clouds and aerosols (in some instances aerosol scattering may also amplify the spectral signals), in order to derive vertical column abundances. This will be accomplished by the use of pre-calculated air mass factors (*M*s). *M* for gas *i* is defined as

$$M = N_{si} / N_{vi} \qquad [\ 1\text{-}5\ ]$$

where N_{si} is the slant column abundance and N_{vi} is the vertical column abundance. Vertical column abundances are then simply determined as

$$N_{vi} = N_{si} / M_i. \qquad [\ 1\text{-}6\ ]$$

The algorithms for NO_2, HCHO, BrO, and OClO assume optically thin absorption and Rayleigh scattering, which does not vary significantly over the fitting window. Air mass factors are calculated using a radiative transfer model [*Dave*, 1965; *De Haan et al.*, 1987; *Stammes et al.*, 1989; *Stammes*, 2001; *Spurr et al.*, 2001]. For a given fit window, they are functions of viewing zenith angle, solar zenith angle, surface albedo, cloud parameters, and the constituent profile. Some of these parameters include latitudinal and seasonal effects, which must be considered during the OMI validation. Cloud height and cloud fraction will be OMI data products from other investigations.

*M*s for stratospheric components of the gases considered here are well determined by measurement geometry and climatological vertical distribution profiles. *M*s for the tropospheric components are more problematic for two reasons: (1) The distributions are substantially more variable; (2) The Rayleigh scattering contribution to the *M* is relatively more important because of the greater atmospheric density. For tropospheric measurements, higher-level products will require further processing to take additional geophysical knowledge about measured distributions into account. An example of this is processing of the NO_2 level 2 data products to remove the stratospheric overburden, leaving the tropospheric residual, which may then be further processed to account for the modeled shape of the tropospheric profile and its effect upon the tropospheric component of the *M*. Such processing will be important for many of the trace gas measurements, including the tropospheric components of NO_2 and BrO, and all SO_2 and HCHO measurements, since these are likely to be primarily tropospheric at the OMI measurement sensitivity.

Air mass factors depend on a number of parameters that are input to the radiative transfer. They can be divided into parameters that are assumed a priori:

- Viewing geometry,
- Surface albedo,
- Cloud albedo,
- Terrain height or terrain pressure,

and parameters that must be estimated from chemical or physical knowledge, e.g., climatologies, predictions by assimilation models, and other OMI measurements:

- Altitude distributions in the troposphere have large influences on the air mass factors for NO_2 and HCHO;
- Cloud fraction;
- Cloud height;
- Aerosol optical thickness;
- Ozone profile. Sensitivity studies have shown that including the ozone slant column density as a fit parameter is required, but that the ozone distribution induces a negligible effect on the retrieved NO_2 columns densities.

Clouds have varying effects on air mass factors. Firstly, clouds obscure gas located below the cloud, and thus decrease measurement sensitivity. Secondly, clouds generally increase the sensitivity to gas above clouds, due to the relatively high cloud albedo. In our algorithms, we assume that clouds can be approximated as opaque, Lambertian surfaces. Thin clouds will similarly be treated as opaque surfaces covering only a small part of the pixel, i.e., the effective cloud fraction will be small. Studies into the validity of this assumption for different cloud types, cloud optical thicknesses etc. are currently being performed.

All clouds in a given pixel will be characterized by three parameters: a cloud-top height, a geometrical cloud fraction, and a cloud albedo. Multiple cloud levels are not considered. To calculate the air mass factor for a partly cloudy scene, calculations for fully clouded and fully clear pixels are merged. Under the *independent pixel assumption*, the air mass factor for partly cloudy conditions is given by:

$$M = w\, M_{cloud} + (1 - w)\, M_{clear} \qquad [\,1\text{-}7\,]$$

where M_{cloud} and M_{clear} represent the air mass factors for completely cloudy and clear scenes, respectively, and w is the flux-weighted cloud fraction. We define w as

$$w = \frac{c\, I_{cloud}}{c\, I_{cloud} + (1-c)\, I_{clear}} \qquad [\,1\text{-}8\,]$$

where c is the geometrical cloud fraction, and I_{cloud} and I_{clear} are the respective radiances of cloudy and clear scenes.

Under background conditions, aerosol concentrations are expected to be small, and we assume that the influence of aerosols can be neglected. Where tropospheric gas concentrations are enhanced, aerosol concentrations are often enhanced as well, and the aerosol's effect on the air mass factor may be significant. However, high aerosol concentrations are typically associated with other, larger error sources. Therefore, our preliminary approach will be to neglect the influence of aerosols in the derivation of vertical column densities.

1.2. SO_2

The SO_2 algorithm is sufficiently different from other optically thin trace gas algorithms (NO_2, HCHO, BrO, OClO) that it needs to be addressed separately. A retrieval algorithm for SO_2 must contend with the transient nature and dramatically different scales of atmospheric SO_2 emissions. The important characteristics are:

1) a dynamic range from 0.5 matm-cm to > 1000 matm-cm ($1.4\cdot10^{16}$ to $2.7\cdot10^{19}$ cm^{-2}), making it the dominant absorber in volcanic clouds (which can be optically thick),
2) the location in the boundary layer of the air-pollution SO_2 , and
3) volcanic ash or aerosol interference.

The processing algorithm will produce quantitative data on low level emissions, which are widespread across the northern hemisphere and generally free of ash, and semi-quantitative information on volcanic clouds, which are local in size but can drift over global scales. As no constraints can be p laced on the geographic location of either type of source, all the OMI data will be processed.

The TOMS SO_2 algorithm was developed for sulfur dioxide and ozone discrimination in the near UV spectral region [*Krueger et al.*, 1995; *Krueger et al.*, 2000]. The algorithm uses an atmospheric optical model which characterizes the absorption and scattering processes as four independent pieces of information; two absorption terms for ozone and sulfur dioxide, and two scattering terms for albedo and wavelength dependence. The four TOMS radiance measurements required for closure are selected from the six TOMS bands. Radiative transfer tables are used to determine the optical path for each of the wavelengths. This model has proved very effective with TOMS data even though the channel wavelengths are not well chosen for this purpose. However, the measurement noise level was too high to determine passive volcanic emissions and air pollution. This problem was not present in the GOME data and the DOAS method was able to retrieve anthropogenic SO_2 emissions under wintertime conditions [*Eisinger and Burrows*, 1998].

The OMI SO_2 algorithm is based on the TOMS sulfur dioxide and ozone methods in combination with the DOAS method. We make use of: 1) additional spectral information of OMI, 2) a priori information, and 3) other OMI products (ozone, aerosol, clouds, see other ATBD volumes). Special emphasis is placed on retrieval of small amounts of lower tropospheric SO_2 because of the challenge of the observing conditions and the importance of a database on anthropogenic sulfur dioxide and passive volcanic emissions. Maximum likelihood techniques are employed to make use of all information. It is important to note that ozone and sulfur dioxide must be determined simultaneously for volcanic eruption clouds because of the almost complete overlap of their absorption bands, comparable absorber amounts, and the likelihood that the total ozone column will be modified by the volcanic cloud. Similarly, the optical depth of ash in the cloud needs to be measured and specified for production of radiative transfer tables. The optical properties of ash vary between volcanoes and between eruptions and require laboratory analysis of ash samples for determination. Thus, off-line processing of subsets of data is required to handle the greater complexity of volcanic clouds.

Parallel wavelength sampling with OMI produces a greater S/N than the serial sampling TOMS. Also, OMI measures the full UV spectrum allowing selection of optimum wavelength for a TOMS-like retrieval. These factors can produce an OMI SO_2 retrieval noise level that is a factor of 10 lower than TOMS (~4 DU) and comparable to GOME SO_2 [*Eisinger and Burrows*, 1998]. In addition, the smaller OMI FOV will greatly decrease the minimal detectable SO_2 flux compared with that from GOME.

1.3. References

Burrows, J.P., K.V. Chance, A.P.H. Goede, R. Guzzi, B.J. Kerridge, C. Muller, D. Perner, U. Platt, J.-P. Pommereau, W. Schneider, R.J. Spurr, and H. van der Woerd, *Global Ozone Monitoring Experiment Interim Science Report*, ed. T. D. Guyenne and C. Readings, Report ESA SP-1151, ESA Publications Division, ESTEC, Noordwijk, The Netherlands, ISBN 92-9092-041-6, 1993.

Burrows, J.P., M.Weber, M. Buchwitz, V.V.Rosanov, A.Ladstatter, A. Weissenmayer, A.Richter, R.DeBeek, R.Hoogen,K. Bramstedt, and K.U. Eichmann, The Global Ozone Monitoring Experiment (GOME): Mission concept and first scientific results, *J. Atmos. Sci.,* 56, 151-175, 1999.

Caspar, C., and K. Chance, GOME wavelength calibration using solar and atmospheric spectra, *Proc. Third ERS Symposium on Space at the Service of our Environment*, Ed. T.-D. Guyenne and D. Danesy, European Space Agency publication SP-414, ISBN 92-9092-656-2, 1997.

Chance, K.V., J.P. Burrows, and W. Schneider, Retrieval and molecule sensitivity studies for the Global Ozone Monitoring Experiment and the SCanning Imaging Absorption spectroMeter for Atmospheric CHartographY, *Proc. S.P.I.E., Remote Sensing of Atmospheric Chemistry*, 1491, 151-165, 1991.

Dave, J.V. Multiple scattering in a non-homogeneous, Rayleigh atmosphere, J. Atmos. Sci. 22, 273-279, 1965.

De Haan, J.F., P.B. Bosma, and J.W. Hovenier, The adding method for multiple scattering calculations of polarized light, Astron. Astrophys. 183, 371-391, 1987.

Eisinger, M., and J.P. Burrows, Tropospheric sulfur dioxide observed by the ERS-2 GOME instrument, Geophys. Res. Lett. 25, 4177-4180, 1998.

European Space Agency, The GOME Users Manual, ed. F. Bednarz, European Space Agency Publication SP-1182, ESA Publications Division, ESTEC, Noordwijk, The Netherlands, ISBN-92-9092-327-x, 1995.

Krueger, A.J., L.S. Walter, P.K. Bhartia, C.C. Schnetzler, N. A. Krotkov, I. Sprod, and G.J.S. Bluth, Volcanic sulfur dioxide measurements from the Total Ozone Mapping Spectrometer instruments, J. Geophys. Res. 100, 14,057-14,076, 1995.

Krueger, A.J., S.J. Schaefer, N. Krotkov, G. Bluth, and S. Barker, Ultraviolet Remote Sensing of Volcanic Emissions, in *Remote Sensing of Active Volcanism*, ed. P. Mouginis Mark, J.A. Crisp, and J. H. Fink, Geophysical Monograph 116, American Geophysical Union, Washington, DC, 2000.

Langley, S.P., and C.G. Abbot, *Annals of the Astrophysical Observatory of the Smithsonian Institution*, Vol. 1, pp. 69-75, 1900.

Spurr, R.J.D., T.P. Kurosu, and K. Chance, A linearized discrete ordinate radiative transfer model for atmospheric remote sensing retrieval, J. Quant. Spectrosc. Radiat. Transfer 68, 689-735, 2001.

Stammes, P., J.F. de Haan, and J.W. Hovenier, The polarized internal radiation field of a planetary atmosphere, Astron. Astrophys. 225, 239-259, 1989.

Stammes, P., Spectral radiance modelling in the UV-Visible Range, to appear in *IRS 2000: Current problems in Atmospheric Radiation*, Eds. W.L. Smith and Y.M. Timofeyev, A. Deepak Publ., Hampton (VA), 2001.

2. NO_2

Folkert Boersma[1], Eric Bucsela[2], Ellen Brinksma[1], James F. Gleason[2]
[1]KNMI, [2]NASA-GSFC

2.1. Introduction

Nitrogen dioxide, NO_2, is a critical trace gas in the atmosphere because of its role in the photochemistry of ozone in the stratosphere and troposphere. NO_2 is important for direct destruction of odd-oxygen in the middle stratosphere (Reactions 2.1 - 2.3). NO_2 connects the hydrogen and chlorine chemical families through the production of reservoir species (Reactions 2.4 - 2.7), which are critical to our understanding of lower stratospheric ozone photochemistry.

$$NO + O_3 \rightarrow NO_2 + O_2 \qquad (2\text{-}1)$$
$$NO_2 + O \rightarrow NO + O_2 \qquad (2\text{-}2)$$

Net: $O_3 + O \rightarrow 2\ O_2$ (2-3)

$$NO_2 + OH + M \rightarrow HNO_3 + M \qquad (2\text{-}4)$$
$$NO_2 + HO_2 + M \rightarrow HNO_4 + M \qquad (2\text{-}5)$$
$$NO_3 + NO_2 + M \rightarrow N_2O_5 + M \qquad (2\text{-}6)$$

$$ClO + NO_2 + M \rightarrow ClONO_2 + M \qquad (2\text{-}7)$$

Tropospheric ozone is formed after the photolysis of NO_2 in the tropospheric oxidation of hydrocarbons. Reactions 2.8 - 2.12 illustrate, using CO, how ozone can be produced in the troposphere.

$$CO + OH + (O_2) \rightarrow HO_2 + CO_2 \qquad (2\text{-}8)$$
$$H\ O_2 + NO \rightarrow NO_2 + OH \qquad (2\text{-}9)$$
$$NO_2 + h\nu \rightarrow NO + O\ (h\nu < 600\ nm) \qquad (2\text{-}10)$$
$$O + O_2 + M \rightarrow O_3 + M \qquad (2\text{-}11)$$

Net: $CO + 2\ O_2 \rightarrow O_3 + CO_2$ (2-12)

Column NO_2 has a long history of ground-based measurements. *Brewer et al.* [1973] published the first measurements. J. Noxon, in a series of papers in the late 1970's [*Noxon*, 1975; *Noxon et al.*, 1979; *Noxon*, 1980] established the basic latitudinal and seasonal behavior of column NO_2, including the famous Noxon's cliff, a large drop-off in winter high-latitude NO_2. S. Solomon used Noxon's measurements to understand the chemistry of N_2O_5 formation (Reaction 2.6) in the stratosphere [*Solomon and Garcia*, 1984]. Figure 2.1 shows five-year monthly mean total column NO_2 from the ESA GOME instrument. Noxon's cliff is dramatically illustrated in 2.1b and 2.1d for the Southern and Northern Hemisphere winters, respectively.

Tropospheric NO_2 can clearly be seen in Figure 2.1. Measured NO_2 values over the populated areas of the Eastern United States and Europe can be twice as high as values recorded

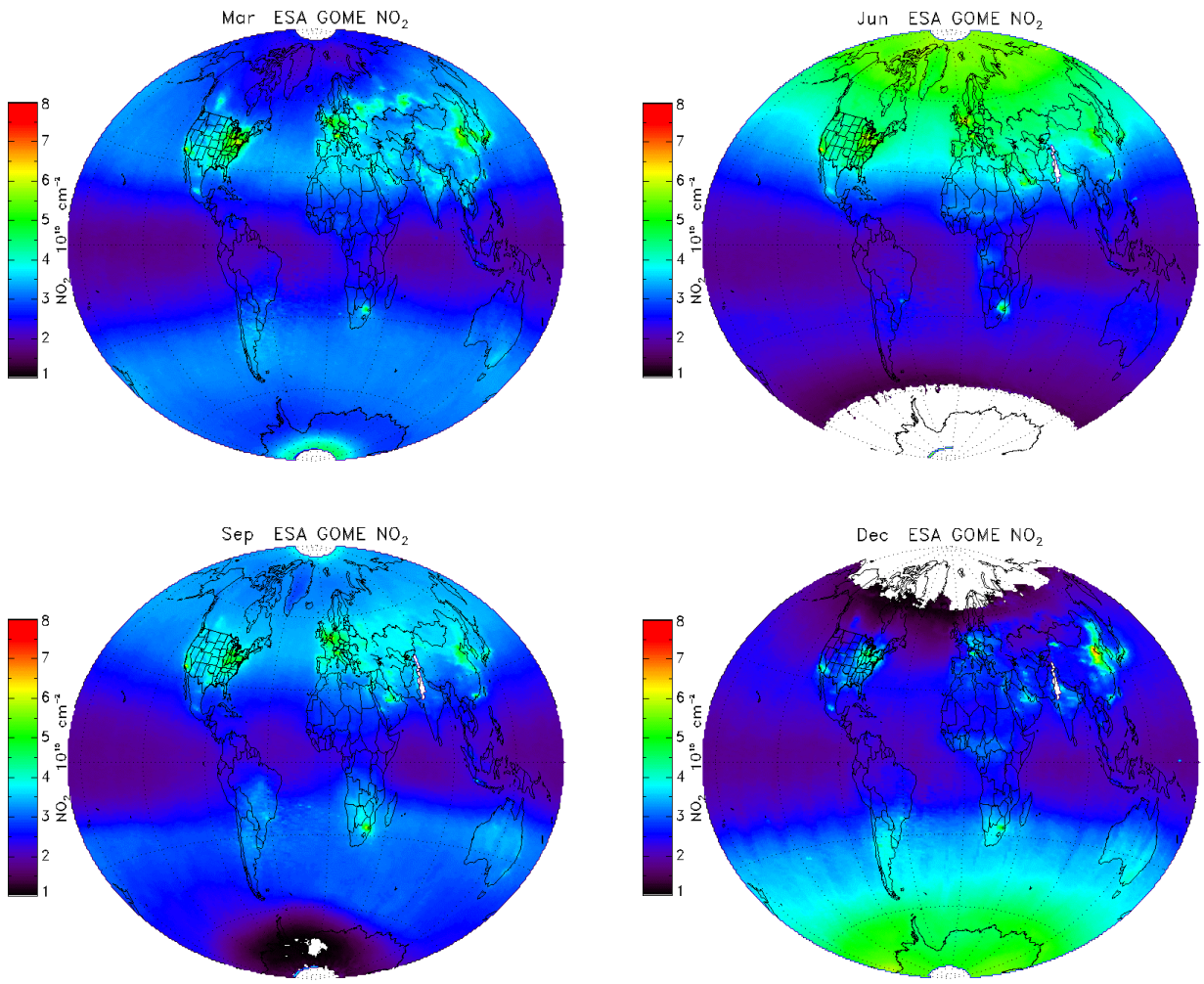

Figure 2.1 Seasonal Variation in Total Column NO_2 from 5 years of GOME

over adjacent less populated regions. Enhanced tropospheric NO_2 is also seen in Figure 2.2, which is a three-day composite of GOME NO_2 measurements for eastern North America. The tropospheric origin of the enhanced NO_2 is evident in the spatial correlation between the GOME measurements and the locations of NO_2 point sources, shown in Figure 2.3. Current retrieval algorithms, including the operational GOME NO_2 retrieval algorithm, are less sensitive to tropospheric NO_2 concentrations than to NO_2 in the stratosphere. Retrievals done over areas of enhanced tropospheric NO_2 result in total column values that are too low. The challenge for the OMI NO_2 algorithm will be to properly account for the amount of NO_2 in the troposphere, in order to report more accurate total column NO_2 measurements. A secondary product from the total column measurement will be a high-quality estimate of the tropospheric NO_2 column, an important scientific result.

2.2. Algorithm Description

The NO_2 algorithm will compute accurate vertical column densities from spectrally fitted NO_2 slant column densities. This will be accomplished by designating two components of the column density: an unpolluted component, which includes stratospheric and free tropospheric NO_2, and a polluted component, containing boundary layer NO_2. The two parts will be separated through spatial filtering of the geographic NO_2 field. Polluted NO_2 is assumed to show the greatest small-scale variation and will be isolated and corrected for air mass factor and

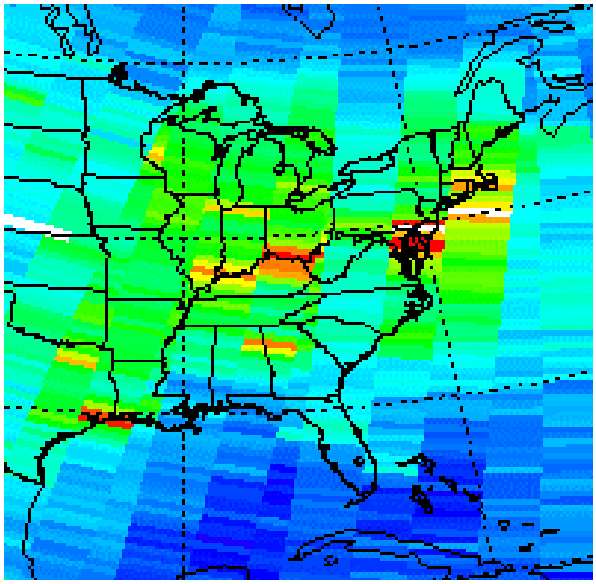

Figure 2.2 3-Day Composite of GOME NO_2 in April 1998. Scale asFigure 2.1.

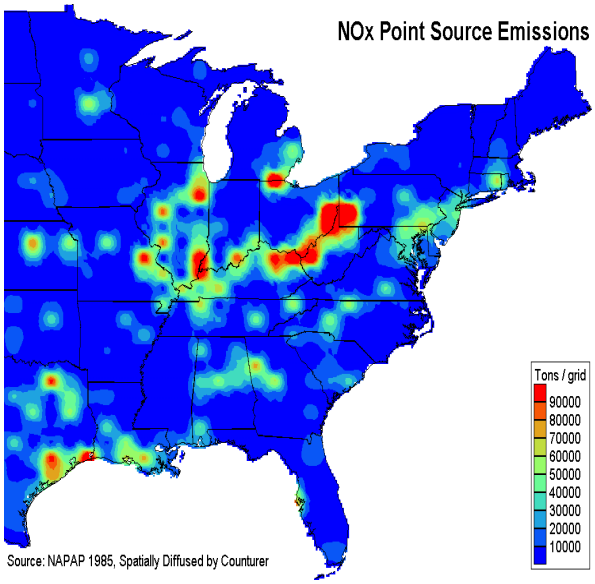

Figure 2.3 NOx Point Source Emission Map Source: OTAG Executive Summary.

temperature. The unpolluted and corrected polluted components will then be added to give the final vertical column density.

2.2.1. Slant column measurements

The baseline method to determine NO_2 slant column abundances is Differential Optical Absorption Spectroscopy (DOAS), which is a linear decomposition of earth radiance spectra. The 'BOAS' method of fitting a non-linear expression to the radiances is considered a non-baseline option for NO_2. Additional options will be part of the overall NO_2 fitting strategy, which will be fully tested during OMI commissioning, using synthetic spectra and data from GOME. The most successful methods will be used in the NO_2 slant column-density retrievals.

Radiance fitting by DOAS

The DOAS technique works well to determine column densities of trace gases from ground-based observations of direct light and has recently been applied successfully to the operational retrieval of NO_2 column densities from space-borne observations of scattered light [*Burrows et al.,* 1999]. In space-borne DOAS, the slant column density is interpreted as the column density along the average light path of photons that reach the detector.

A DOAS fit is a least squares fit of a modeled spectrum to the natural log of a measured reflectance spectrum. The reflectance spectrum, $R(\lambda)$, at wavelength λ is defined as π times the ratio of the radiance at the top of the atmosphere, $I(\lambda)$, divided by μ_0 times the extraterrestrial solar irradiance, $E(\lambda)$, where μ_0 is the magnitude of the cosine of the solar zenith angle. In general, both I and R are also functions of the observation zenith angle and the sun-satellite azimuth angle. The reflectance spectrum may be written:

$$R(\lambda) = \frac{\pi\, I(\lambda)}{\mu_0\; E(\lambda)}. \qquad [\,2\text{-}13\,]$$

The logarithm of the reflectance is assumed to be expressible as a linear sum, based on Lambert-Beer's law, which holds that

$$ln[R(\lambda)] = -\sum \sigma_i(\lambda) N_{s,i} - P_3(\lambda) \qquad [2\text{-}14]$$

where, for molecule i the slant column density is $N_{s,i}$ and the absorption cross section is $\sigma_i(\lambda)$. The Ring effect can be included in the summation in Equation [2-14], since the Ring spectrum, in this context, behaves as an effective absorption cross-section with an associated effective slant-column density. A third-order polynomial, $P_3(\lambda)$, is introduced to account for spectrally smooth extinction structures resulting from Rayleigh scattering, Mie (aerosol) scattering and absorption, surface albedo, and the slowly varying components of molecular absorption. Thus, only the highly structured *differential* (hence DOAS) trace gas structures contribute to the fit of the slant-column densities.

Slant column densities, $N_{s,i}$, and the polynomial coefficients are obtained through a least squares fitting that minimizes χ^2. The least squares fit is done in an unweighted fashion -i.e. all wavelengths in the spectrum are attributed the same weight (because measurement error per wavelength is assumed to be constant over the spectrum). Since $\ln[R(\lambda)]$ is linear in its fit parameters, χ^2 is minimized with a *linear* least squares method, based on the singular value decomposition (SVDFIT) from [*Press et al.*, 1986]. However, if certain reference spectra, $\sigma_i(\lambda)$, are not well wavelength calibrated, a *non-linear* fit can be used. By allowing reference spectra that suffer from calibration errors to be shifted and squeezed with respect to their wavelength grids (by adding a shift and squeeze as extra fit parameters), the fitting result can be improved. The modeled spectrum then depends on reference spectra that are adjustable in the fitting process, making the fit non-linear. For this method a routine (MRQMIN, the Levenberg-Marquardt Method) from *Press at al.* [1986] is used. The linear least squares method is the current fitting baseline.

Estimated fitting uncertainties are obtained from the covariance matrix of the standard errors. The effects of errors in the other spectral components on the NO_2 fit can be seen in the off-diagonal elements of the covariance matrix. However, these effects are expected to be small, due to the orthogonality of the basis functions (reference spectra) in the chosen NO_2 fitting window. Coefficients for all basis functions will also be given as diagnostic data.

Reference spectra

Reference spectra are degraded to the OMI resolution either in pre-tabulated form (baseline option) or using the parameterized slit function determined during the irradiance calibration (non-baseline option). They are then re-sampled to the radiance wavelength grid, using cubic spline interpolation [*Press et al.*, 1986]. Reference spectra for the NO_2 algorithm are shown in Figure 2.4. The current baseline choices are:

- NO_2 cross sections: *Vandaele et al.* [1998]. The NO_2 cross-section is temperature-dependent, with amplitudes of the differential absorption features increasing as temperature decreases. A difference of ~15% in amplitude exists between the warmest and coolest atmospheric NO_2. The current baseline is to fit spectra at a nominal stratospheric temperature of 220 K and then apply corrections for other temperatures.
- O_3 cross sections: *Burrows et al.* [1999];
- H_2O cross section: *Harder and Brault* [1997] (currently under review);
- O_2-O_2 cross section: *Newnham and Ballard* [1998] (currently under review);
- Ring-effect spectrum: *Chance and Spurr* [1997]. An additional Ring spectrum will be made available for OMI applications by J. Joiner [*private communication*];
- Under-sampling correction: Calculated dynamically, if required.

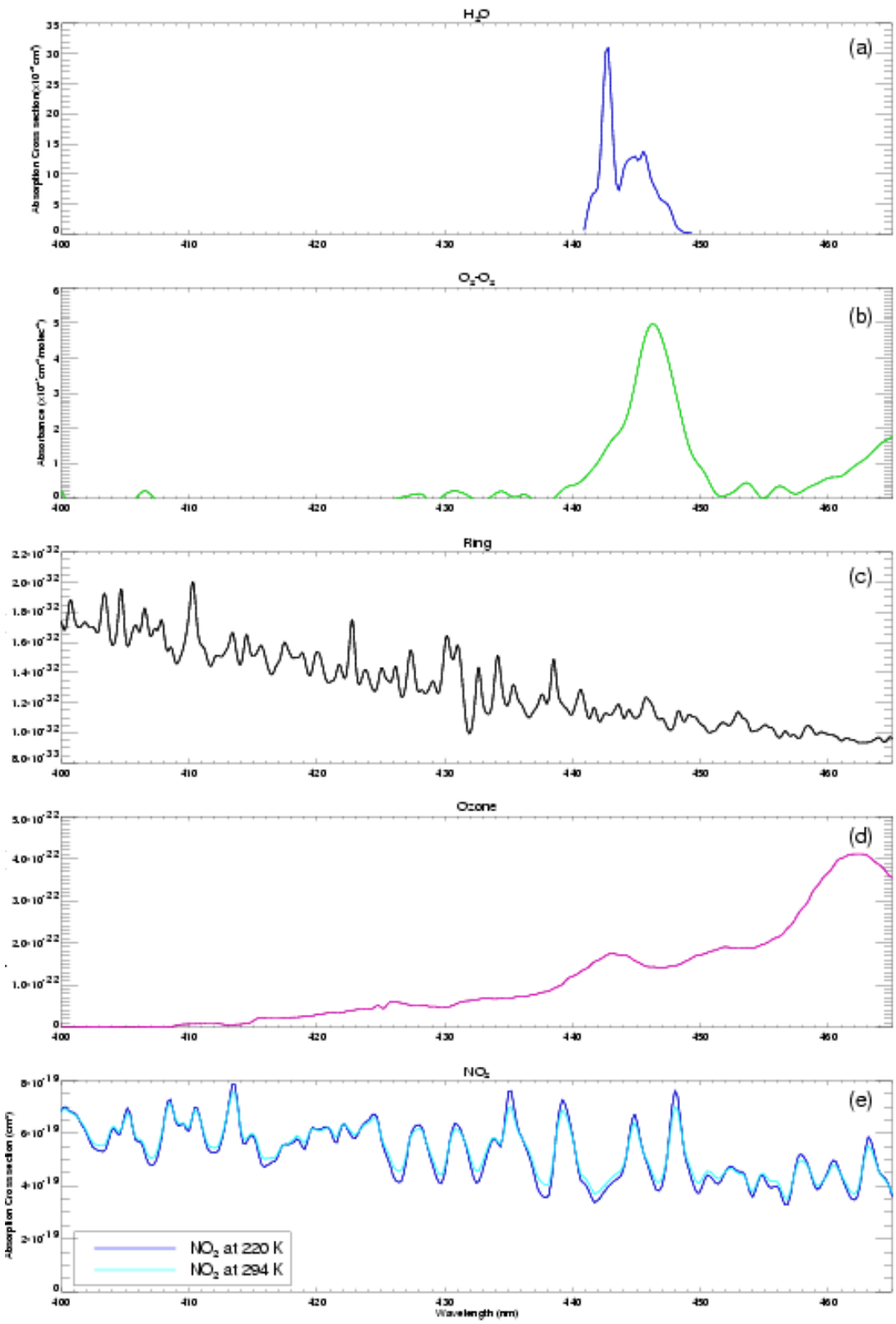

Figure 2.4 Reference spectra at OMI spectral resolution for water vapor (a), O_2-O_2 (b), Ring effect (c), ozone (d) and NO_2 (e).

Fitting window

The optimal wavelength window for the retrieval must have high sensitivity to the NO_2 absorption signature and minimal sensitivity to geophysical and instrument-related spectral features. Important considerations in selecting the wavelength range include

- Locating regions of maximum amplitude in the structures of the NO_2 cross section;
- Avoiding overlap with atmospheric spectral features, including those of other absorbers and parts of the Raman scattering (Ring) spectrum;
- Avoiding regions containing spectral structures of instrumental origin;
- Choosing as wide a window as possible to maximize the number of sampling points;
- Selecting a region of the NO_2 spectrum that minimizes temperature sensitivity.

A fitting window of 405-465 nm was selected for the baseline NO_2 retrieval. This choice includes the strongest NO_2 absorption features and avoids the Ring structures associated with the Ca II H and K lines at 397 and 393 nm and the band of the O_2-O_2 collision complex at 465-475 nm. Other window ranges were tested using simulated spectra from the DAK and TOMRAD radiative-transfer models. The tests indicate a broad minimum in NO_2 retrieval errors for windows centered between 430 nm and 450 nm, as shown in Figure 2.5. In this range, the errors decrease by about 15% when the width of the window is increased from 40 nm to 60 nm. A small reduction in temperature sensitivity can also be achieved by increasing the width of the fitting window.

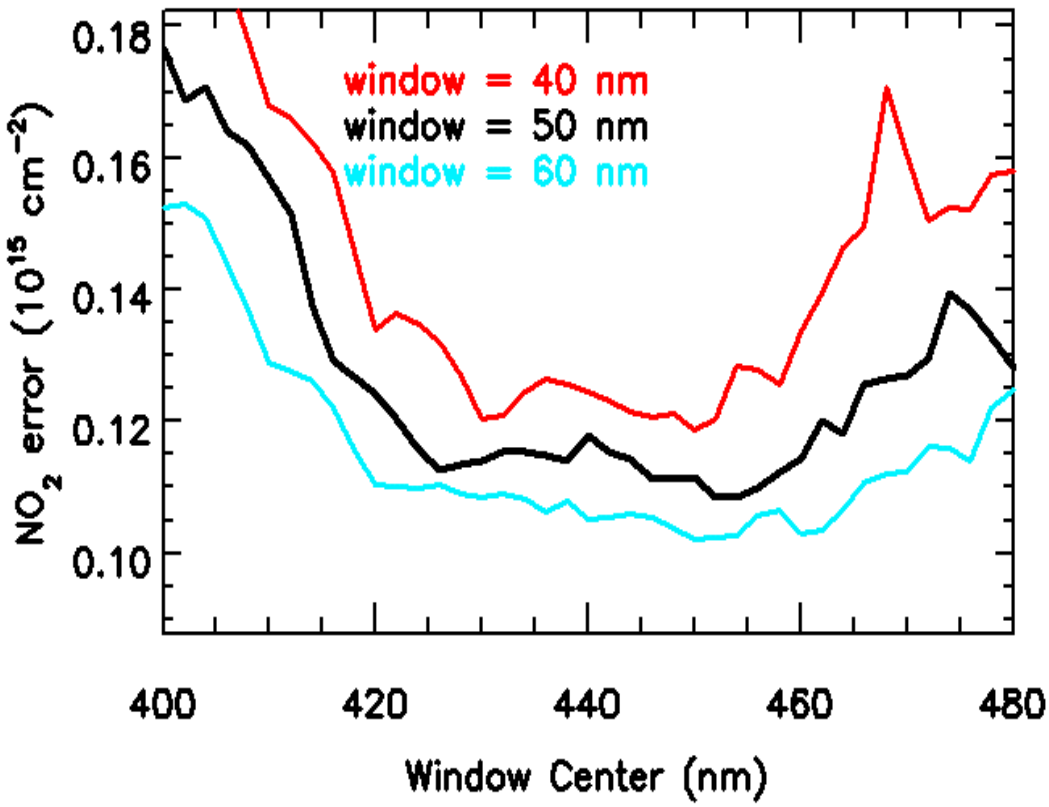

Figure 2.5 NO_2 fitting error dependence on fitting window (SNR=1000).

2.2.2. Air mass factors and vertical column abundances

Determination of NO_2 vertical column densities, N_v, from slant column densities, N_s, is accomplished in three steps:

(1) Calculate an air mass factor appropriate to unpolluted conditions and use this to get initial vertical column densities, $N_{v,\,init}$,

(2) Bin globally $N_{v,init}$ and apply spatial filtering to estimate the polluted and unpolluted components of the vertical column density,

(3) Correct $N_{v,init}$ for the polluted component, if significant. Otherwise, set $N_v = N_{v,init}$.

Air mass factor calculations

Air mass factors, $M = N_s / N_v$, are needed compute the NO_2 vertical column densities. We define M for spatially homogeneous scenes by the relation

$$M(z) = \frac{\int_z^\infty m(z')\, n(z')\, dz'}{\int_o^\infty n(z')\, dz'} \qquad [\,2\text{-}15\,]$$

where z is the altitude of the lower boundary of the visible part of the column, and $m = dN_s / dN_v$ is the altitude-resolved air mass factor. In general, $m(z')$ depends on altitude, viewing geometry and the albedo at altitude z. It is independent of the volume density profile, $n(z')$, which we may write as $n_p(z')$ for polluted cases and $n_u(z')$ for unpolluted cases. Note that the denominator in Equation [2-15] is always the total vertical column density above the ground (altitude $z = 0$).

The air mass factor, M', for a partly cloudy (i.e. spatially inhomogeneous) scene can be obtained under the *independent pixel assumption*, namely,

$$M' = w\, M(z_c) + (1 - w)\, M(0), \qquad [\,2\text{-}16\,]$$

where $M(z_c)$ is the air mass factor above cloud-top height, z_c, for a completely cloudy scene, and $M(0)$ is the air mass factor above the ground for a clear scene. A single cloud-top height is assumed within a given pixel. The radiance-weighted cloud fraction, w, is defined as

$$w = \frac{c\, I_{cloud}}{c\, I_{cloud} + (1-c)\, I_{clear}}, \qquad [\,2\text{-}17\,]$$

where c is the OMI *effective* cloud fraction, and I_{cloud} and I_{clear} are the radiances for cloudy and clear scenes, respectively. The effective cloud fraction equals the geometrical cloud fraction in the case of opaque clouds that behave as Lambertian surfaces. However, for optically thin or mixed clouds, the effective cloud fraction may be smaller than the geometrical cloud fraction.

Initial NO_2 vertical columns densities, $N_{v,init}$, will be found by dividing N_s by an air mass factor for partly cloudy, unpolluted conditions. Using Equation [2-16], we write this explicitly as

$$N_{v,\,init} = \frac{N_s}{w\, M_u(z_c) + (1-w)\, M_u(0)}, \qquad [\,2\text{-}18\,]$$

where the subscript u denotes air mass factors computed from the unpolluted profile, $n_u(z)$.

The OMI NO_2 algorithm will use *empirical* air mass factors, defined as the ratio of N_s to N_v. The slant column, N_s, is retrieved from model spectra using DOAS fitting identical to the

fitting applied to actual OMI spectra, and the vertical column, N_v, is known exactly from the input model atmosphere. The correspondence between atmospheric and model parameters determines the air mass factor accuracy, which dominates the OMI NO_2 vertical column accuracy. Two radiative transfer codes are used to model the spectra: TOMRAD [*Dave*, 1965] and the Doubling-Adding code KNMI (DAK, described by *Stammes* [2001]). At present the codes assume plane-parallel atmospheres, but a correction for atmospheric sphericity is included in TOMRAD.

A range of observing conditions will be considered. Air mass factors will be computed for a generic unpolluted NO_2 profile obtained from HALOE climatology and/or a chemical model. Calculations will also be done with various tropospheric profiles for polluted cases. Approximately four tropospheric profiles will be used, representing sources typical of industrial pollution and biomass burning, as well as locations downwind of pollution sources. Additional varied parameters will include the viewing geometry and the altitude and albedo at the lower bounding surface. The latter two can be chosen to represent a variety of ocean, land and cloud scenes, using albedos from MODIS or GOME data. We neglect the effects of aerosols, since their relative contribution to the total error budget is expected to be small in both polluted and unpolluted cases. Operationally, *M* will be obtained from a lookup table, as summarized below.

Table 2.1 Parameters used in the air mass factor lookup table.

Dimension name	Min. value	Max. value	# of entries
Solar zenith angle	0°	85°	TBD
Viewing zenith angle	0°	57°	TBD
Relative azimuth angle	TBD	TBD	TBD
Stratospheric NO_2 profile	N/A	N/A	1
Tropospheric NO_2 profile	N/A	N/A	< 4
Albedo	0	1	TBD
Terrain height	0 km	8 km	TBD
Cloud pressure	0 km	12 km	TBD
Latitude	-90°	+90°	TBD

Binning and smoothing

Information about the vertical distribution of the observed NO_2 column may be inferred from its geographic distribution. *Leue et al.*, [2001] distinguished boundary layer NO_2 from stratospheric NO_2 by spatial filtering of GOME NO_2 measurements over the Earth. Similarly, the procedure for analyzing the OMI data is based on the assumption that the spatial variability of polluted NO_2 occurs on smaller scales than that of unpolluted NO_2. To separate the two regimes, the $N_{v,init}$ are first binned on a uniform geographic grid. The data are then smoothed to produce a field, $N_{v,u}$, representative of the unpolluted NO_2 vertical column densities.

A complete global NO_2 map requires 24 hours of OMI data. The $N_{v,init}$ are binned once per orbit to produce maps containing data from the preceding and following 12- hours of orbits. The binning scheme uses grid cells that are 0.125 degrees in latitude by 0.250 degrees in longitude. Since the smallest dimensions of an OMI pixel are 13x24 km^2, cells near the equator have approximately the OMI spatial resolution.

Smoothing is accomplished by spatial filtering. The binned data are first masked to remove regions of known boundary-layer emissions. One-dimensional distributions comprising

360 degrees of longitude are then created by averaging the remaining $N_{v,init}$ field within latitude bands. The bands must be narrow enough (~5 degrees latitude) so that the natural latitudinal variation of stratospheric NO_2 is not smoothed out. Fourier analysis is applied to the distributions, and components with frequencies greater than wave-2 are removed. This wave frequency approximates the large-scale variations seen in HALOE measurements of stratospheric NO_2. Smoothing schemes that include other frequencies are currently being investigated.

Correction of the vertical column for polluted conditions

The total vertical column density is described accurately by Equation [2-18] when the NO_2 vertical profile is unpolluted. If a significant polluted component is present, then $N_{v,init}$ must be modified. This is readily done, since absorption is optically thin; the total slant column absorption is the sum of absorption by the polluted and unpolluted components of the profile. Two corrections are required. The first is an air-mass factor adjustment for the difference in optical path through the polluted part of the profile. Air mass factors for profiles that peak near the boundary layer (polluted) are generally smaller than high-altitude (unpolluted) air mass factors. The second correction accounts for the error introduced by spectrally fitting the polluted component of the NO_2 column with a cross section at the effective unpolluted temperature (220 K). In most situations, both corrections act to increase the total vertical column density. It can be shown [Appendix A: *Brinksma et al.*, 2001] that the polluted component of the vertical column density, $N_{v,p}$, and the corrected total vertical column, N_v, are given by

$$N_{v,p} = \frac{N_s - [w\,M_u(z_c) + (1-w)\,M_u(0)]\;N_{v,u}}{w\,M_p(z_c) + (1-w)\,M_p(0)} \times \alpha \qquad [2\text{-}19]$$

$$\textit{and} \qquad N_v = N_{v,u} + N_{v,p} \qquad [2\text{-}20]$$

where N_s is the slant column density from the initial spectral fit at the effective temperature of unpolluted NO_2, and $N_{v,u}$ is the unpolluted component of the vertical column density from the smoothing procedure. The homogeneous air mass factors are given by Equation [2-15]. $M_p(0)$ and $M_u(0)$ are, respectively, the polluted and unpolluted air mass factors over the surface for clear-sky conditions, and $M_p(z_c)$ and $M_u(z_c)$ are the corresponding air mass factors over clouds with tops at height z_c. Air mass factors are calculated from the polluted and unpolluted profile shapes, $n_p(z)$ and $n_u(z)$, which are known a priori and may overlap in altitude. The radiance weighting factor w is calculated from Equation [2-17], using a priori radiative transfer calculations and cloud fraction from the OMI cloud product. The factor α is the temperature correction, which is approximately the ratio of the amplitude of the NO_2 differential cross section at the effective unpolluted temperature to the amplitude at the effective polluted temperature. The estimated range is $1.1 < \alpha < 1.2$.

The decision to apply a pollution correction will be based on the value of the quantity $\Delta N_v = N_{v,init} - N_{v,u}$. If ΔN_v is positive and large, then the polluted vertical column density (Equation [2-19] will be reported, along with the corrected total vertical column density from Equation [2-20]. If ΔN_v is small or negative, no correction will be made – i.e., only $N_v = N_{v,init}$ will be reported as the total vertical column, using Equation [2-18]. For intermediate cases, an interpolated value of N_v will be reported. Note that the value of ΔN_v may be small for one or more of the following reasons: (1) pollution is negligible, (2) the true local value of the unpolluted column is much smaller than the smooth value, $N_{v,u}$, or (3) most of the polluted column is obscured by clouds or aerosols. The OMI NO_2 algorithm cannot distinguish among these possibilities. Instead, the criterion that ΔN_v exceeds the natural variability of unpolluted

NO_2 will be used to determine whether to apply a correction. The current baseline is to determine the natural variability from the 1-sigma variation of $N_{v,init}$ in pollution-free regions – e.g., over open ocean.

Figure 2.6 shows predicted slant column densities (assuming an isothermal atmosphere) as a function of effective cloud fraction. The unpolluted and polluted components of the NO_2 vertical column density profile are $4{\cdot}10^{15}$ and $6{\cdot}10^{15}$ mol/cm^2, respectively, with respective clear-sky air mass factors of 2.0 and 1.0. The solid black line and surrounding shaded region represent the slant column density of the unpolluted component and its natural range of variation. The curves represent observed total slant column densities under partly cloudy conditions for cloud-top heights ranging from 850 mb (red) to 200 mb (blue). When clouds are low, the enhancement in the slant column density due to the tropospheric component is significant for all cloud fractions. However, when high clouds are present, they hide much of the tropospheric component, making it impossible to distinguish pollution from natural variation for cloud fractions above 0.3.

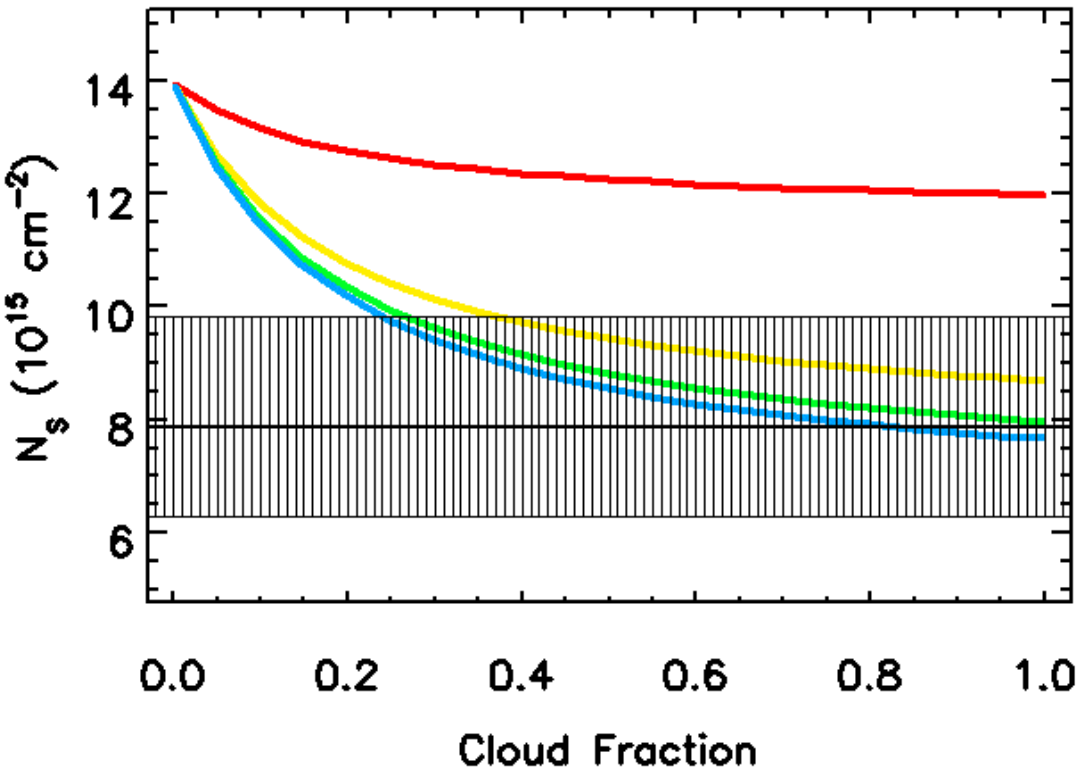

Figure 2.6 Theoretical slant column densities, N_s, vs. cloud fraction for unpolluted NO_2 and its natural variation (shaded region), and for a mixed polluted and unpolluted profile with cloud tops at 850 mb (red), 700 mb (yellow), 500 mb (green), and 200 mb (blue) . The calculations assumed cloud and surface albedos of 0.80 and 0.05, respectively.

2.2.3. Outputs

Standard outputs include:

- Slant column abundance and 1-sigma fitting uncertainties for NO_2 and the other species varied in the fitting window;
- Correlation of other fitted species to NO_2 (from off-diagonal elements of the covariance matrix of the standard errors);

- Fitting *rms*;
- Geolocation information;
- Version numbers of algorithm and parameter input file;
- Vertical column abundances and 1-sigma uncertainties;
- Tropospheric vertical column abundances and 1-sigma uncertainties.

2.2.4. Validation

Synthetic and observational data will be used for testing the OMI NO_2 algorithm. Because the OMI instrument properties are not well characterized at present, synthetic spectra will be the primary means of verifying the accuracy of the DOAS technique, but GOME data have also been used as input to the OMI NO_2 algorithm, with good results.

For validation purposes after launch, OMI vertical column densities may be compared with GOME level-1 and -2 data. However, such comparisons are valid only in unpolluted regions, as the current GOME algorithm makes no adjustments for tropospheric NO_2. Estimates of the tropospheric column are available in discrete locations from ground-based measurements. We refer to the AURA validation plan for further details.

2.3. Error Analysis

The OMI DOAS NO_2 algorithm generates two level-2 products, namely, total vertical column densities for all pixels and tropospheric column densities for pixels with significant NO_2 pollution. Since retrieval assumptions differ considerably between unpolluted and polluted cases, the error budget for each case will be treated separately.

The accuracy in the vertical column density is defined as the root-mean-square of all errors, including forward model, inverse model and instrument errors. To investigate the sensitivity of the OMI DOAS NO_2 algorithm to random errors and retrieval assumptions, a number of sensitivity studies were performed. Studies involved both unpolluted and polluted situations. In the analysis, reference cases were perturbed to quantify the effect of errors on the retrieval. Case studies assumed a surface albedo of 0.05, and a mid-latitude standard atmospheric profile containing approximately $5 \cdot 10^{15}$ mol/cm^2 of NO_2. Situations with enhanced NO_2 levels were modeled by adding $8 \cdot 10^{15}$ mol/cm^2 of NO_2 to the lower troposphere, using a globally (13:30 local time) averaged tropospheric NO_2 profile from the TM3 chemical transport model [*Houweling et al.*, 1993] for 20 known industrial areas. The results of sensitivity studies on error sources are described in terms of percentage of their value (slant column density and air mass factor) and summarized in Table 2.2. The values are considered to be root-mean-square errors, i.e., they represent all atmospheric conditions and all possible viewing geometries. Errors that vary from day-to-day are considered random errors. Slant column density retrieval suffers from random errors related to atmospheric temperature and instrument noise. Air mass factor error arises from incorrect day-to-day assumptions regarding the NO_2 profile, cloud fraction and aerosol effects.

The cumulative effects of all error sources considered in the sensitivity studies are summarized in Table 2.3. The magnitude of the error in vertical column density is much greater under polluted conditions, due mainly to air-mass-factor uncertainty. This is especially apparent in cloudy cases. Under clear, unpolluted conditions the total column error is ~ 7%, but can be as large as 20 – 50 % in the presence of pollution and clouds. Errors in the tropospheric column density estimate are larger than the total column errors.

Table 2.2 Results Sensitivity Analysis of the OMI DOAS NO_2 algorithm.

Slant column errors	**Unpolluted case error (%)**	**Polluted case error (%)**
NO_2 cross section	2	2
Temperature	4	6
Instrument noise	4	2
Spectral calibration	0.5	0.3
Air mass factor errors		
NO_2 profile shape	1	20
Surface albedo	0.5	20
Cloud albedo	0.5	4
Cloud fraction	0.3	8
Cloud pressure	0.5	50
Aerosol assumption	1	15
Error in $N_{v,u}$		
Estimation of $N_{v,u}$	N/A	5

Table 2.3 Estimated accuracy of the OMI DOAS NO_2 algorithm.

Vertical column errors	**Unpolluted case Total column error**	**Polluted case Total column error**	**Polluted case Tropospheric column error**
Clear	7 %	20 %	30 %
Partly Cloudy	7 %	50 %	60 %

2.4. Acknowledgments

We are grateful to Johan de Haan for useful suggestions and careful reading of several stages of this ATBD.

Various radiative transfer simulations were carried out using the Doubling-Adding Code KNMI (DAK) [*Stammes*, 2000; *De Haan et al.*, 1987; *Stammes et al.*, 1989]. We are grateful to Piet Stammes for making this code available.

2.5. References

Brewer, A. W., C. T. McElroy, and J. B. Kerr, Nitrogen dioxide concentrations in the atmosphere, Nature, 246, 129, 1973.

Brinksma, E., J.F. de Haan, E. Bucsela, F. Boersma, and J. Gleason, Air mass factors over clouded scenes, Appendix to OMI ATBD, 2001.

Burrows, J.P., A. Richter, A. Dehn, B. Deters, S. Himmelmann, S. Voigt, and J. Orphal, Atmospheric remote sensing reference data from GOME - 2. Temperature-dependent absorption cross-sections of O_3 in the 231-794 nm range, J. Quant. Spectrosc. Radiat. Transfer 61, 509-517, 1999.

Burrows, J.P., M.Weber, M. Buchwitz, V.V.Rosanov, A. Ladstatter, A. Weissenmayer, A.Richter, R.DeBeek, R.Hoogen,K. Bramstedt, and K.U. Eichmann, The Global Ozone Monitoring Experiment (GOME): Mission concept and first scientific results, *J. Atmos. Sci.,* 56, 151-175, 1999.

Chance, K., and R.J.D. Spurr, Ring Effect Studies: Rayleigh Scattering, Including Molecular Parameters for Rotational Raman Scattering, and the Fraunhofer Spectrum, Appl. Opt. 36, 5224-5230, 1997.

Dave, J.V. Multiple scattering in a non-homogeneous, Rayleigh atmosphere, J. Atmos. Sci. 22, 273-279, 1965.

De Haan, J.F., P.B. Bosma, and J.W. Hovenier, The adding method for multiple scattering calculations of polarized light, Astron. Astrophys. 183, 371-391, 1987.

De Vries, J., S/N status prediction, SE-OMIE-0437-FS/00, 2000.

Greenblatt, G.D., J.J. Orlando, J.B. Burkholder, and A.R. Ravishankara, Absorption measurements of oxygen between 330 and 1140 nm, J. Geophys. Res. 95, 18,577-18,582, 1990.

Harder, J.W. and J.W. Brault, Atmospheric measurements of water vapor in the 442-nm region, J. Geophys. Res. 102, 6245 – 6252, 1997.

Houweling, S., F.J. Dentener and J. Lelieveld, The impact of non-methane hydrocarbon compounds on tropospheric photochemistry, J. Geophys. Res,. 103, 10,673-10,696, 1998.

Koelemeijer, R.B.A., Stammes, P., Hovenier, J.W. and De Haan, J.F., A fast method for retrieval of cloud parameters using oxygen A band measurements from the Global Ozone Monitoring Experiment, *J. Geophys. Res., 106,* 3475-3490, 2001.

Leue, C., M. Wenig, T. Wagner, O. Klimm, U. Platt, and B. Jaehne, Quantitative analysis of NO_X emissions from Global Ozone Monitoring Experiment satellite image suences, J. Geophys. Res. 106, 5493-5505, 2001.

Levelt, P.F. and co-authors, Science Requirements Document for OMI-EOS, RS-OMIE-KNMI-001, Version 2, ISBN 90-369-2187-2, 2000.

Newnham D.A. and J.Ballard, Visible absorption cross sections and integrated absorption intensities of molecular oxygen O_2 and O_4, *J. Geophys. Res.,* 103, 28801-28816, 1998.

Noxon, J. F., Nitrogen dioxide in the stratosphere and troposphere measured by ground-based absorption spectroscopy, *Science*, *189*, 547, 1975.

Noxon, J. F., E. C. Whipple, Jr., and R. S. Hyde, Stratospheric NO_2, 1. Observational method and behavior at mid-latitude, *J. Geophys. Res*., *84*, 5047, 1979.

Noxon, J.F. Stratospheric NO_2, 2. Global behavior, *J. Geophys. Res., 84*, 5067, 1997. Correction *J. Geophys. Res. 85*, 4560, 1980.

Press, W.H., B.P. Flannery, S.A. Teukolsky, and W.T. Vetterling, *Numerical Recipes*, ISBN 0-521-30811-9, Cambridge University Press, 1986.

Solomon, S. and R. R. Garcia, On the distribution of long-lived tracers and chlorine species in the middle atmosphere, J. Geophys. Res., 89, 11633-11644, 1984.

Stammes, P., J.F. de Haan, and J.W. Hovenier, The polarized internal radiation field of a planetary atmosphere, Astron. Astrophys. 225, 239-259, 1989.

Stammes, P., Spectral radiance modelling in the UV-Visible Range, to appear in *IRS 2000: Current problems in Atmospheric Radiation*, Eds. W.L. Smith and Y.M. Timofeyev, A. Deepak Publ., Hampton (VA), 2001.

Vandaele A.C., C. Hermans, P.C. Simon, M. Carleer, R. Colin, S. Fally, M.F. Mérienne, A. Jenouvrier, and B. Coquart, Measurements of the NO_2 absorption cross-section from 42000 cm^{-1} to 10000 cm^{-1} (238-1000 nm) at 220 K and 294 K, J. Quant. Spectrosc. Radiat. Transfer 59, 171-184, 1998.

2.A. Appendix A: Air mass factors over clouded scenes

Authors: Ellen Brinksma, Johan de Haan, Folkert Boersma, KNMI
Eric Bucsela, James F. Gleason, NASA-GSFC

In the NO_2 ATBD, an expression for the polluted (≈ tropospheric) vertical column density was presented. In this appendix, we derive this expression, along with expressions for the air mass factors over clouded scenes.

2.A.1. Effects of clouds and aerosols

Clouds have varying effects on air mass factors. Firstly, clouds obscure gas located below the cloud, and thus decrease measurement sensitivity. Secondly, clouds generally increase the sensitivity to gas above clouds, due to the relatively high cloud albedo. Under background (unpolluted) conditions, aerosol concentrations are expected to be small, and we assume that the influence of aerosols can be neglected. Where tropospheric gas concentrations are enhanced (polluted conditions), aerosol concentrations are often enhanced as well, and the aerosol's effect on the air mass factor may be significant. However, high aerosol concentrations are typically associated with other, larger error sources. Therefore, our preliminary approach will be to neglect the influence of aerosols in the air mass factor calculations.

2.A.2. Definitions

To convert slant column densities (N_s), retrieved by performing DOAS fits to OMI spectra, into vertical column densities (N_v), an airmass factor (M) is used. This is a number which, for specific atmospheric conditions, viewing geometry, NO_2 altitude distribution, etc., is defined as

$$M = \frac{N_s}{N_v} \tag{1}$$

Simulations using a radiative transfer model and an OMI-simulator are used to derive numerical values of M for various atmospheric input conditions (including NO_2 profile shape). This is done independently for completely clouded and completely clear scenes, and for various profile shapes. To these simulated spectra, a DOAS fit is applied to derive N_s. Since for the model atmosphere the vertical column density is known, M can be determined.

Let $m(z)$ be the altitude resolved air mass factor. It can be calculated using a radiative transfer code, as above, by inserting NO_2 at one altitude z, and calculating the airmass factor – which will be interpreted as the altitude resolved airmass factor at altitude (z). This calculation should be repeated for all altitudes. The (total) airmass factor is related to the altitude resolved airmass factor by

$$M = \frac{\int_0^\infty m(z)n(z)dz}{\int_0^\infty n(z)dz} \tag{2}$$

where $n(z)$ is the NO_2 number density at altitude z. Note that $m(z)$ does not depend on the NO_2 profile shape, while M does.

In addition, the normalized profile $n_n(z)$ is defined as follows:

$$n(z) = N_v n_n(z) \tag{3}$$

where N_v is the vertical column density. Consequently, the normalized profile obeys the condition

$$\int_0^\infty n_n^{unp}(z)\, dz = \int_0^\infty n_n^p(z)\, dz = 1 \tag{4}$$

2.A.3. Unpolluted and polluted profiles.

Two NO_2 number density profiles are defined: an unpolluted profile, $n^{unp}(z)$, which consists mainly of stratospheric NO_2, and a polluted profile $n^p(z)$, which peaks in the lower troposphere.

The (total) profile is given by

$$n(z) = N_v^{unp} n_n^{unp}(z) + N_v^p n_n^p(z) \tag{5}$$

2.A.4. Application

In order to separate the measured unpolluted and polluted NO_2 fields, a smoothed field is introduced that represents the mean unpolluted column density (smoothed) for a pixel. This value follows from a fitting procedure as described in Chapter 6, and will be denoted by $<N_v>$. We will substitute $<N_v>$ for N_v^{unp} .

2.A.5. Cloudless case

The airmass factor for a cloudless scene can be expressed as:

$$M \equiv \frac{N_s}{N_v} = \frac{N_s^{unp} + N_s^p}{<N_v> + N_v^p} = \frac{<N_v> M^{unp} + N_v^p M^p}{<N_v> + N_v^p}, \tag{6}$$

where M^{unp} and M^p are the airmass factors for the unpolluted and polluted profiles, respectively.

With Eq. (6), the total VCD for a clear scene is given by:

$$N_v = \langle N_v \rangle + N_v^p = \frac{N_s^{meas}}{M} = N_s^{meas} \frac{\langle N_v \rangle + N_v^p}{\langle N_v \rangle M^{unp} + N_v^p M^p}, \tag{7}$$

where N_s^{meas} is the slant column density derived from a DOAS fit applied to the OMI spectra, assuming an effective temperature typical for the smooth (~ stratospheric) profile.

If Eq. (7) is solved for the polluted column density N_v^p, and the right-hand-side is multiplied by a correction factor to incorporate the appropriate effective temperature, Eq. (8) emerges;

$$N_v^p = \frac{N_s^{meas} - \langle N_v \rangle M^{unp}}{M^p} \frac{\sigma_{NO2}(T_{unp})}{\sigma_{NO2}(T_p)} \qquad \textit{[unclouded pixel]} \tag{8}$$

where T_p and T_{unp} are the effective temperatures for the polluted and unpolluted atmospheres, and σ_{NO2} is the absorption cross-section of NO_2. Effective temperatures are defined as temperatures weighted with NO_2 number density and air mass factor, for example

$$T_p = \frac{\int_0^\infty T(z)\, m(z)\, n_n^p(z)\, dz}{\int_0^\infty m(z)\, n_n^p(z)\, dz} = \frac{\int_0^\infty T(z)\, m(z)\, n_n^p(z)\, dz}{M^p} \tag{9}$$

and analogously for T_{unp}. Once N_v^p is known, the total vertical column can be calculated from $N = < N_v > + N_v^p$.

2.A.6. Clouds

We now turn to a partly cloudy pixel. Let z_{cloud} be the altitude of the Lambertian cloud. A fraction k^p of the polluted profile will be situated above the clouds, i.e.

$$k^p = \int_{zcloud}^{\infty} n_n^p(z) dz \tag{10}$$

And, defined analogously, a fraction k^{unp} of the unpolluted profile will be located above the cloud. Suppose a particular pixel is not polluted. Then we have

$$N^{meas} = wX^{unp}(z_{cloud})k^{unp}N_v^{unp} + (1-w)M^{unp}N_v^{unp} \tag{11}$$

where w is the reflectance-weighted cloud fraction (see Chapter 5 for definition), $X^{unp}(z_{cloud})$ is an airmass factor for the cloudy pixel, defined as

$$X^{unp}(z_{cloud}) = \frac{\int_{zcloud}^{\infty} m^{cloud}(z) n_n^{unp}(z) dz}{k^{unp}} \quad , \tag{12}$$

where we added the superscript cloud to m to indicate that it depends (slightly) on the surface albedo of the Lambertian cloud. $X^{unp}(z_{cloud})$ can be interpreted as the slant column density observed over a completely clouded pixel, divided by the normalized vertical column density *located above the cloud*. However, to simplify the equation, we will define the airmass factor differently, namely as:

$$M^{unp}(z_{cloud}) = k^{unp}X^{unp}(z_{cloud}) = \int_{zcloud}^{\infty} m^{cloud}(z) n_n^{unp}(z) dz \tag{13}$$

which can be interpreted as the measured slant column density divided by the total vertical column density. Equation (13) will be substituted into Eq. (11)

From Eq. (11) it follows that the vertical column can be calculated using

$$N_v^{unp} = \frac{N_s^{meas}}{wM^{unp}(z_{cloud}) + (1-w)M^{unp}} \tag{14}$$

If we deal with a polluted pixel, we have to extend Eq. (11) to the following:

$$N_s^{meas} = w(M^{unp}(z_{cloud})N_v^{unp} + M^p(z_{cloud})N_v^p) + (1-w)(M^{unp}N_v^{unp} + M^pN_v^p) \tag{15}$$

If we substitute N_v^{unp} by $<N_v>$, and solve for N_v^p, this yields:

$$N_v^p = \frac{N_s^{meas} - (wM^{unp}(z_L) + (1-w)M^{unp}) < N_v >}{wM^p(z_L) + (1-w)M^p}, \tag{16}$$

The polluted column is given by Eq. (16). The total column follows from $N_v = \langle N_v \rangle + N_v^p$, and the column located under the clouds (which was NOT explicitely assumed) is $N_v^{ghost} = (1-k^p)N_v^p + (1-k^{unp})\langle N_v \rangle$

2.A.7. Temperature correction

The measured slant column density was retrieved by applying a DOAS fit for a temperature appropriate for the unpolluted profile. Airmass factor calculations are also performed for this same temperature. However, since the pollution is located in the troposphere, a temperature correction must be applied to both of the airmass factors in the denominator.

For a completely clouded scene, the airmass factor is defined as:

$$T_p = \frac{\int_{zcloud}^{\infty} T(z)m(z)n_n^p(z)dz}{\int_{zcloud}^{\infty} m(z)n_n^p(z)dz} = \frac{\int_{zcloud}^{\infty} T(z)m(z)n_n^p(z)dz}{M^p(z_{cloud})} \tag{17}$$

for the polluted part of the profile. Similar definitions to Eqs. (9) and (17) apply to the unpolluted part of the profile (air mass factors in the numerator), but we will assume that the temperature used in the DOAS fit is does not differ much from the unpolluted profile effective temperature, and thus that a temperature correction for the unpolluted profile is not necessary.

2.B. Appendix B: Error analysis details

Authors: Folkert Boersma, Ellen Brinksma, KNMI
Eric Bucsela, James F. Gleason, NASA-GSFC

2.B.1. Slant column density

Errors in the inverse model come from a priori errors and instrument errors. The accuracy of the NO_2 absorption cross-section spectrum and the assumptions on the temperature of the NO_2 in the atmosphere are typical a priori errors. Measurement noise and spectral calibration are instrument errors.

(1) NO_2 cross section spectrum

The accuracy of the NO_2 cross section is estimated to be 2% [*Vandaele et al.*, 1998]. Since this 2% is mostly due to offset errors, the error in the NO_2 slant column density is estimated to be less than 2%.

(2) Temperature dependence

In fitting NO_2 to a reflectivity spectrum, a 220 K effective temperature is assumed for NO_2. The fit window is optimized such that the temperature dependence is minimal. For unpolluted conditions, a 10 K perturbation of the effective temperature results in a 3.7 % fit error (as can be seen from Figure 4). In polluted situations, the temperature correction as described in Chapter 5 will reduce the error due to assuming an effective temperature to approximately 6% in the NO_2 slant column density.

(3) Measurement noise

The radiometric signal-to-noise ratio of OMI in the 400 – 480 nm range is estimated to be of the order 2800 for four co-added pixels [*De Vries et al.*, 2000]. Tests with the proposed 405 – 465 nm fit window showed that the error in the slant column density due to noise is less than 4% for nominal conditions and less than 2% for situations with enhanced NO_2 levels.

(4) Spectral calibration and stability

DOAS is sensitive to wavelength calibration errors. OMI reflectivity spectra will be calibrated from cross-correlating the Fraunhofer lines in the solar irradiance with the Earth radiance spectra. The spectral calibration is estimated to be better than 0.0021 nm [*Levelt et al.*, 2000]. The error in the NO2 slant column density due to a spectral calibration error of 0.0021 nm is 0.5% for nominal conditions and 0.3% for enhanced NO_2 conditions.

Because of instrument temperature differences over an OMI orbit, the wavelength grid of the Earth's radiance spectra will shift with respect to the irradiance spectra. To account for this effect, irradiance spectra will be spline interpolated to the radiance wavelength grid. The spectral stability over an orbit is estimated to be better than 0.011 nm [*Levelt et al.*, 2000]. Interpolating the solar irradiance spectrum to a 0.011 nm ($1/20^{th}$ of a spectral pixel) shifted wavelength grid causes irradiance levels to change by less than $2 \cdot 10^{-5}$. This error has a negligible effect on slant column density retrieval.

2.B.2. Air Mass Factor

The most important errors in the air mass factor come from a priori assumptions regarding the state of the atmosphere. The air mass factor is especially sensitive to the shape of the NO_2 profile and the value of the surface albedo in situations with enhanced NO_2 levels. Other errors are due to assuming that clouds can be represented as Lambert surfaces with an albedo of 0.8 and assumptions regarding the aerosol model that is used for situations with enhanced NO_2 levels.

(1) NO_2 profile shape

The sensitivity of the air mass factor on the NO_2 profile shape is particularly important in the case of enhanced NO_2 levels, when surface emissions can give rise large variability in the tropospheric NO_2 burden [*Houweling et al.*, 1998]. The NO_2 profile is much better known for unpolluted situations, when seasonal variations dominate the stratospheric NO_2 column and the uncertainty in the unpolluted air mass factor due to assuming an approximately geometrical air mass factor is estimated to be 1%. The large uncertainty in the tropospheric NO_2 profile shape has been investigated by analyzing a yearly average tropospheric NO_2 profile that was generated from 12 monthly profiles (1997) from 20 regions with emissions from industrial sources. The large variability in boundary layer NO_2 concentrations as well as the uncertainty whether TM3 is representing the boundary layer in a proper way is resulting in an estimate of the uncertainty in the tropospheric air mass factor of approximately 20% for situations with enhanced NO_2 levels.

(2) Surface albedo

The air mass factor is sensitive to the assumed value of the surface albedo. Using DAK simulations, this sensitivity was assessed. In both nominal and enhanced NO_2 cases, the sensitivity is larger for dark surfaces than for bright surfaces, although for the nominal case, this difference is small. We assume that the variability within a grid box of the surface albedo database is ±0.03 [*Koelemeijer et al.*, 2001]. For nominal cases, a surface albedo change of ±0.03 to a realistic continental surface albedo of 0.05 yields an airmass factor change of ±0.5 %. For situations with enhanced NO_2 levels, the sensitivity to the surface albedo is much larger and much more dependent on the surface albedo. In this case, an albedo change of ±0.03 to a typical surface albedo of 0.05 yields an airmass factor change of 22 %, for a bright surface (albedo 0.2) this change is 6 %. Since enhanced NO_2 concentrations are often observed over land, the accuracy due to surface albedo uncertainties is estimated to be 20 %.

(3) Cloud albedo

Assuming that clouds can be represented as Lambertian surfaces, the sensitivity to changes in cloud albedo was tested by using the same simulation procedure as described above. For nominal conditions, the typical uncertainty of the airmass factor induced by an albedo change of ±0.1, is 1.5 %. For situations with enhanced NO_2 levels and typical cloud albedoes (0.6 to 0.8) this is 4%.

(4) Cloud fraction

Errors in the cloud fraction induce an inaccuracy in the air mass factor via the weighting factor described in equations (8) and (9). The accuracy of the cloud fraction is expected to be 0.1 [*Levelt et al.*, 2000]. For nominal situations, an error in the cloud fraction of 0.1 results in an error in the air mass factor of 0.3 %. For situations with enhanced NO_2 levels, the error depends very much on the cloud fraction itself. For cloud fractions below about 0.3, when it is still possible to detect $N_{v,p}$, errors in the cloud fraction of 0.1 result in errors in the air mass factor < 8%.

(5) Cloud pressure

The required accuracy of the cloud pressure is 100 hPa [*Levelt et al*., 2000]. For nominal cases, this induces an inaccuracy on the airmass factor of 0.3 % at the ground, through 1 % at 200 hPa. For enhanced NO_2 levels, the largest sensitivity is found when the cloud is located within the region of high NO_2 concentrations. A 100 hPa inaccuracy on the cloud pressure induces a 50 % error on the air mass factor for clouds at 900 hPa, a 0.6 % error at 500 hPa, and a 1.2 % error at 200 hPa.

(6) Aerosol effect

Radiative transfer calculations to construct air mass factor look-up tables make an assumption about scattering and absorption by aerosol particles. For background situations, when most of the NO_2 is above tropospheric aerosol layers, air mass factors are estimated to be accurate to 0.5%. In situations of enhanced NO_2 levels, aerosol concentrations are usually also enhanced (smog, biomass burning) and assumptions on an aerosol model can give rise to errors in the air mass factor of about 15%.

(7) Estimate of the unpolluted column

The uncertainty in determining $N_{v,unp}$ from the smoothing and gridding procedure is estimated to be 5%.

2.C Appendix C: Data Products Table and Data Product Dependencies

Authors: Eric Bucsela, James F. Gleason, NASA-GSFC
Folkert Boersma, Ellen Brinksma, KNMI

Primary Product: Total NO_2 vertical column density + error
Secondary Product: Tropospheric NO_2 vertical column density + error

Diagnostic Data
Slant Column NO_2 + error
Tropospheric Slant Column NO_2 + error
Cloud fraction & Cloud height
Clear AMF & Cloudy AMF
Aerosol Correction
Coefficients for all basis functions
Geo-location Information
Solar and Viewing Geometry

Data Dependencies	Data Source	Required
Cloud fraction & Cloud height	OMI Cloud Group	Yes
Solar and Viewing Geometry	OMI Instrument Team	Yes
Surface Albedo	Koelemeijer database	Yes
Aerosol Data	OMI Aerosol Group	No
Temperature Profile	NCEP	No
HIRDLS NO_2 Profiles	Aura HIRDLS Group/DAAC	No

3. HCHO

K. Chance, T.P. Kurosu, and L.S. Rothman
Smithsonian Astrophysical Observatory
Cambridge, MA, USA

HCHO is a principal intermediate in the oxidation of hydrocarbons in the troposphere, providing an important indicator of biogenic activity. In the remote marine troposphere it may serve as a useful proxy for tropospheric OH. HCHO was proposed for measurement from space by the GOME instrument [*Chance et al.,* 1991] and was first measured from space by GOME, in the 337-359 nm range [*Thomas et al.*, 1998]. HCHO is prominent in the Southeastern U.S. in summertime (from isoprene oxidation) [*Chance et al.*, 2000] and is also a prominent product of biomass burning [*Thomas et al.*, 1998]. Figure 3.1a shows vertical column abundances of HCHO derived from GOME measurements over North America for July 1996; Figure 3.1b shows the modeled result from the GEOS-CHEM 3-dimensional tropospheric chemistry and transport model. The HCHO in this case is primarily due to isoprene oxidation. Figure 3.2 shows in more detail the results from a single GOME orbit exhibiting high isoprene production over the southeastern U.S. Figures 3.3a and 3.3b show enhanced HCHO as measured by GOME from biomass burning episodes over the northern Amazon basin, and over Indonesia during the intense fires of 1997, respectively. OMI will measure HCHO at higher spatial resolution than GOME and with better temporal coverage, allowing for improved characterization of sources and transport. GOME has difficulty in measuring HCHO at concentrations typical of the remote marine free troposphere due to systematic effects, which may be associated with the instrument. OMI may overcome these and thus supply better determination of the global climatology of free tropospheric HCHO.

Absorptions for HCHO are quite small (substantially less than 1% in most cases), so that they are optically thin to a high degree of accuracy and so that interferences from other causes (e.g., O_3 absorption and the Ring effect) must be accounted for very precisely. The fitting for HCHO includes two major steps: (1) the fitting of a selected wavelength window of spectrum to determine the slant column density, N_{si}, for a particular species i, and (2) the determination of an appropriate air mass factor, M_i, to convert N_{si} to a vertical column density, N_{vi}:

$$M = N_{si} / N_{vi} , \qquad [\ 3\text{-}1\ ]$$

where M is a function of viewing geometry, geophysical condition (albedo, cloud coverage), and the vertical distribution of the gas. Generally, gas located at lower altitude contributes less to the satellite-measured absorption spectrum since Rayleigh scattering discriminates against its viewing [*Palmer et al.*, 2001]. Algorithms are designed assuming sequential processing of level 1 data products, including spectra, so that higher-level processing will be required in some cases to fully exploit the measurements. The first step is accomplished by a spectral fitting procedure, which will be optimized during the commissioning phase of the OMI instrument, and where various options described below are evaluated. The second step is more complex: HCHO is predominantly a tropospheric species, so that determination of the vertical column abundances requires modeling of the vertical profile shape in the troposphere in order to determine Ms appropriate to specific measurement conditions, as demonstrated for GOME measurements [*Chance et al.*, 2000; *Palmer et al.*, 2001].

3.1. Slant column measurements

The determination of slant column abundances, N_s, is accomplished by fitting the measured radiance I, beginning with the measured irradiance E, molecular absorption cross sections, correction for the Ring effect, effective albedo (which includes the contribution from Rayleigh scattering for these molecules, as discussed in **Air mass factors and vertical column abundances**, below), and a low-order polynomial for closure. This latter term accounts for small

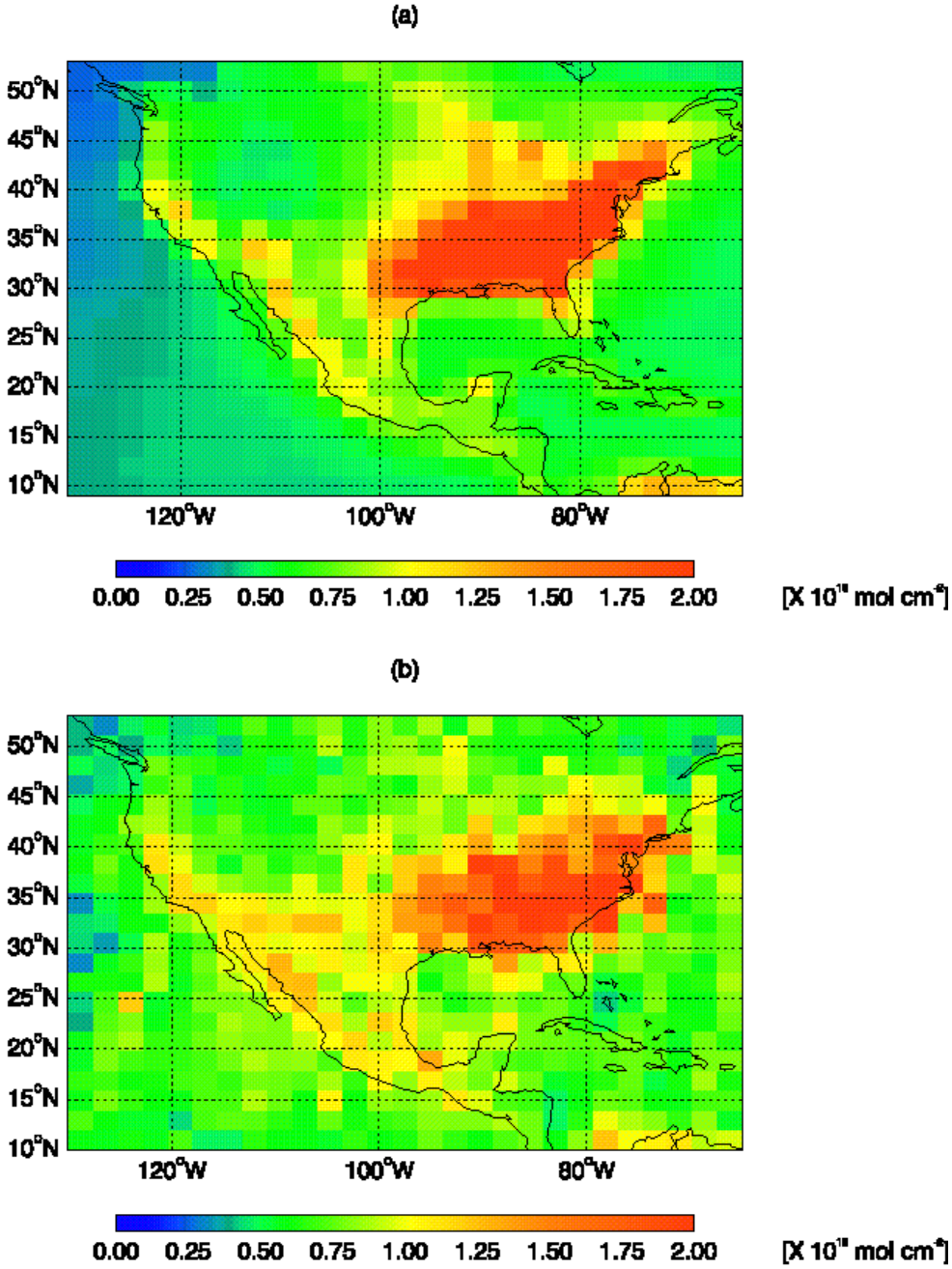

Figure 3.1. (a) Vertical column abundances of HCHO derived from GOME measurements over North America for July 1996;
(b) Modeled result from the GEOS-CHEM 3-dimensional tropospheric chemistry and transport model. The HCHO in this case is primarily due to isoprene oxidation [Chance et al., 2000; Palmer et al., 2001].

remaining differences in Rayleigh scattering versus wavelength over the fitting window, variation of ground albedo, and imperfect intensity calibration of the OMI radiance and irradiance measurements. The overall fitting strategy includes a number of options, which will be fully tested during OMI commissioning, with the ones that have proved most successful in the analysis of previous satellite measurements providing the baseline.

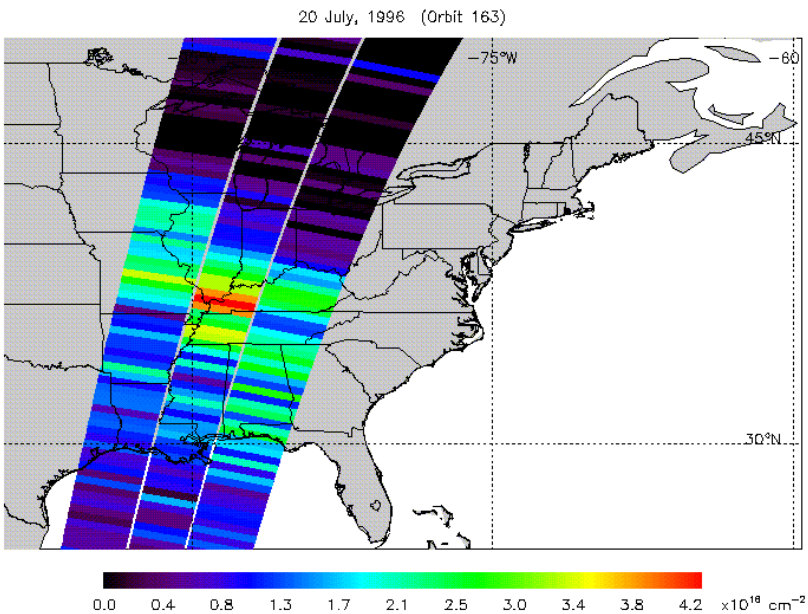

Figure 3.2 Elevated slant columns of HCHO over the Southeastern United States in July 1996. Measurements are from direct fitting of GOME level 1 spectra.

3.1.1. Nonlinear least-squares fitting

The Levenberg-Marquardt nonlinear least-squares fitting procedure (nlls) [*Marquardt*, 1963; *Press et al.*, 1986] is used in several of the subsequent steps in the analysis. In this procedure, the χ^2 merit function

$$\chi^2 = \sum_{i=1}^{N} \left[(y_i - F(x_i;a)) / \sigma_i \right]^2 \qquad [\,3\text{-}2\,]$$

is minimized with respect to the parameters a. The strategy for finding the minimum is to begin with a diagonally-dominant curvature matrix, corresponding to a steepest descent search procedure, and gradually changing continuously over to the inverse-Hessian (curvature) method search procedure as the minimum is neared.

Convergence is reached when χ^2 is less than a pre-set amount, when χ^2 decreases by less than a pre-set amount over several successive iterations, or when all parameters change by less than a pre-set fraction for several successive iterations. Iteration is also halted when the number of iterations reaches a pre-set maximum without successful convergence.

Estimated fitting uncertainties are given as $\sigma_i = \sqrt{C_{ii}}$, where C is the covariance matrix of the standard errors. This definition is strictly true only when the errors are normally distributed. In the case where the level-1 data product uncertainties are not reliable estimates of the actual uncertainties, spectral data are given unity weight over the fitting window, and the 1σ fitting error in parameter i is determined as

$$\sigma_i = \varepsilon_{rms} \sqrt{\frac{C_{ii}\ n_{points}}{n_{points} - n_{varied}}} \qquad [\ 3\text{-}3\ ]$$

where ε_{rms} is the root-mean-squared fitting residual, n_{points} is the number of points in the fitting window, and n_{varied} is the number of parameters varied during the fitting.

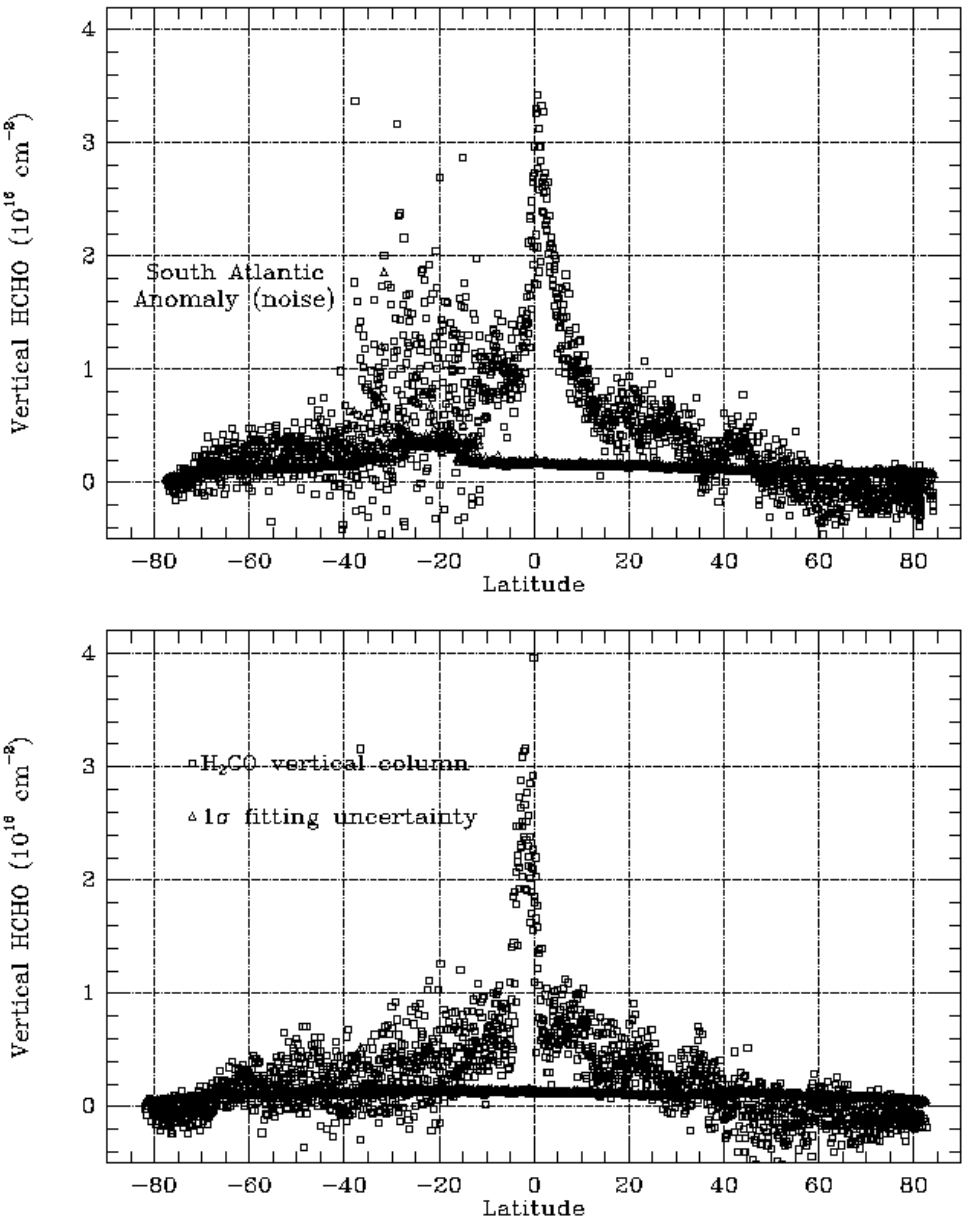

Figure 3.3 Enhanced HCHO as measured by GOME from biomass burning episodes over (a) the northern Amazon basin; and (b) Indonesia during the intense fires of 1997.

3.1.2. Re-calibration of wavelength scales

This is a baseline option, required by the fact that fitting to small root-mean-square differences between the measurements and the modeling (*rms*), comparable to the measurement SNRs requires better wavelength calibration than that provided in the level 1 data products

(wavelength calibration for the specific fitting window is more accurate than that derived for the spectrum as a whole). The model for this procedure comes from the analysis of GOME data [*Caspar and Chance*, 1997; *Chance*, 1998]. The irradiance to be used in the subsequent spectrum fitting is re-calibrated in wavelength over the fitting window by nlls comparison to a high-resolution solar reference spectrum which is accurate in absolute vacuum wavelength to better than 0.001 nm [*Chance and Spurr*, 1997]. A slit width (instrument transfer function) parameter is fitted simultaneously. Radiance spectra are equivalently fitted, with the slit width parameter frozen to the values (versus CCD spectral field) determined in fitting the irradiance: Since the window regions for these four molecules are optically thin in all Telluric absorptions and contain only a few percent of inelastically-scattered Fraunhofer spectrum (Ring effect), the procedure works almost as well on radiances as on irradiances. Experience with GOME spectra (which are at higher spectral resolution) is that both are fitted to within about 1/50 spectral resolution element. Re-calibration normally involves only the determination of a single wavelength shift parameter for the fitting window (baseline option); inclusion of a wavelength "squeeze" parameter is a non-baseline option. The case for OMI is complicated by the fact that such calibrations are made for the separate spectral fields on the CCD detector array (GOME has linear Reticon detectors, which measure single spectra).
Wavelength calibrations are made for each OMI orbit as follows:

1. The set of irradiances, versus CCD position are calibrated in wavelength over the fitting window;
2. One set of radiances versus CCD position, selected by an input parameter, usually in the middle of the orbit, are calibrated in wavelength over the fitting window. This calibration is applied as the initial wavelength scale for all radiances in the orbit;
3. Further fine-tuning of the relative calibration of all radiances through the orbit to the irradiance is performed during the detailed spectrum fitting, as described below (baseline option).

3.1.3. Reference spectra

Reference spectra are degraded to the OMI resolution either in pre-tabulated form (baseline option) or using the parameterized slit function determined during the irradiance calibration (non-baseline option). They are then re-sampled to the radiance wavelength grid, using cubic spline interpolation [*Press et al.*, 1986]. The current baseline choices for reference spectra to fit HCHO are shown in Figure 3.4:

- HCHO cross sections *Cantrell et al.*, 1990.
- NO_2 cross sections *Vandaele et al.*, 1997.
- BrO cross sections *Wilmouth et al.*, 1999.
- OClO cross sections *Wahner et al.*, 1987 (corrected to vacuum wavelength).
- O_3 cross sections *Burrows et al.*, 1999.
- O_2-O_2 collision complex *Greenblatt et al.*, 1990 (corrected to vacuum wavelength).
- Ring effect: Determined specifically for OMI applications by J. Joiner *et al.*
- Undersampling correction: Calculated dynamically, if required

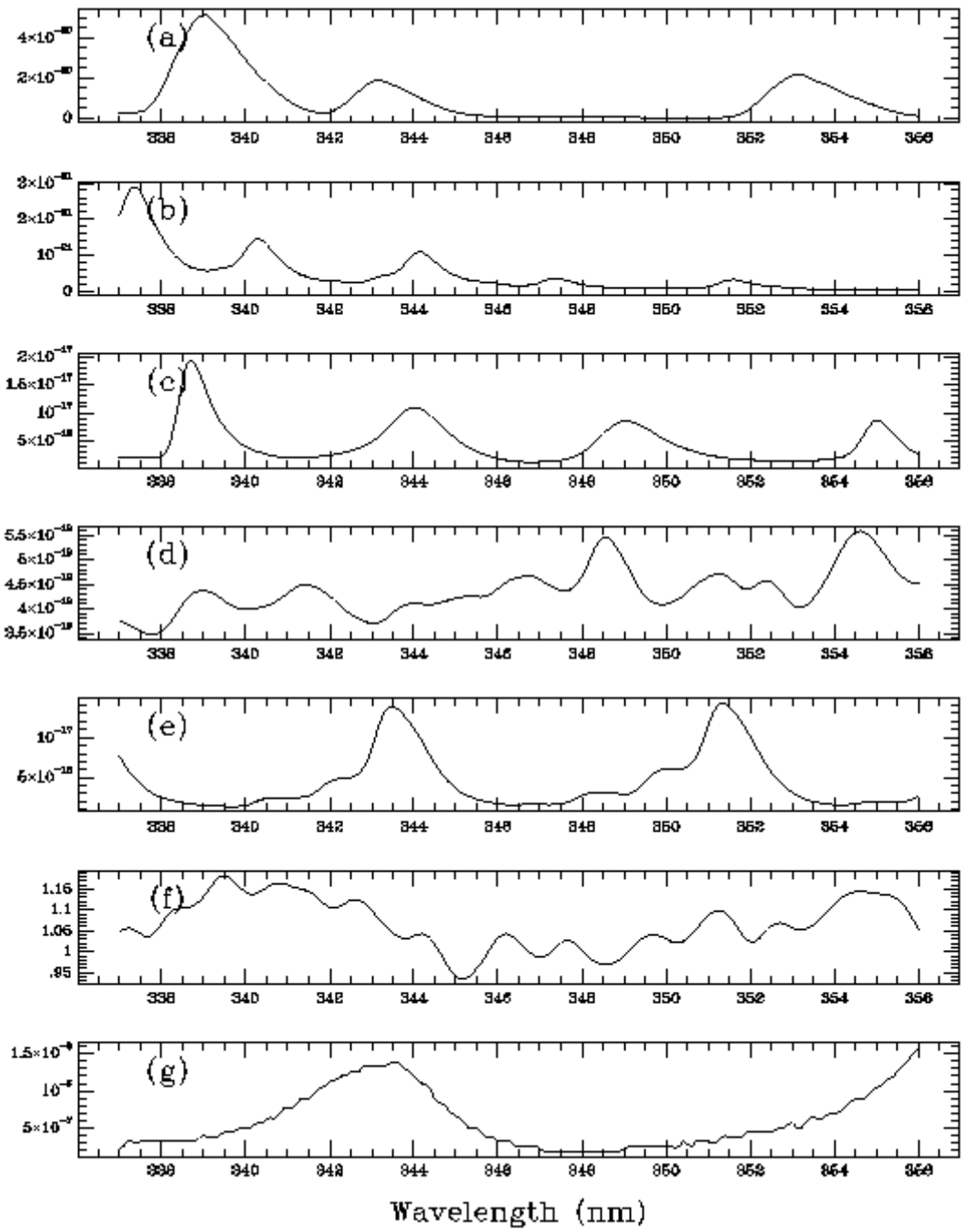

Figure 3.4 Reference spectra for fitting to determine slant column abundances of HCHO: (a) HCHO; (b) O_3; (c) BrO; (d) NO_2; (e) OClO; (f) O_2-O_2 collision complex; (g) Ring effect.

Fitting of GOME spectra gave systematic residuals that were much larger than the absorption of the trace gases until it was discovered that these are due to spectral undersampling by the instrument. High frequency spectral information is aliased into the spectrum when irradiances are re-sampled to the radiance wavelength scale (irradiances for GOME, and for OMI, are measured at slightly different Doppler shifts with respect to the sun) [*Chance*, 1998; *Slijkhuis et al.*, 1999]. The algorithm for OMI includes a non-baseline option (since OMI is not anticipated to significantly undersample) for calculating undersampling corrections at the time of

reference spectrum sampling. This is accomplished by taking the high-resolution Fraunhofer reference spectrum, convolved with the instrument transfer function (as determined during the irradiance spectral calibration), which constitutes an oversampled irradiance and forming properly-sampled and undersampled representations of it, using cubic spline interpolation. The difference between the representation is the undersampling correction; for GOME this constitutes ca. 90% of the systematic residual.

3.1.4. Common-mode correction

Remaining systematic residuals which are, by definition, uncorrelated to the trace gas spectra may be averaged and included in the spectrum fitting as a ``common-mode" spectrum, to reduce the fitting *rms* and, proportionally, the fitting uncertainties. This is included as a non-baseline option for OMI. For GOME, this reduces the *rms* by about a factor of two for BrO and a factor of 3 for NO_2. The presumption is that the undersampling correction only imperfectly models the instrument transfer function and thus leaves some remaining systematic effects. Comparisons with GOME measurements of NO_2 for clean maritime (mostly stratospheric NO_2) conditions show that this reduced uncertainty is the appropriate choice.

3.1.5. Radiance fitting: BOAS (baseline option)

The radiance is nlls fitted to a modeled spectrum which includes the irradiance, and effective albedo, trace gas concentrations, Ring effect correction, and a low-order polynomial (up to cubic) closure term:

$$I(\lambda) = AE(\lambda)e^{-N_{s1}\sigma_1(\lambda)}\cdots e^{-N_{sn}\sigma_n(\lambda)} + c_R\sigma_R + c_0 + c_1(\lambda-\bar{\lambda}) + c_2(\lambda-\bar{\lambda})^2 + c_3(\lambda-\bar{\lambda})^3 \qquad [3\text{-}4]$$

The σ_i are the absorption cross sections, σ_R is the Ring effect correction, and the $c_0 - c_3$ are the coefficients of the closure polynomial. Each parameter may be individually selected to be varied during the fitting or frozen at a constant value.

The determination of slant column abundances for HCHO is analogous to that for BrO and OClO except for the following difference: Because of the weakness of the HCHO absorption and the correlation with other spectral features in the HCHO fitting window, the HCHO fitting will be made with fixed values of BrO and O_3 that have been previously fitted for the corresponding OMI spectra (baseline option). BrO values will come from the BrO trace gas fitting algorithm. O_3 slant column values will either come from the OMI O_3 total column algorithm, or will be fitted separately for the present purpose (TBD). The baseline is then to vary A, N_s (HCHO), N_s (NO_2), N_s (O_2-O_2), C_R, and $c_0 - c_3$. The non-baseline option to vary BrO and O_3 will be possible as well. In addition, there will be a baseline option to correct the fixed O_3 slant column values for the difference in viewing due to Rayleigh scattering for O_3 in the O_3 window and the HCHO window. The baseline fitting window is 337-356 nm. In addition, the linear wavelength scale of the irradiance is allowed to vary (baseline option) to correct for small wavelength changes in the radiance over the orbit. While it is actually the radiance scale that requires adjustment, the relative change in wavelength scale is much smaller than the instrument resolution or the variation of measurable features in the reference or Ring spectra: adjustment of the irradiance scale avoids changing the measured quantity (the radiance) during the fitting process.

Smoothing (low-pass filtering) of the irradiances, radiances, and reference spectra is included as a non-baseline option. This procedure provides an alternate means to correct for spectral undersampling effects. It is implemented by applying a running 5-point filter (1/16, 1/4, 3/8, 1/4, 1/16) to each of the spectra.

Updating of the fitting parameters is included as a baseline option: For each spectrum after the first in a particular spectrum field of the CCD, the initial guesses for fitting parameters are updated to those fitted to the previous spectrum.

3.1.6. Radiance fitting: DOAS (non-baseline option)

This option converts the direct (BOAS) fitting of radiances to the DOAS method. The logarithm of the radiance divided by the irradiance is taken and the result high-pass filtered by the subtraction of a low-order polynomial (up to cubic, with the actual number of terms determined by the input parameter file):

$$H\left[ln(I/E)\right] = -N_{s1}H(\sigma_1) - \cdots - N_{sn}H(\sigma_n) + c_{R1}\,H(\sigma_{R1}/F) + c_{R2}\,H(\sigma_{R2}/F) + HOT, \qquad [3\text{-}5]$$

where H denotes high-pass filtering. The coefficients of the polynomial are determined by linear fitting to ln (I/E) [*Press et al.*, 1986]. Reference cross sections sampled at the OMI wavelength scale are also high pass filtered by subtraction of a low-order polynomial. The Ring effect correction is divided by the irradiance for each spectral field and the result high-pass filtered as well (note that this determines the first term in the expansion for the logarithmic quantity which includes the Ring effect; higher-order terms are not included - see Equation [1-4]). The fitting is then entirely analogous to the BOAS fitting, except that the fitted quantity is now H ln (I/E).

If the radiance/irradiance wavelength adjustment is not selected, then the DOAS fitting would be linear in the fitting parameters. However, since wavelength adjustment and BOAS fitting are both baseline options, it is not currently planned to implement separate linear fitting for this case; the additional computer time in fitting the linear case with the nonlinear method is inconsequential, and the results are virtually identical.

3.2. Air mass factors and vertical column abundances

HCHO is assumed to be primarily tropospheric, with Ms that depend heavily on the vertical distribution and the geophysical conditions [*Palmer et al.*, 2001]. Ideally, air mass factors appropriate to vertical distributions of HCHO for the measurement time and geophysical conditions would be used for operational processing. These are determined using results from the GEOS-CHEM global 3-D model of tropospheric chemistry and transport [*Bey et al.*, 2001] and are calculated using the SAO LIDORT radiative transfer model [*Spurr et al.*, 2001; *Chance et al.*, 2000; *Palmer et al.*, 2001]. LIDORT is designed to deliver both intensities and weighting functions. LIDORT solves the radiative transfer equation in a multi-layered atmosphere with multiple-scattering using the discrete ordinate method. The model contains a full internal perturbation analysis of the intensity field, allowing all weighting functions to be derived analytically to the same level of accuracy specified for the intensity. Although LIDORT has been designed primarily as a general forward model tool for non-linear atmospheric retrieval problems, the calculation of Ms is a straightforward application of the model. A single call to LIDORT will deliver both the top-of-the-atmosphere upwelling intensity I_B and the corresponding set of weighting functions $K(z)$ required for the M determination.

The baseline option for HCHO processing assumes that the necessary assimilated data for GEOS-CHEM modeling, and the modeled results for HCHO vertical columns, are not available operationally. Air mass factors are determined from a lookup procedure, where Ms are pre-calculated as functions of location and season (and, hence, albedo), and viewing geometry. In order to simplify the lookup process, the viewing geometry is parameterized by the effective solar zenith angle ($ESZA$), where

$$\sec(ESZA) = \sec(SZA) + \sec(LOSZA) - 1, \qquad [3\text{-}6]$$

where *SZA* is the solar zenith angle of the measurement and *LOSZA* is the line-of-sight zenith angle, and azimuthal dependence of *M* is ignored. Experience with fitting GOME data shows that, except for the highest solar zenith angles, above 80°, this procedure adds negligible additional error. The lookup procedure requires a database of albedo values (TBD - it may be taken from those developed using GOME data at the KNMI and the SAO, or eventually determined from OMI data itself, after cloud analysis).

The variations of *M* with albedo and with wavelength over the fitting window are included as error terms. An additional *ESZA*-dependent error contribution of up to 20% is included to account for the variation of the profile of stratospheric/upper tropospheric HCHO from the selected shape.

3.3. Error estimates

Estimated errors are given for a ground footprint of 40·40 km^2, which has been adopted as the standard for reporting OMI error estimates within EOS. S/N values for estimating fitting uncertainties come from the OMI-EOS Instrument Specification Document RS-OMIE-0000-FS-021, Tables 5.5 and 5.6, and are applied to he best fitting knowledge from GOME analysis, taking into account the difference in spectral resolution. All uncertainties are given here as 1σ.

The 1σ fitting error in parameter *i* is determined as

$$\sigma_i = \sqrt{C_{ii}} + \delta BrO + \delta O_3 \qquad [3\text{-}7]$$

or

$$\sigma_i = \varepsilon_{rms} \sqrt{\frac{C_{ii}\ n_{points}}{n_{points} - n_{varied}}} + \delta BrO + \delta O_3 , \qquad [3\text{-}8]$$

As discussed in Section 3.1.1., *C* is the covariance matrix of the standard errors. Equations [3-7] and [3-8] include the contribution from correlation of fitted parameters, and additional contributions δBrO and δO_3 for the uncertainties in the previously-fitted N_s (BrO) and N_s (O_3) and the correlations of the BrO and O_3 concentrations to the HCHO. This contribution is determined from a lookup procedure based upon finite difference studies. The published uncertainties of the absorption cross sections are added to this in quadrature to obtain the final slant column fitting uncertainties. The fitting precision for biogenically-enhanced conditions is 9%. δBrO and δO_3 are TBD, but are estimated here as 5% each, for a total slant column fitting uncertainty of 11%.

The uncertainty in the cross sections, including temperature dependence, is 10%, for a total slant column uncertainty, in biogenically-enhanced conditions, of 15%.

The uncertainty in *M* is added in quadrature to obtain the final vertical column fitting uncertainties. The uncertainty in *M* due to assumptions on the vertical profile shape is 20%, worst case [*Palmer et al.*, 2001]. Effects on *M* due to cloud parameter uncertainties and albedo uncertainties are TBD, but are assumed for the present to be negligible compared to assumptions on the vertical profile shape (these effects will be addressed in detail when the cloud uncertainties and albedo database uncertainties have been quantified).

The total error for the vertical column uncertainty under biogenically-enhanced conditions is then 15% + 20% = 25%. The error excluding the systematic contribution from cross sections uncertainties is 22%, corresponding to $3.5 \cdot 10^{15}$ cm^{-2} vertical column density. This can be compared to the requirement in the Science Requirements Document for OMI-EOS (RS-OMIE-KNMI-001, Version 2) of 10^{15} cm^{-2}. The detection limit, only considering fitting uncertainty, is

$1.8 \cdot 10^{15}$ cm^{-2} vertical column density. Thus, meeting the Science Requirement Document specification will require improvement in S/N over that given in the Instrument Specification Document as well as *M*s with greater accuracy.

3.4. Outputs

Standard outputs include:

- Slant column abundance and 1σ fitting uncertainties for HCHO and the other species varied in the fitting window;
- Correlation of other fitted species to HCHO (from off-diagonal elements of the covariance matrix of the standard errors);
- Fitting *rms*;
- Convergence flags and number of iterations (successful? which convergence criterion?)
- Geolocation information;
- Version numbers of algorithm and parameter input file;
- Vertical column abundances and 1σ uncertainties.

3.5. Validation

HCHO slant and vertical column densities are currently measured by GOME [*Thomas et al.*, 1998; *Chance et al.*, 2000; *Palmer et al.*, 2001] and will be measured by SCIAMACHY. Ground- and aircraft-based measurement campaigns will be necessary for OMI validation, especially when concentration are expected to be high, *i.e.,* for periods with strong tropospheric hydrocarbon emissions. A past example is the U.S. Southern Oxidants Study (SOS), measuring continental production of HCHO from isoprene [*Lee et al.*, 1998]. Measurements are also necessary to confirm rates of production in the maritime free troposphere, such as those from the 1997 Subsonic Assessment (SASS) Ozone and Nitrogen Oxide Experiment (SONEX) [*Singh et al.*, 2000]. Measurements over the southeastern U.S. in summertime, and over the midlatitude oceans (preferably in summertime for maximum production from oxidation of CH_4) would provide optimum data sets. Midlatitude maritime measurements could be combined with campaigns to study intercontinental pollution transport.

3.6. References

Bey I., D.J. Jacob, R.M. Yantosca, J.A. Logan, B. Field, A.M. Fiore, Q. Li, H. Liu, L.J. Mickley, and M. Schultz, Global modeling of tropospheric chemistry with assimilated meteorology: Model description and evaluation, J. Geophys. Res., submitted, 2001.

Burrows, J.P., A. Richter, A. Dehn, B. Deters, S. Himmelmann, S. Voigt, and J. Orphal, Atmospheric remote sensing reference data from GOME - 2. Temperature-dependent absorption cross-sections of O_3 in the 231-794 nm range, J. Quant. Spectrosc. Radiat. Transfer 61, 509-517, 1999.

Cantrell, C.A., J.A. Davidson, A.H. McDaniel, R.E. Shetter, and J.G. Calvert, Temperature-dependent formaldehyde cross sections in the near-ultraviolet spectral region, J. Phys. Chem. 94, 3902-3908, 1990.

Caspar, C., and K. Chance, GOME wavelength calibration using solar and atmospheric spectra, *Proc. Third ERS Symposium on Space at the Service of our Environment*, Ed. T.-D. Guyenne and D. Danesy, European Space Agency publication SP-414, ISBN 92-9092-656-2, 1997.

Chance, K.V., J.P. Burrows, and W. Schneider, Retrieval and molecule sensitivity studies for the Global Ozone Monitoring Experiment and the SCanning Imaging Absorption spectroMeter for Atmospheric CHartographY, *Proc. S.P.I.E., Remote Sensing of Atmospheric Chemistry*, 1491, 151-165, 1991.

Chance, K., and R.J.D. Spurr, Ring Effect Studies: Rayleigh Scattering, Including Molecular Parameters for Rotational Raman Scattering, and the Fraunhofer Spectrum, Appl. Opt. 36, 5224-5230, 1997.

Chance, K., Analysis of BrO Measurements from the Global Ozone Monitoring Experiment, Geophys. Res. Lett. 25, 3335-3338, 1998.

Chance, K., P.I. Palmer, R.J.D. Spurr, R.V. Martin, T.P. Kurosu, and D.J. Jacob, Satellite Observations of Formaldehyde over North America from GOME, Geophys. Res. Lett. 27, 3461-3464, 2000.

Greenblatt, G.D., J.J. Orlando, J.B. Burkholder, and A.R. Ravishankara, Absorption measurements of oxygen between 330 and 1140 nm, J. Geophys. Res. 95, 18,577-18,582, 1990.

Lee Y.-N., *et al.*, Atmospheric chemistry and distribution of formaldehyde and several multioxygenated carbonyl compounds during the 1995 Nashville/Middle Tennessee Ozone Study, J. Geophys. Res. 103, 22,449-22,462, 1998.

Marquardt, D.L., An algorithm for least-squares estimation of non-linear parameters, J. Soc. Indust. Appl. Math. 2, 431-441, 1963.

Palmer, P.I., D.J. Jacob, K. Chance, R.V. Martin, R.J.D. Spurr, T.P. Kurosu, I. Bey, R. Yantosca, A. Fiore, and Q. Li, Air Mass Factor Formulation for Spectroscopic Measurements from Satellites: Application to Formaldehyde Retrievals from GOME, J. Geophys. Res. 106, 14,539-14,550, 2001.

Press, W.H., B.P. Flannery, S.A. Teukolsky, and W.T. Vetterling, *Numerical Recipes*, ISBN 0-521-30811-9, Cambridge University Press, 1986.

Singh, H., *et al.*, Distribution and fate of selected oxygenated organic species in the troposphere and lower stratosphere over the Atlantic, J. Geophys. Res. 105, 3795-3805, 2000.

Slijkhuis, S., A. von Bargen, W. Thomas, and K. Chance, Calculation of undersampling correction spectra for DOAS spectral fitting, *Proc. ESAMS'99 - European Symposium on Atmospheric Measurements from Space*, 563-569, 1999.

Spurr, R.J.D., T.P. Kurosu, and K. Chance, A linearized discrete ordinate radiative transfer model for atmospheric remote sensing retrieval, J. Quant. Spectrosc. Radiat. Transfer 68, 689-735, 2001.

Thomas, W., E. Hegels, S. Slijkhuis, R. Spurr, and K. Chance, Detection of biomass burning combustion products in Southeast Asia from backscatter data taken by the GOME spectrometer, Geophys. Res. Lett. 25, 1317-1320, 1998.

Vandaele A.C., C. Hermans, P.C. Simon, M. Carleer, R. Colin, S. Fally, M.F. Mérienne, A. Jenouvrier, and B. Coquart, Measurements of the NO_2 absorption cross-section from 42000 cm^{-1} to 10000 cm^{-1} (238-1000 nm) at 220 K and 294 K, J. Quant. Spectrosc. Radiat. Transfer 59, 171-184, 1998.

Wahner, A., G.S. Tyndall, and A.R. Ravishankara, Absorption cross sections for OClO as a function of temperature in the wavelength range 240-480 nm, J. Phys. Chem. 91, 2734-2738, 1987.

Wilmouth, D.M., T.F. Hanisco, N.M. Donahue, and J.G. Anderson, Fourier transform ultraviolet spectroscopy of the $A\ ^2\Pi_{3/2} \leftarrow X\ ^2\Pi_{3/2}$ transition of BrO, J. Phys. Chem. 103, 8935-8945, 1999.

4. SO_2

A.J. Krueger, Joint Center for Earth Systems Technology
N. A. Krotkov, Goddard Earth Science Technology Center
University of Maryland, Baltimore County

4.1. Introduction

Sulfur dioxide releases in the Earth's atmosphere are always transient because of chemical conversion to sulfate with time scales of hours in the boundary layer to weeks in the stratosphere. Volcanic sulfur dioxide clouds are easy to measure because they are at high altitudes, large, and have long lifetimes. Passive degassing and SO_2 from anthropogenic pollution (e.g., burning of coal), is more difficult to measure as the gas is contained in the boundary layer below the mean level of penetration for UV sunlight. These background sources are important to measure because they contribute more to the global annual sulfur budget than explosive eruptions. Model calculations [*Chin et al*., 2000] of background SO_2 column amounts are shown in Figure 4.1 and compared with far larger amounts measured with TOMS [*Krueger et al.,* I 2000] from four large volcanic eruptions (yellow colors).

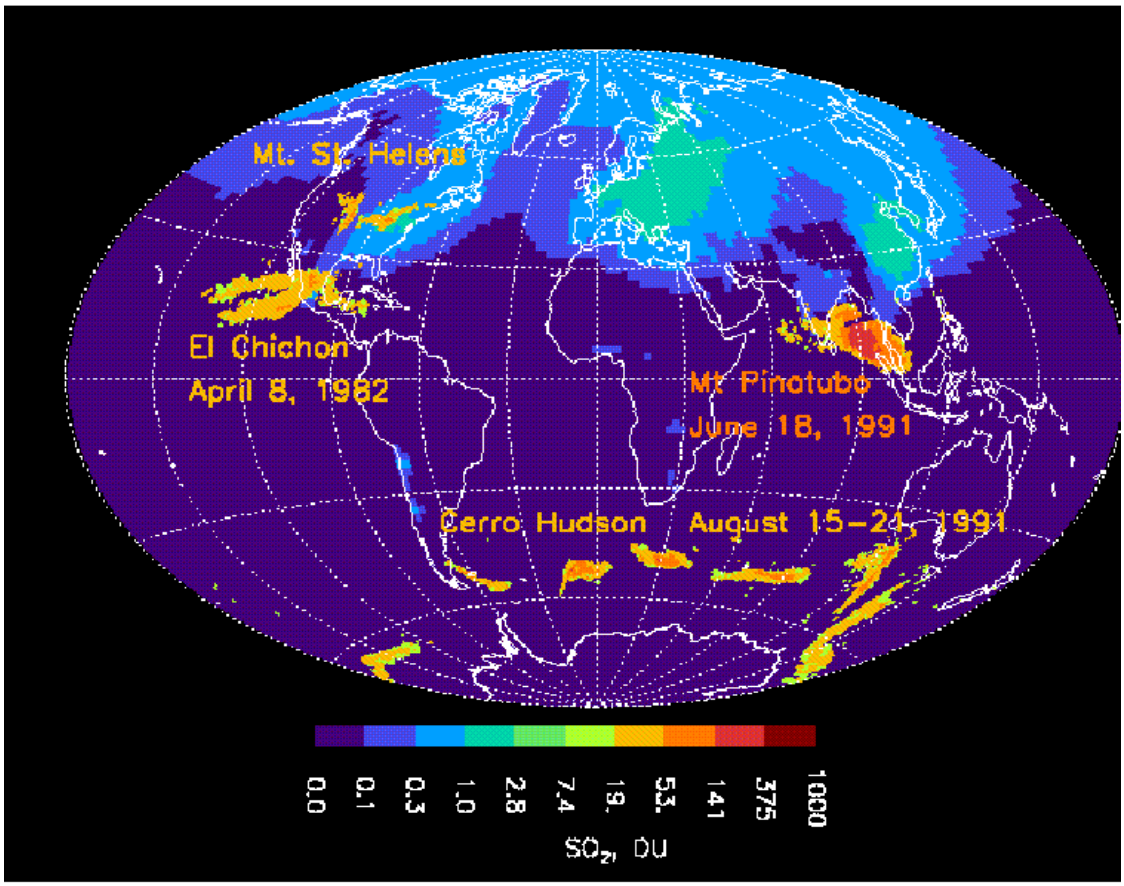

Figure 4.1 Global monthly map of air pollution SO_2 from GOCART model [Chin et al., 2000] superimposed on global composite map of several volcanic SO_2 eruption clouds measured by TOMS [Krueger et al., 2000].

4.1.1. Volcanic SO_2

Volcanic eruptions have been considered an important factor in climate change ever since abnormal weather was observed to follow major eruptions. The factor for forcing climate was suspected to be stratospheric sulfate aerosols from sulfur dioxide rather than the more obvious volcanic ash because of the long-lasting effects. This hypothesis could not be validated quantitatively because no means was available for measuring the amount of sulfur lofted into the stratosphere until the era of satellites. For the first time the sulfur dioxide output for all sizes of magmatic eruptions could be measured with the TOMS instrument [*Krueger*, 1983; *Krueger et al.*, 2000] because of its contiguous mapping ability. No other instrument or technique has ever approached this unique record. The 14-year Nimbus 7 TOMS mission captured every eruption since 1978 greater than 10 kt SO_2, including 2 super-sized eruptions. The 1991 eruption of Mt. Pinatubo is believed to be the largest of the century in sulfur output (20 Mt), although only indirect estimations exist for eruptions prior to 1978, so this issue may never be resolved. Follow-on TOMS missions (Meteor-3, ADEOS, Earth Probe) have extended the record to 21 years (with an 18 month gap in 1995-6, which may be partially filled using GOME data *[Burrows et al*., 1993*, Burrows et al.,* 1999],). The uncertainty in the average annual flux of sulfur from eruptions [*Bluth*, *et al.*, 1993; *Bluth et al.*, 1997] has been reduced from 100% to 30%. This average is representative of the late 1900's but is greatly influenced by the occurrence of large eruptions in the database. This database will continue with QuikTOMS and OMI, as the successor to TOMS. The OMI mission could extend the volcanic record through the next decade when the NPOESS instruments are expected to operationally measure volcanic eruptions.

4.1.2. Anthropogenic SO_2

The small column amounts of air pollution SO_2 predicted from the model shown in figure 4.1 are a major challenge for satellite instruments. However, column abundances less than 2.6 Dobson Units (DU, 1 DU = $2.6868 \cdot 10^{16}$ cm^{-2}) due to the burning of sulfur-rich lignite coal in Southeastern Europe [*Eisinger and Burrows*, 1998] have already been measured in winter conditions by GOME. This result was due to GOME's high signal to noise ratio in spite of its large footprint which dilutes the signal from point sources. With OMI's smaller footprint and comparable sensitivity (ca. 0.4 DU vertical column abundance) it will be possible to observe many of the sources of anthropogenic sulfur dioxide and begin to build a satellite base inventory.

4.1.3. Volcanic ash measurements

Ash is present in some volcanic clouds, particularly from explosive eruptions, and affects the radiative transfer path significantly. Sulfur dioxide retrievals that ignore the ash produce serious overestimates depending on the ash optical depth (Krueger et al., 1995). The optical depth depends on the index of refraction of the ash which varies significantly between volcanoes and eruptions. Fortunately, the presence of ash clouds is identified in the OMI data by discrimination from Rayleigh scattering using the UV absorbing aerosol index (AAI) at 340/380 nm wavelength pair [*Seftor et al.*, 1997; *Krotkov et al.*, 1999a] or distance from the Rayleigh curve on the spectral slope-reflectivity diagram [*Krotkov et al.*, 1997a]. Quantitative algorithms were developed to compute ash optical thickness, effective particle size, and column mass [*Krotkov et al.*, 1999a,b]. These will be enhanced taking advantage of the broader spectral span of OMI to determine water/ice presence. With the ash specified we will produce tables incorporating the particular ash properties for reprocessing of the volcanic cloud data.

4.2. Selection of optimum spectral region

The optimum spectral region for SO_2 retrievals is determined from the differential radiance due to added SO_2 compared with the noise radiance of the instrument. Figure 4.2 is an example of the differential radiance (blue curves) due to the addition of 1 DU of SO_2 in the stratosphere (20 km) or in the boundary layer (1 km) at midlatitude conditions. An order-of-magnitude loss of sensitivity at the lesser altitude is very apparent. However, the optimum spectral region between 310 and 320 nm remains nearly the same. When the differential radiance is compared with the expected OMI noise (red curve) based on OMI Demonstration Model data [*DeVries*, 2000] for minimum radiance conditions (clear sky) the radiance exceeds.

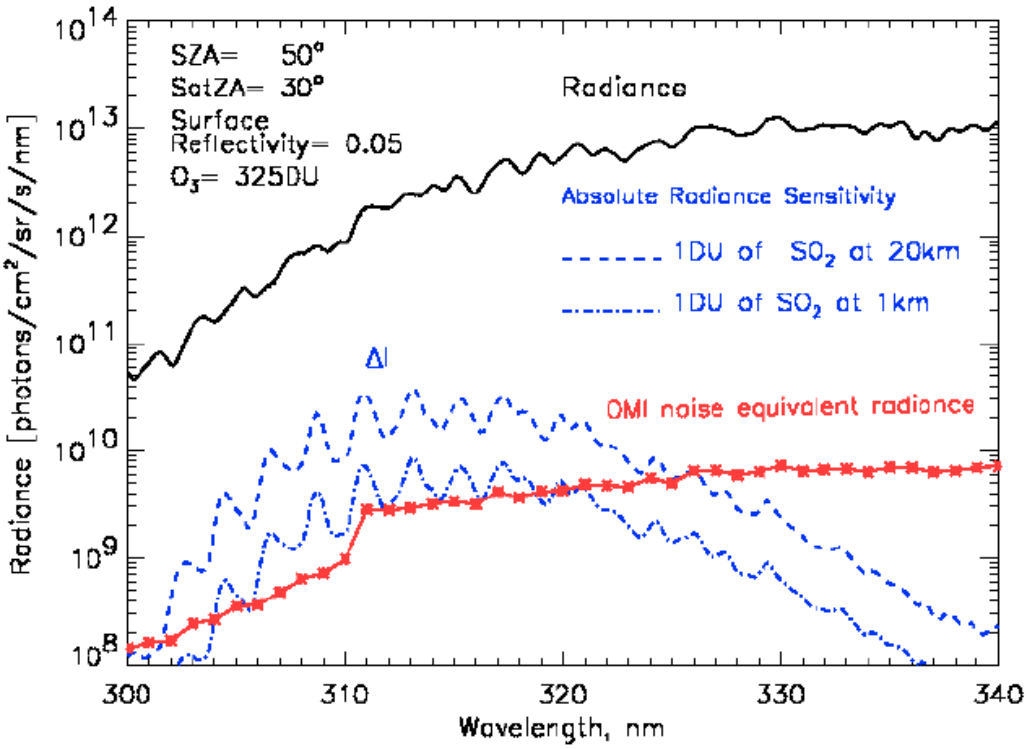

Figure 4.2 Selection of optimum wavelength region for SO_2 determination at midlatitudes with clear sky. Radiance of the midlatitude atmosphere (black curve) and differential radiance due to SO_2 layers (blue curves) compared with the noise radiance of OMI (red curve).

the noise radiance only for wavelengths less than 320 nm. The break in the noise curve at 310 nm located at the intersection of the UV-1 and UV-2 channels is near the middle of the optimum spectral region. However, differing ground footprints prevent direct combination of the two channels. The UV-2 channel at 310-317 nm is preferred for air pollution source data because of the smaller footprint; whereas the UV-1 channel at 305-310 nm has a greater signal above the noise. Thus, dual processing may be required

Ozone absorption varies strongly across the optimum spectral regions of both channels and the use of air mass factors is problematic. The algorithm described in the next section makes use of wavelength dependent paths as an implicit part of radiative transfer tables.

4.3. Detailed Descriptions of the SO_2 algorithm

4.3.1. Inversion strategy

For OMI we have developed an approach which combines the TOMS and DOAS techniques. The general description of the algorithm (data flow) is shown in Figure 4.3.

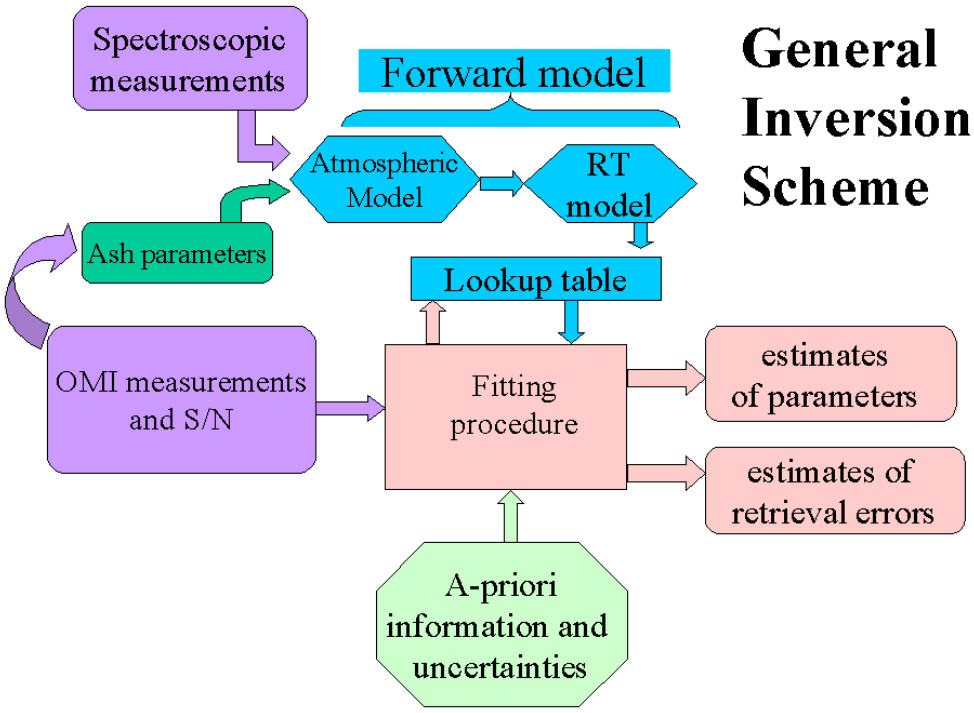

Figure 4.3 SO_2 inversion flowchart

The SO_2 inversion strategy is based on the statistical approach given by *Dubovik and King* [2000]. The strategy is to consider OMI measurements together with a climatological data as a single set of multi-source data. The inversion technique is designed as a search for the best overall fit of all data considered by our forward model (in a least-squares sense) taking into account different accuracies of the fitted (measured and a priori) data. The basic model contains the terms:

$$\begin{cases} N_k^*(\lambda) = N_k(\lambda;\Sigma;\Omega) + \Delta_k^S(\lambda) + \Delta_k^R(\lambda) = N(\lambda;\Sigma;\Omega) + \Delta_k^S(\lambda) + \Delta_k^R(\lambda) \\ \Sigma^* = \Sigma + \Delta_{\Sigma^*} \\ \Omega^* = \Omega + \Delta_{\Omega^*} \end{cases} \qquad [\,4\text{-}1\,]$$

$N_k^*(\lambda)$ - OMI measured N values: $N_1^*(\lambda) = -100\ \log_{10}\left(\frac{I}{F}\right)$; (k=1 for UV1 and k=2 for UV2)

Σ - the concentration of SO_2, Σ^* - a priori estimate of the concentration of SO_2;
Ω, - the concentration of O_3, Ω^* - a priori estimate of the concentration of O_3;

Asterisks denote that the data are measured (or known) with some uncertainty, Δ_k: Δ^S_k and Δ^R_k are the systematic and random N value errors, and $\sigma^2_{\Delta_\Sigma}$ and $\sigma^2_{\Delta_\Omega}$ denote the variances in a priori

SO_2 and O_3 estimates. For discrete spectral measurements, $N_k^*(\lambda)$ is considered as a vector and Eq. [4-1] can be solved numerically. We assume that systematic N value errors (including aerosol and cloud effects) in Equation [4-1] can be described by a 2nd degree spectral polynomial plus known high frequency terms (Ring effect): $\Delta^S_k = a_k + b_k(\lambda-\lambda_0) + c_k(\lambda-\lambda_0)^2 + Ring(\lambda) + \ldots$. We also assume that random N value errors (Δ^R_k) are distributed normally with zero means and known covariance matrices and variances, Δ^R_k.

To achieve the statistically optimum solution, $\mathbf{x} = [\Sigma, \Omega, a_k, b_k, c_k,]$, we solve Equations [4-1] using the Maximum Likelihood approach. The solution of Equations [4-1] is performed using a least-squares fitting method with weighting $(S/N)^{-2}$ $(\lambda, S(\lambda))$. The a priori ozone and SO_2 data supplement the OMI radiance data, with their relative contribution (Lagrange multipliers) weighted according to the ratio of the variances of the measurements and a-priori estimates: $\gamma_\Omega = \Delta^R_k / \sigma^2_{\Delta_\Omega}$ and $\gamma_\Sigma = \Delta^R_k / \sigma^2_{\Delta_\Sigma}$.

4.3.2. Forward model

Detailed radiative transfer calculations are used to build lookup tables of $N(\lambda,\Sigma,\Omega)$ of backscattered radiances in the 305 to 340nm spectral region at the OMI spectral resolution as a function of O_3 and SO_2 vertical profiles (Figure 4.4) and the conditions of the measurement: geometry, surface/cloud pressure, reflectivity and latitude.

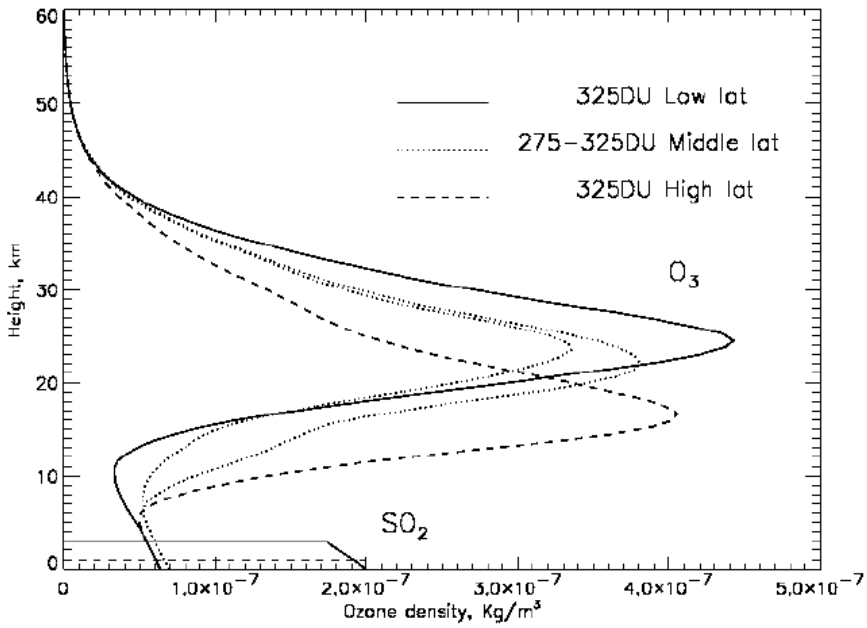

Figure 4.4 Forward model: ozone and background sulfur dioxide profiles

The inversion algorithm works with an arbitrary set of OMI wavelengths within 300-310 and 310 - 330 nm fitting windows, which can range from just four "TOMS-like" wavelengths to the full range of wavelengths at the highest OMI spectral resolution. Like the TOMS algorithm (and OMI standard ozone algorithm), the clouds, aerosols and surface albedo variations within OMI FOV are treated implicitly in the forward model through the concept of Lambertian Equivalent Reflectivity (LER) (known from the OMI column ozone algorithm). The radiances and sensitivity functions to tropospheric SO_2 are pre-calculated for two constant mixing ratio SO_2 vertical profiles: a) from the ground to 900 mbar and b) from the ground to 700 mbar (Fig.

4.4). When high SO_2 amounts are found, they are assumed to be volcanic and will use precomputed tables for an SO_2 layer at 15 km.

Absorption cross sections in the near UV of ozone and sulfur dioxide are shown in Fig. 4.5 together with the ratio of the cross sections. Both ozone and SO_2 cross-sections are temperature dependent. Therefore, for best accuracy we have to address the geographical and seasonal changes in the boundary layer temperature. In addition, the air temperature drops with altitude. We presently assume that explosive volcanic clouds rise to the tropopause where the temperature is near 210K. Sulfur dioxide cross sections at 210 and 295K are taken from McGee and *Burris* [1987], augmented by *Manatt and Lane* [1993] at wavelengths longer than 320 nm. Current work at intermediate temperatures by J. Halpern will be used when published

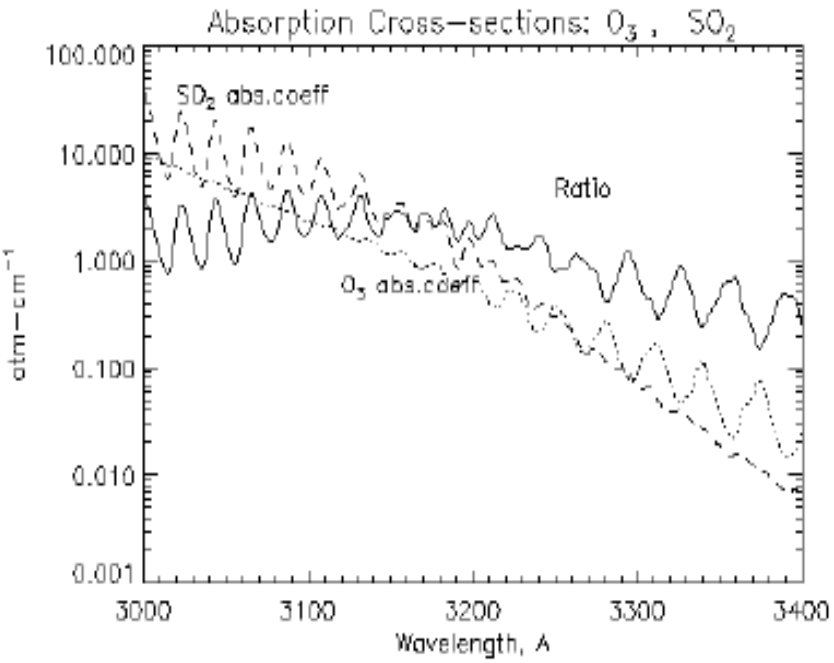

Figure 4.5 Ozone and sulfur dioxide cross sections

4.3.3. Inversion technique

General solution of non-linear system of Eq.(4-1) can be re-written as follows (this is given for clarity of the algorithm):

$$\mathbf{f}^* = \mathbf{f}(\mathbf{x}) + \Delta. \qquad [\,4\text{-}2\,]$$

Since Eq. [4-2] is non-linear, we solve it iteratively on the basis of Taylor expansion in small vicinity at each step:

$$\mathbf{x}^{p+1} = \mathbf{x}^{p} - t_p \Delta\mathbf{x}^{p}, \qquad [\,4\text{-}3\,]$$

where $\Delta\mathbf{x}^{p}$ is correction which is solution of linear system at each p-th step:

$$\left(\mathbf{U}_p^T\mathbf{C}^{-1}\mathbf{U}_p\right)\Delta\mathbf{x}^{p} = \mathbf{U}_p^T\mathbf{C}^{-1}\left(\mathbf{f}\left(\mathbf{x}^{p}\right) - \mathbf{f}^*\right). \qquad [\,4\text{-}4\,]$$

where, $\mathbf{U_p}$ is the Jacobi matrix of the first derivatives ((sensitivity functions) in the near vicinity of the vector $\mathbf{x^p}$, $\mathbf{t_p}$– Levenberg-Marquardt multiplier [*Marquardt,* 1963] (if necessary the more sophisticated Levenberg-Marquardt type statistical correction can be included in the matrix

$\left(\mathbf{U}_p^T\mathbf{C}^{-1}\mathbf{U}_p\right)$, the details are given in is given in the paper *Dubovik and King* [2000]). This multiplier is used to provide monotonic convergence and it is typically smaller than 1(t_p<1).

The initial guess of the effective reflectivity and total ozone value is taken from the OMI ozone algorithm and the initial guess for SO_2 is taken from the standard DOAS fitting procedure of the OMI radiances in the UV2 spectral region. Then the iterations [4-3] are performed to improve the SO_2 solution. In order to control convergence the following residual should be controlled at each step:

$$\Psi\left(\mathbf{x}^p\right)=\left(\mathbf{f}\left(\mathbf{x}^p\right)-\mathbf{f}^*\right)^T\mathbf{C}^{-1}\left(\mathbf{f}\left(\mathbf{x}^p\right)-\mathbf{f}^*\right). \qquad [\,4\text{-}5\,]$$

If the condition $\Psi\left(\mathbf{x}^{p+1}\right)\leq\Psi\left(\mathbf{x}^{p+1}\right)$ is not satisfied then t_p should be decreased until the condition is satisfied. The iterations are needed to improve the solution and reduce the residual [4-5]. The convergence is satisfied when the SO_2 difference between iterations is less than a certain threshold value.

4.4. Error analysis

4.4.1. Checking consistency of the forward model with the measurements

The magnitude of the minimum of $\Psi(\mathbf{x})$ is not predefined and usually is used to estimate the variance of the measurements errors, σ^2, (for the simplest case of the covariance matrix: C = σ^2 I, I is the unity matrix). In case of uncorrelated random measurement errors, the residual, $\Psi(\mathbf{x})$, is distributed according to χ^2, i.e.

$$\Psi\left(\mathbf{x}^p\right)=\left(\mathbf{f}\left(\mathbf{x}^p\right)-\mathbf{f}^*\right)^T\mathbf{C}^{-1}\left(\mathbf{f}\left(\mathbf{x}^p\right)-\mathbf{f}^*\right)\approx(M-N)\,\sigma^2. \qquad [\,4\text{-}6\,]$$

Correspondingly, the variance of the measurement errors σ^2 can be estimated from the residual value:

$$\hat{\sigma}\approx\sqrt{\frac{\Psi\left(\mathbf{x}^p\right)}{\mathrm{M-N}}}. \qquad [\,4\text{-}7\,]$$

where M is the number of fitting wavelengths and N is the number of retrieved parameters (N=5 in our case). This estimate of the measurement error is also very useful for checking both the measurement error and consistency of forward model. Namely, for a reasonable fitting one should expect:

$$\sigma^2\sim\varepsilon^2 \qquad [\,4\text{–}8\,]$$

where ε^2 is anticipated measurement accuracy (measurement error variance). If the condition [4-8] is not met, the forward model is not consistent with the observational conditions. Thus, the control of the residual [4-7] is useful for an internal quality control of the retrieval.

4.4.2. Estimating retrieval error

The lookup tables can be also used for the estimation of the SO_2 retrieval noise due to random noise in the OMI measurements. Table 4.1 shows the calculated SO_2 noise (1σ SO_2) for different pairs of OMI channels from the following equation:

$$\sigma_{SO2}(\lambda_i,\lambda_j)=\frac{\sqrt{\dfrac{n_i^2}{S_i^2}+\dfrac{n_j^2}{S_j^2}}}{\gamma_i-\gamma_j} \qquad [\,4\text{-}9\,]$$

where $S_i = dN(\lambda_i)/d\Omega$ is sensitivity to ozone at wavelength λ_i, (known from Jacobi matrix of the first derivatives); $\gamma_i(H_S)$ is the sensitivity to SO_2, $dN(H_S,\lambda_i)/d\Sigma$, normalized to S_i (H_S is the SO_2 altitude), and n_i is 1/(signal-to-noise) of the OMI measurements.

Table 4.1 Estimated 1σ OMI SO_2 retrieval noise using different pairs of OMI spectral channels for conditions in Figure 4-2.

λ_2	λ_2	1σ SO_2 at 20km [DU]	1σ SO_2 at 1km [DU]
304.5	305.7	0.41	2.76
305.7	306.6	0.27	1.55
306.6	307.6	0.25	1.53
307.6	308.7	0.20	1.04
308.7	309.6	0.21	1.14
309.6	310.8	0.24	1.14
310.8	311.85	0.20	1.00
311.85	313.2	0.21	0.93
313.2	314.4	0.24	1.11
314.4	315.3	0.51	2.18
315.3	316.2	0.72	3.28
316.2	317.2	0.94	3.82
317.2	319.2	0.65	2.81
319.2	319.8	1.21	4.86
308.7	311.85	0.18	1.02
310.8	314.4	0.23	1.22
308.7	314.4	0.20	1.22
307.6	310.8	0.23	1.03
307.6	313.2	0.23	0.96

The typical 1σ SO_2 noise for a clear scene in one pixel is 0.2 DU if only 2 wavelengths are used and for an SO_2 layer at 20 km. The noise increases to 1DU if the SO2 layer at 1 km. The increase in retrieval noise results from the decrease in radiometric sensitivity with decrease in SO_2 plume height.

Using multiple OMI wavelengths reduces the radiometric noise compare to the case of just 2 wavelengths. The estimated covariance matrix of the retrieval error estimated in linear approximation is given by the following equation (see Dubovik et al. [2000]):

$$\mathbf{C}_{\hat{\mathbf{x}}} \approx \left(\mathbf{U}_{\mathrm{pf}}^{\mathrm{T}}\mathbf{C}^{-1}\mathbf{U}_{\mathrm{pf}}\right)^{-1}\hat{\sigma}^2 \qquad [\,4\text{-}10\,]$$

where p_f is the number of the last iteration, and σ^2 can be obtained from (4-7) or from the anticipated measurement accuracy (4-8). Application of equation (4-10) for the case of boundary layer SO_2 and uncorrelated and spectrally independent random noise in OMI measurements with signal-to-noise ratio of 300 provides the theoretical SO_2 error estimate of ~0.1DU (1σ SO_2 noise). This error estimate does not include any geophysical or instrumental biases that should be properly taken into account by the forward model [4-1].

4.4.3. Correction for Ring effect

The model *N* values in Equations [4-1] are corrected for the Ring effect using a pre-calculated lookup table. The Ring correction algorithm [*Joiner et al.,* 1995] will be applied to the entire spectrum, but will only include O_3 absorption. Figure 4.6 (left) shows the standard Ring correction [*J.Joiner and P.K. Bhartia, private communication*] in the SO_2 fitting window. Figure 4.6 (right) shows the additional correction due to SO_2 absorption [calculated by D. Flittner]. The additional Ring correction due to SO_2 up to 10 DU (maximum expected for non-volcanic sources) is small and one can use the standard Ring correction as a first approximation.

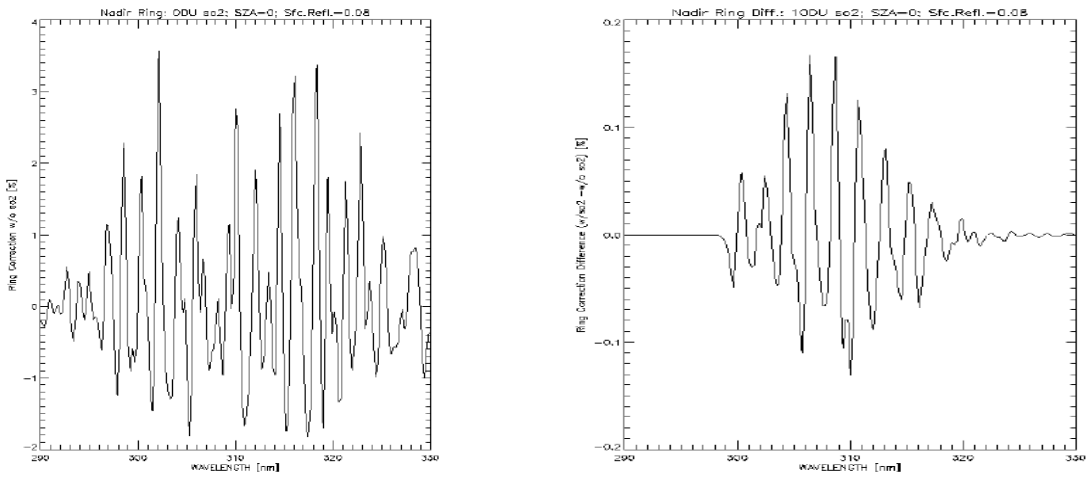

Figure 4.6 Ring correction in the SO_2 spectral fitting window: a) Standard Ring spectrum taking into account only ozone absorption and Rayleigh scattering; b) Additional correction due to 10 DU of SO_2. A triangular slit function with a FWHM = 0.45 nm was used for this calculation.

4.4.4. Correction for volcanic ash

Ash in volcanic clouds can produce overestimation in TOMS-like sulfur dioxide retrievals [*Krueger et al.*, 1995]. In the initial version of the SO_2 algorithm the ash/aerosol effects are treated implicitly through the effective reflectivity (a by-product of the OMI ozone algorithm) and coefficients of the quadratic correction term in (1). This will be changed in the volcanic SO_2 algorithm through the explicit radiative transfer modeling of the spectral dependence of the ash effect [*Krotkov et al.*, 1997a; *Krueger et al.*, 2000]. After initial ash parameters estimation using one of the methods described in [*Krotkov et al.*, 1999a,b], a new set of lookup tables with explicit inclusion of ash particles will be constructed for the specific volcanic cloud.

4.5. Outputs

Standard outputs include:

- Vertical column SO_2 and uncertainty
- Prescribed SO_2 layer height
- Fitting *rms*
- Convergence flags
- Total ozone

- Common OMI data:
  - Geolocation data
  - Solar zenith angle
  - Satellite zenith angle
  - Surface reflectivity
  - Cloud top height
- Version numbers of algorithm and parameter input file;

4.6. Validation

The OMI SO_2 algorithm performance will be confirmed through testing with synthetic radiances, and comparison with DOAS retrievals using GOME data.

The MK II Brewer spectrophotometer is designed to measure SO_2 and total ozone from direct sun irradiances at 5 near UV wavelengths. However, background SO_2 amounts are usually below the detection limit. Better stray light rejection in double monochromator MK III Brewer instruments may be adequate to measure amounts as small as 1 matm-cm. Seven double Brewers at Northern Hemisphere stations (one at the Goddard Laboratory for Atmospheres) are collecting data. A new direct sun spectral scan method appears capable of detecting sub matm-cm amounts (*J. Kerr*, private communication, 2001). If successful, this will be invaluable for validating background SO_2 amounts.

Validation of volcanic SO_2 cloud amounts depends on drift of the cloud over an observing station. Normally volcanic clouds drift too rapidly to schedule instrumented aircraft flights in their paths. Other satellite data can often provide supporting information or coincident observations to lend confidence in the retrievals.

4.7. References

Bluth G.J.S., C.C. Schnetzler, A.J. Krueger, and L.S. Walter, The contribution of explosive volcanism to global atmospheric sulfur dioxide concentrations, Nature 366, 327-329, 1993.

Bluth G.J.S., W.I. Rose, I.E. Sprod, and A.J. Krueger, Stratospheric loading of sulfur from explosive volcanic eruptions, J. Geol. 105, 671-683, 1997.

Burrows, J.P., K.V. Chance, A.P.H. Goede, R. Guzzi, B.J. Kerridge, C. Muller, D. Perner, U. Platt, J.-P. Pommereau, W. Schneider, R.J. Spurr, and H. van der Woerd, *Global Ozone Monitoring Experiment Interim Science Report*, ed. T. D. Guyenne and C. Readings, Report ESA SP-1151, ESA Publications Division, ESTEC, Noordwijk, The Netherlands, ISBN 92-9092-041-6, 1993.

Burrows, J.P., M.Weber, M. Buchwitz, V.V.Rosanov, A.Ladstatter, A. Weissenmayer, A.Richter, R.DeBeek, R.Hoogen,K. Bramstedt, and K.U. Eichmann, The Global Ozone Monitoring Experiment (GOME): Mission concept and first scientific results, *J. Atmos. Sci.,* 56, 151-175, 1999.

Chin, M., R.B.Rood, S-J. Lin, J-F. Muller, and A.M.Thompson, Atmospheric sulfur cycle simulated in the global model GOCART: Model description and global properties, *J. Geophys. Res.,* 105, 24671-24687, 2000

Dave, J.V. Multiple scattering in a non-homogeneous, Rayleigh atmosphere, J. Atmos. Sci. 22, 273-279, 1965.

De Vries, J., S/N status prediction, SE-OMIE-0437-FS/00, 2000.

Dubovik, O. and M. King, A flexible inversion algorithm for retrieval of aerosol optical properties from sun and sky radiance measurements, J. Geophys. Res. 105, 20,673-20,696, 2000.

Eisinger, M., and J.P. Burrows, Tropospheric sulfur dioxide observed by the ERS-2 GOME instrument, Geophys. Res. Lett. 25, 4177-4180, 1998.

Joiner, J., P.K. Bhartia, R.P. Cebula, E. Hilsenrath, R.D. McPeters, and H. Park, Rotational Raman scattering (Ring effect) in satellite backscatter ultraviolet measurements, *Appl. Opt.* 34, 4513-4525, 1995.

Joiner, J. and P.K. Bhartia, The determination of cloud top pressures from rotational-Raman scattering in satellite backscatter ultraviolet measurements, J. Geophys. Res. 100, 23,019-23,026, 1995.

Krotkov, N.A., A.J. Krueger, and P.K. Bhartia, Ultraviolet optical model of volcanic clouds for remote sensing of ash and sulfur dioxide, J. Geophys. Res. 102, 21,891-21,904, 1997.

Krotkov, N.A., O. Torres, C. Seftor, A.J. Krueger, A. Kostinski, W.I. Rose, G.J.S. Bluth, D. Schneider, and S.J. Schaefer, Comparison of TOMS and AVHRR volcanic ash retrievals from the August 1992 eruption of Mt. Spurr, Geophys. Res. Lett. 26, 455-458, 1999a.

Krotkov, N.A., D.E. Flittner, A.J. Krueger, A. Kostinski, C. Riley, W. Rose, and O. Torres, Effect of particle non-sphericity on satellite monitoring of drifting volcanic ash clouds, J. Quant. Spectrosc. Radiat. Transfer 63, 613-630, 1999b.

Krueger, A.J., Sighting of El Chichon sulfur dioxide clouds with the Nimbus 7 Total Ozone Mapping Spectrometer, Science 220, 1377-1379, 1983.

Krueger, A.J., L.S. Walter, P.K. Bhartia, C.C. Schnetzler, N. A. Krotkov, I. Sprod, and G.J.S. Bluth, Volcanic sulfur dioxide measurements from the Total Ozone Mapping Spectrometer instruments, J. Geophys. Res. 100, 14,057-14,076, 1995.

Krueger, A.J., S.J. Schaefer, N. Krotkov, G. Bluth, and S. Barker, Ultraviolet Remote Sensing of Volcanic Emissions, in *Remote Sensing of Active Volcanism*, ed. P. Mouginis Mark, J.A.

Crisp, and J. H. Fink, Geophysical Monograph 116, American Geophysical Union, Washington, DC, 2000.

Manatt, S.L. and A.L. Lane, A compilation of the absorption cross-sections of SO_2 from 106 to 403 nm, , J. Quant. Spectrosc. Radiat. Transfer, 50, 267-276, 1993.

McGee, T.J. and J.Burris Jr, SO_2 absorption cross sections in the near UV, J. Quant. Spectrosc. Radiat. Transfer, 37, 165-182, 1987.

Marquardt, D.L., An algorithm for least-squares estimation of non-linear parameters, J. Soc. Indust. Appl. Math. 2, 431-441, 1963.

5. BrO

K. Chance, T.P. Kurosu, and L.S. Rothman
Smithsonian Astrophysical Observatory
Cambridge, MA, USA

BrO was first measured from space by GOME, in the region 344-360 nm. While it was anticipated that BrO could be measured globally [*Chance et al.*, 1991], it was also thought that BrO would be of interest primarily as a stratospheric gas. However, lower tropospheric ozone destruction in the Arctic polar sunrise has been coupled with bromine chemistry associated with the ice pack [*Barrie et al.*, 1988]. ER-2 observations show the presence of enhanced BrO in the free troposphere during the Arctic polar sunrise [*McElroy et al.*, 1999], and GOME measurements have now confirmed and further quantified enhancements in BrO in both Arctic and Antarctic spring [*Wagner and Platt*, 1998]. Figure 5.1 shows an example of enhanced tropospheric BrO over the ice pack in the Northern hemisphere late spring in 1997. OMI measurements of BrO will make such observations at higher spatial resolution that, coupled with cloud determination, will permit the location and persistence of enhanced polar tropospheric BrO to be studied in synergy with tropospheric O_3 in order to quantify the effects on tropospheric O_3.

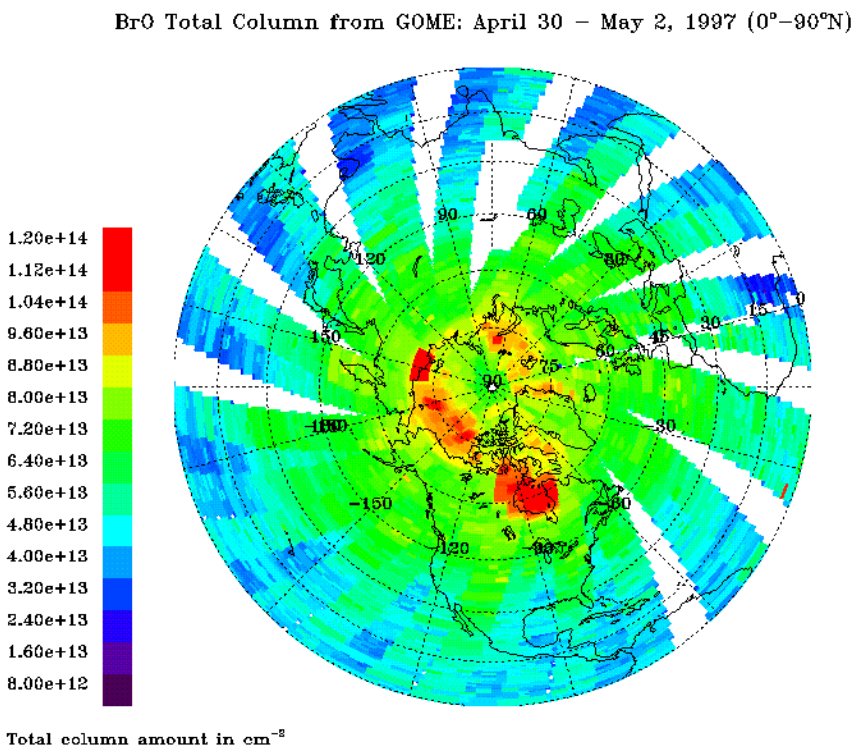

Figure 5.1 The distribution of BrO (vertical column in cm^{-2}) in the Northern hemisphere for April 30-May 2, 1997 [Chance, 1998]. Large enhancements, almost certainly due to tropospheric BrO, are obvious over several areas, including Hudson Bay and the Arctic ice shelf.

The higher spatial resolution of OMI will also permit detailed observations to be made of the relation of BrO to the polar vortex structure.

Absorptions for BrO are quite small (substantially less than 1% in most cases), so that they are optically thin to a high degree of accuracy and so that interferences from other causes (e.g., O_3 absorption and the Ring effect) must be accounted for very precisely. The fitting for BrO includes two major steps: (1) the fitting of a selected wavelength window of spectrum to determine the slant column density, N_{si}, for a particular species i, and (2) the determination of an appropriate air mass factor, M_i, to convert N_{si} to a vertical column density, N_{vi}:

$$M = N_{si} / N_{vi} , \qquad [\ 5\text{-}1\ ]$$

where M is a function of viewing geometry, geophysical condition (albedo, cloud coverage), and the vertical distribution of the gas. Generally, gas located at lower altitude contributes less to the satellite-measured absorption spectrum since Rayleigh scattering discriminates against its viewing [*Palmer et al.*, 2001]. Algorithms are designed assuming sequential processing of level 1 data products, including spectra, so that higher-level processing will be required in some cases to fully exploit the measurements. The first step is accomplished by a spectral fitting procedure, which will be optimized during the commissioning phase of the OMI instrument, and where various options described below are evaluated. The second step is more problematic for some conditions. BrO is normally predominantly located in the stratosphere and upper troposphere, and air mass factors pre-tabulated versus measurement geometry for nominal geophysical conditions and profile shape give results correct to within the uncertainties from step (1).

However, during the polar spring there are enhancements in tropospheric BrO [*Wagner and Platt*, 1998; *Richter et al.*, 1998; *Hegels et al.*, 1998; *Chance*, 1998]. For these, the *M*s calculated assuming stratospheric/upper troposphere BrO significantly underestimate the tropospheric concentration (by about a factor of two). It is anticipated that correction for these cases will occur in higher-level processing rather than dynamically as a part of the level 1-2 operation processing, since effective discrimination of these cases involves processing that is not sequential in analysis. Additionally, there is some evidence that free tropospheric concentrations of BrO may be larger than anticipated [*Fitzenberger et al.*, 2000]. If this proves to be the case, appropriate changes to the algorithm will be required in order to appropriately weight the contribution to the measured spectra from BrO at these altitudes.

5.1. Slant column measurements

The determination of slant column abundances, N_s, is accomplished by fitting the measured radiance I, beginning with the measured irradiance E, molecular absorption cross sections, correction for the Ring effect, effective albedo (which includes the contribution from Rayleigh scattering for these molecules, as discussed in **Air mass factors and vertical column abundances**, below), and a low-order polynomial for closure. This latter term accounts for small remaining differences in Rayleigh scattering versus wavelength over the fitting window, variation of ground albedo, and imperfect intensity calibration of the OMI radiance and irradiance measurements. The overall fitting strategy includes a number of options, which will be fully tested during OMI commissioning, with the ones that have proved most successful in the analysis of previous satellite measurements providing the baseline.

5.1.1. Nonlinear least-squares fitting

The Levenberg-Marquardt nonlinear least-squares fitting procedure (nlls) [*Marquardt*, 1963; *Press et al.*, 1986] is used in several of the subsequent steps in the analysis. In this procedure, the χ^2 merit function

$$\chi^2 = \sum_{i=1}^{N} \left[(y_i - F(x_i;a)) / \sigma_i \right]^2 \qquad [5\text{-}2]$$

is minimized with respect to the parameters *a*. The strategy for finding the minimum is to begin with a diagonally-dominant curvature matrix, corresponding to a steepest descent search procedure, and gradually changing continuously over to the inverse-Hessian (curvature) method search procedure as the minimum is neared.

Convergence is reached when χ^2 is less than a pre-set amount, when χ^2 decreases by less than a pre-set amount over several successive iterations, or when all parameters change by less than a pre-set fraction for several successive iterations. Iteration is also halted when the number of iterations reaches a pre-set maximum without successful convergence.

Estimated fitting uncertainties are given as $\sigma_i = \sqrt{C_{ii}}$, where *C* is the covariance matrix of the standard errors. This definition is strictly true only when the errors are normally distributed. In the case where the level-1 data product uncertainties are not reliable estimates of the actual uncertainties, spectral data are given unity weight over the fitting window, and the 1σ fitting error in parameter *i* is determined as

$$\sigma_i = \varepsilon_{rms} \sqrt{\frac{C_{ii}\ n_{points}}{n_{points} - n_{varied}}} \qquad [5\text{-}3]$$

where ε_{rms} is the root-mean-squared fitting residual, n_{points} is the number of points in the fitting window, and n_{varied} is the number of parameters varied during the fitting.

5.1.2. Re-calibration of wavelength scales

This is a baseline option, required by the fact that fitting to small root-mean-square differences between the measurements and the modeling (*rms*), comparable to the measurement signal-to-noise ratios (SNRs) requires better wavelength calibration than that provided in the level 1 data products (wavelength calibration for the specific fitting window is more accurate than that derived for the spectrum as a whole). The model for this procedure comes from the analysis of GOME data [*Caspar and Chance*, 1997; *Chance*, 1998]. The irradiance to be used in the subsequent spectrum fitting is re-calibrated in wavelength over the fitting window by nlls comparison to a high-resolution solar reference spectrum which is accurate in absolute vacuum wavelength to better than 0.001 nm [*Chance and Spurr*, 1997]. A slit width (instrument transfer function) parameter is fitted simultaneously. Radiance spectra are equivalently fitted, with the slit width parameter frozen to the values (versus CCD spectral field) determined in fitting the irradiance: Since the window regions for these four molecules are optically thin in all Telluric absorptions and contain only a few percent of inelastically-scattered Fraunhofer spectrum (Ring effect), the procedure works almost as well on radiances as on irradiances. Experience with GOME spectra (which are at higher spectral resolution) is that both are fitted to within about 1/50 spectral resolution element. Re-calibration normally involves only the determination of a single wavelength shift parameter for the fitting window (baseline option); inclusion of a wavelength ``squeeze" parameter is a non-baseline option. The case for OMI is complicated by the fact that such calibrations are made for the separate spectral fields on the CCD detector array (GOME has linear Reticon detectors, which measure single spectra).

Wavelength calibrations are made for each OMI orbit as follows:

1. The set of irradiances versus CCD position are calibrated in wavelength over the fitting window;
2. One set of radiances versus CCD position, selected by an input parameter, usually in the middle of the orbit, are calibrated in wavelength over the fitting window. This calibration is applied as the initial wavelength scale for all radiances in the orbit;
3. Further fine-tuning of the relative calibration of all radiances through the orbit to the irradiance is performed during the detailed spectrum fitting, as described below (baseline option).

5.1.3. Reference spectra

Reference spectra are degraded to the OMI resolution either in pre-tabulated form (baseline option) or using the parameterized slit function determined during the irradiance calibration (non-baseline option). They are then re-sampled to the radiance wavelength grid, using cubic spline interpolation [*Press et al.*, 1986]. The current baseline choices for reference spectra to fit BrO are shown in Figure 5.2:

- NO_2 cross sections *Vandaele et al.*, 1997.
- BrO cross sections *Wilmouth et al.*, 1999.
- OClO cross sections *Wahner et al.*, 1987 (corrected to vacuum wavelength).
- O_3 cross sections (needed to correct for spectral interference) *Burrows et al.*, 1999.
- O_2-O_2 collision complex *Greenblatt et al.*, 1990 (corrected to vacuum wavelength).
- Ring effect: Determined specifically for OMI applications by J. Joiner *et al.*
- Undersampling correction: Calculated dynamically, if required

Fitting of GOME spectra gave systematic residuals that were much larger than the absorption of the trace gases until it was discovered that these are due to spectral undersampling by the instrument. High frequency spectral information is aliased into the spectrum when irradiances are re-sampled to the radiance wavelength scale (irradiances for GOME, and for OMI, are measured at slightly different Doppler shifts with respect to the sun) [*Chance*, 1998; *Slijkhuis et al.*, 1999]. The algorithm for OMI includes a non-baseline option (since OMI is not anticipated to significantly undersample) for calculating undersampling corrections at the time of reference spectrum sampling. This is accomplished by taking the high-resolution Fraunhofer reference spectrum, convolved with the instrument transfer function (as determined during the irradiance spectral calibration), which constitutes an oversampled irradiance and forming properly-sampled and undersampled representations of it, using cubic spline interpolation. The difference between the representation is the undersampling correction; for GOME this constitutes ca. 90% of the systematic residual.

5.1.4. Common-mode correction

Remaining systematic residuals which are, by definition, uncorrelated to the trace gas spectra may be averaged and included in the spectrum fitting as a ``common-mode'' spectrum, to reduce the fitting *rms* and, proportionally, the fitting uncertainties. This is included as a non-baseline option for OMI. For GOME, this reduces the *rms* by about a factor of two for BrO and a factor of 3 for NO_2. The presumption is that the undersampling correction only imperfectly

models the instrument transfer function and thus leaves some remaining systematic effects. Comparisons with GOME measurements of NO_2 for clean maritime (mostly stratospheric NO_2) conditions show that this reduced uncertainty is the appropriate choice.

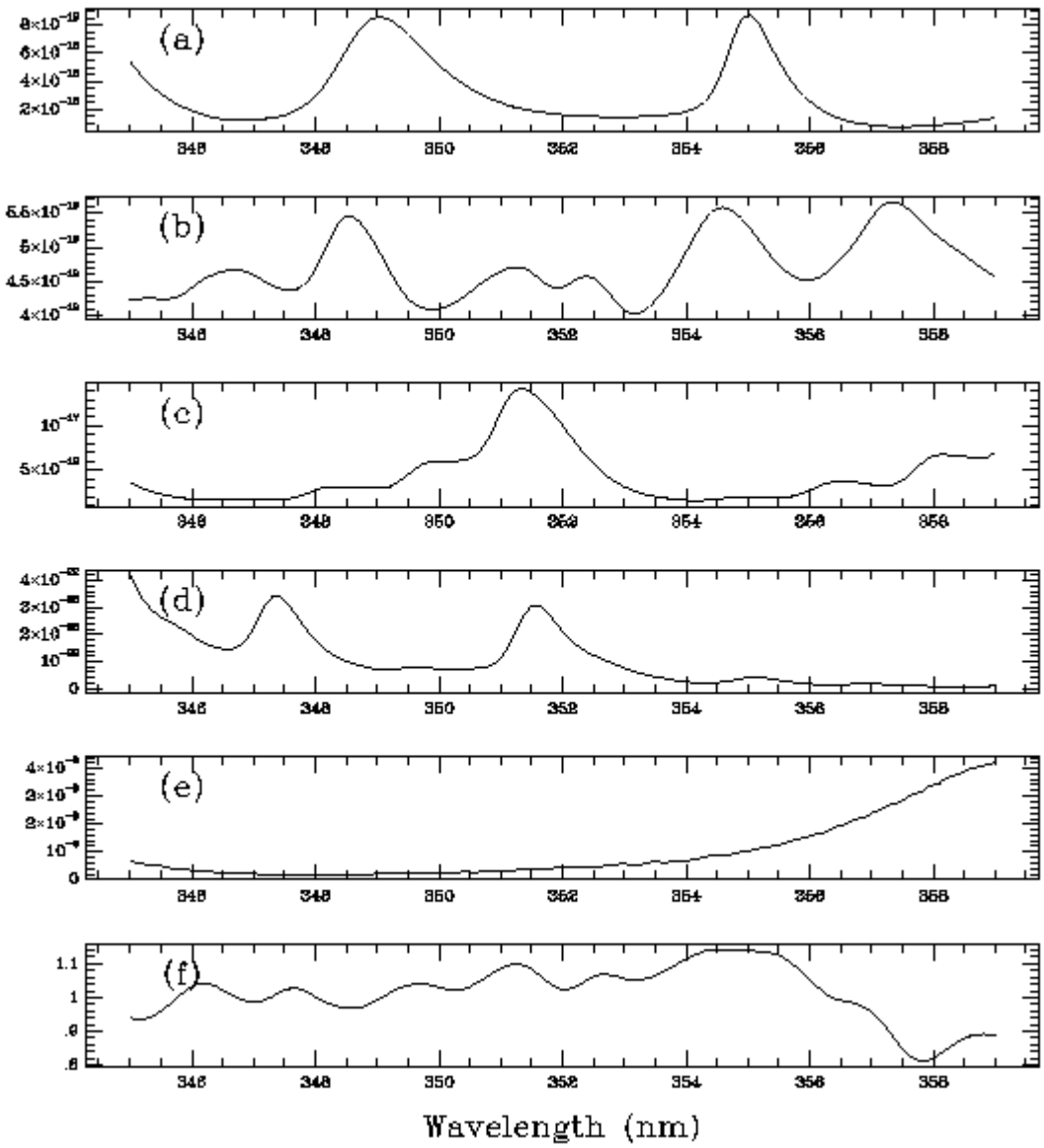

Figure 5.2 Reference spectra for fitting to determine slant column abundances of BrO: (a) BrO; (b) NO_2 (c) OClO; (d) O_3; (e) O_2-O_2 collision complex; (f) Ring effect.

5.1.5. Radiance fitting: BOAS (baseline option)

The radiance is nlls fitted to a modeled spectrum which includes the irradiance, and effective albedo, trace gas concentrations, Ring effect correction, and a low-order polynomial (up to cubic) closure term:

$$I(\lambda) = AE(\lambda)e^{-N_{s1}\sigma_1(\lambda)}\cdots e^{-N_{sn}\sigma_n(\lambda)} + c_R\sigma_R + c_0 + c_1(\lambda-\overline{\lambda}) + c_2(\lambda-\overline{\lambda})^2 + c_3(\lambda-\overline{\lambda})^3 \qquad [5\text{-}4]$$

The σ_i are the absorption cross sections, σ_R is the Ring effect correction, and the c_0 - c_3 are the coefficients of the closure polynomial. Each parameter may be individually selected to be varied during the fitting or frozen at a constant value. The baseline for BrO is to vary A, N_s

(BrO), N_s (NO_2), N_s (O_3), N_s (O_2-O_2), c_R, and $c_0 - c_3$. In addition, the linear wavelength scale of the irradiance is allowed to vary (baseline option) to correct for small wavelength changes in the radiance over the orbit. While it is actually the radiance scale that requires adjustment, the relative change in wavelength scale is much smaller than the instrument resolution or the variation of measurable features in the reference or Ring spectra: adjustment of the irradiance scale avoids changing the measured quantity (the radiance) during the fitting process. The baseline fitting window is 345-359 nm.

Smoothing (low-pass filtering) of the irradiances, radiances, and reference spectra is included as a non-baseline option. This procedure provides an alternate means to correct for spectral undersampling effects. It is implemented by applying a running 5-point filter (1/16, 1/4, 3/8, 1/4, 1/16) to each of the spectra.

Updating of the fitting parameters is included as a baseline option: For each spectrum after the first in a particular spectrum field of the CCD, the initial guesses for fitting parameters are updated to those fitted to the previous spectrum.

5.1.6. Radiance fitting: DOAS (non-baseline option)

This option converts the direct (BOAS) fitting of radiances to the DOAS method. The logarithm of the radiance divided by the irradiance is taken and the result high-pass filtered by the subtraction of a low-order polynomial (up to cubic, with the actual number of terms determined by the input parameter file):

$$H\left[ln(I/E)\right] = -N_{s1}H(\sigma_1) - \cdots - N_{sn}H(\sigma_n) + c_{R1}\,H(\sigma_{R1}/F) + c_{R2}\,H(\sigma_{R2}/F) + HOT, \qquad [5\text{-}5]$$

where H denotes high-pass filtering. The coefficients of the polynomial are determined by linear fitting to ln (I/E) [*Press et al.*, 1986]. Reference cross sections sampled at the OMI wavelength scale are also high pass filtered by subtraction of a low-order polynomial. The Ring effect correction is divided by the irradiance for each spectral field and the result high-pass filtered as well (note that this determines the first term in the expansion for the logarithmic quantity which includes the Ring effect; higher-order terms are not included - see Equation [1-4]). The fitting is then entirely analogous to the BOAS fitting, except that the fitted quantity is now H [ln (I/E)].

If the radiance/irradiance wavelength adjustment is not selected, then the DOAS fitting would be linear in the fitting parameters. However, since wavelength adjustment and BOAS fitting are both baseline options, it is not currently planned to implement separate linear fitting for this case; the additional computer time in fitting the linear case with the nonlinear method is inconsequential, and the results are virtually identical.

5.2. Air mass factors and vertical column abundances

Values of M are calculated versus viewing geometry and ground albedo using the LIDORT multiple scattering radiative transfer model [*Spurr et al.*, 2001]. LIDORT is designed to deliver both intensities and weighting functions. LIDORT solves the radiative transfer equation in a multi-layered atmosphere with multiple-scattering using the discrete ordinate method. The model contains a full internal perturbation analysis of the intensity field, allowing all weighting functions to be derived analytically to the same level of accuracy specified for the intensity. Although LIDORT has been designed primarily as a general forward model tool for non-linear atmospheric retrieval problems, the calculation of Ms is a straightforward application of the model. A single call to LIDORT will deliver both the top-of-the-atmosphere upwelling intensity I_B and the corresponding set of weighting functions $K(z)$ required for the M determination. In order to simplify the lookup process, the viewing geometry is parameterized by the effective solar zenith angle (*ESZA*), where $sec\ (ESZA) = sec\ (SZA) + sec\ (LOSZA) - 1$. *SZA*

is the solar zenith angle of the measurement and *LOSZA* is the line-of-sight zenith angle, and azimuthal dependence of *M* is ignored. Experience with fitting GOME data shows that, except for the highest solar zenith angles, above 80°, this procedure adds negligible additional error. BrO is assumed to be primarily in the stratosphere and upper troposphere, and is described by a Gaussian vertical concentration profile shape with a center at 19 km and a half width at 1/e intensity of 9 km (taken from *Brasseur and Solomon*, 1986). Calculations have been made for a range of albedo values from 0.01 to 1.0. Results for the albedo range 0.01 - 0.30 vary by less than 2% from those for albedo 0.1, so this is selected as the baseline. For albedo = 1.0, the error can be as large as 6%. Calculation for the long- and short-wavelength sides of the fitting window and the middle vary by less than 3%. An average of three values (long, short, and middle) is used for the tabulation of *M*s. A pre-calculated grid of *M* values versus *ESZA* is used in a lookup scheme where the individual *M*s are determined by cubic spline interpolation.

The variations of *M* with albedo and with wavelength over the fitting window are included as error terms. An additional *ESZA*-dependent error contribution of up to 5% is included to account for the variation of the profile of stratospheric/upper tropospheric BrO from the selected shape. The departure of *M* from the geometric value (1+sec (*ESZA*)) for stratospheric BrO is quite small, $\leq 3\%$ for values of *ESZA* up to 70°.

Correction for tropospheric BrO is not included in this algorithm. Identification of polar spring enhancements and correction to the *M*s for their analysis will take place in higher-level processing. Accounting for higher levels of free tropospheric BrO will await further confirmation of its existence.

5.3. Error estimates

Estimated errors are given for a ground footprint of $40 \cdot 40$ km^2, which has been adopted as the standard for reporting OMI error estimates within EOS. S/N values for estimating fitting uncertainties come from the OMI-EOS Instrument Specification Document RS-OMIE-0000-FS-021, Tables 5.5 and 5.6, and are applied to he best fitting knowledge from GOME analysis, taking into account the difference in spectral resolution. All uncertainties are given here as 1σ.

The 1σ fitting error in parameter *i* is determined as

$$\sigma_i = \sqrt{C_{ii}} \qquad [5\text{-}6]$$

or

$$\sigma_i = \varepsilon_{rms} \sqrt{\frac{C_{ii}\ n_{points}}{n_{points} - n_{varied}}}, \qquad [5\text{-}7]$$

As discussed in Section 5.1.1; both definitions include the contributions from correlation of fitted parameters. *C* is the covariance matrix of the standard errors. The published uncertainty of the absorption cross sections is added to this in quadrature to obtain the final slant column fitting uncertainties. The uncertainty in *M* is added in quadrature to obtain the final vertical column fitting uncertainties. The global average fitting uncertainty for BrO is 11%. The uncertainty in cross sections is 7%.

For stratospheric and upper tropospheric BrO, the uncertainty due to assuming a standard vertical profile shape is <1% for *ESZA* values up to 70° and <4% up to 80°. This includes error from albedo and cloud uncertainty, which is a minor contributor.

Total error for *ESZA* values up to 80°, assuming upper stratospheric and tropospheric BrO, is the quadrature sum of 11% + 7% + 4% = 14%. The error excluding the systematic

contribution from cross sections uncertainties is 12%, corresponding to $2.0 \cdot 10^{13}$ cm^{-2} vertical column density. This can be compared to the requirement in the Science Requirements Document for OMI-EOS (RS-OMIE-KNMI-001, Version 2) of 10^{13} cm^{-2}; meeting this requirement will require an improvement of a factor of 2 in the S/N over that given in the Instrument Specification Document.

The presence of substantial BrO lower in the troposphere and in the planetary boundary layer will require additional analysis in order to correctly quantify the abundance. In particular, the contribution to *M* from boundary layer BrO can easily be off by a factor of two from that derived with the present assumptions.

5.4. Outputs

Standard outputs include:

- Slant column abundance and 1σ fitting uncertainties for BrO and the other species varied in the fitting window;
- Correlation of other fitted species to BrO (from off-diagonal elements of the covariance matrix of the standard errors);
- Fitting *rms*;
- Convergence flags and number of iterations (successful? which convergence criterion?)
- Geolocation information;
- Version numbers of algorithm and parameter input file;
- Vertical column abundances and 1σ uncertainties.

5.5. Validation

Ground-based UV/visible BrO column measurements provide the primary validation source. ER-2 measurements of the upper tropospheric abundance as well as vertically-integrated OClO profiles from balloon-based UV/visible SAOZ instruments will also prove useful. Ground-based measurements should include high-latitude locations where conditions inside the polar vortex may be sampled and where enhanced boundary layer tropospheric BrO events occur.

5.6. References

Barrie, L.A., J.W. Bottenheim, R.C. Schnell, P.J. Crutzen, and R.A. Rasmussen, Ozone destruction and photochemical reactions at polar sunrise in the lower Arctic atmosphere, Nature 334, 138-141, 1988.

Brasseur, G, and S. Solomon, *Aeronomy of the Middle Atmosphere*, Second revised edition, ISBN 90-277-2343-5, D. Reidel, Dordrecht, 1986, p. 284.

Burrows, J.P., A. Richter, A. Dehn, B. Deters, S. Himmelmann, S. Voigt, and J. Orphal, Atmospheric remote sensing reference data from GOME - 2. Temperature-dependent absorption cross-sections of O_3 in the 231-794 nm range, J. Quant. Spectrosc. Radiat. Transfer 61, 509-517, 1999.

Caspar, C., and K. Chance, GOME wavelength calibration using solar and atmospheric spectra, *Proc. Third ERS Symposium on Space at the Service of our Environment*, Ed. T.-D. Guyenne and D. Danesy, European Space Agency publication SP-414, ISBN 92-9092-656-2, 1997.

Chance, K.V., J.P. Burrows, and W. Schneider, Retrieval and molecule sensitivity studies for the Global Ozone Monitoring Experiment and the SCanning Imaging Absorption spectroMeter for Atmospheric CHartographY, *Proc. S.P.I.E., Remote Sensing of Atmospheric Chemistry*, 1491, 151-165, 1991.

Chance, K., and R.J.D. Spurr, Ring Effect Studies: Rayleigh Scattering, Including Molecular Parameters for Rotational Raman Scattering, and the Fraunhofer Spectrum, Appl. Opt. 36, 5224-5230, 1997.

Chance, K., Analysis of BrO Measurements from the Global Ozone Monitoring Experiment, Geophys. Res. Lett. 25, 3335-3338, 1998.

Fitzenberger, R., H. Boesch, C. Camy-Peyret, M.P. Chipperfield, H. Harder, U. Platt, B.-M. Sinnhuber, T. Wagner, and K. Pfeilsticker, First profile measurements of tropospheric BrO, Geophys. Res. Lett. 27, 2921-2924, 2000.

Greenblatt, G.D., J.J. Orlando, J.B. Burkholder, and A.R. Ravishankara, Absorption measurements of oxygen between 330 and 1140 nm, J. Geophys. Res. 95, 18,577-18,582, 1990.

Hegels, E., P.J. Crutzen, T. Kluepfel, D. Perner, and J.P. Burrows, Global distribution of atmospheric bromine monoxide from GOME on Earth Observing Satellite ERS-2, Geophys. Res. Lett. 25, 3127-3130, 1998

Marquardt, D.L., An algorithm for least-squares estimation of non-linear parameters, J. Soc. Indust. Appl. Math. 2, 431-441, 1963.

McElroy, C.T., C.A. McLinden, and J.C. McConnell, Evidence for bromine monoxide in the free troposphere during the Arctic polar sunrise, Nature 397, 338-341, 1999.

Palmer, P.I., D.J. Jacob, K. Chance, R.V. Martin, R.J.D. Spurr, T.P. Kurosu, I. Bey, R. Yantosca, A. Fiore, and Q. Li, Air Mass Factor Formulation for Spectroscopic Measurements from Satellites: Application to Formaldehyde Retrievals from GOME, J. Geophys. Res. 106, 14,539-14,550, 2001.

Press, W.H., B.P. Flannery, S.A. Teukolsky, and W.T. Vetterling, *Numerical Recipes*, ISBN 0-521-30811-9, Cambridge University Press, 1986.

Richter, A., F. Wittrock, M. Eisinger, and J.P. Burrows, GOME observations of tropospheric BrO in northern hemisphere spring and summer 1997, Geophys. Res. Lett. 25, 2683-2686, 1998

Slijkhuis, S., A. von Bargen, W. Thomas, and K. Chance, Calculation of undersampling correction spectra for DOAS spectral fitting, *Proc. ESAMS'99 - European Symposium on Atmospheric Measurements from Space*, 563-569, 1999.

Spurr, R.J.D., T.P. Kurosu, and K. Chance, A linearized discrete ordinate radiative transfer model for atmospheric remote sensing retrieval, J. Quant. Spectrosc. Radiat. Transfer 68, 689-735, 2001.

Vandaele A.C., C. Hermans, P.C. Simon, M. Carleer, R. Colin, S. Fally, M.F. Mérienne, A. Jenouvrier, and B. Coquart, Measurements of the NO_2 absorption cross-section from 42000 cm^{-1} to 10000 cm^{-1} (238-1000 nm) at 220 K and 294 K, J. Quant. Spectrosc. Radiat. Transfer 59, 171-184, 1998.

Wagner, T., and U. Platt, Satellite mapping of enhanced BrO concentrations in the troposphere, Nature 395, 486-490, 1998.

Wahner, A., G.S. Tyndall, and A.R. Ravishankara, Absorption cross sections for OClO as a function of temperature in the wavelength range 240-480 nm, J. Phys. Chem. 91, 2734-2738, 1987.

Wilmouth, D.M., T.F. Hanisco, N.M. Donahue, and J.G. Anderson, Fourier transform ultraviolet spectroscopy of the $A\ ^2\Pi_{3/2} \leftarrow X\ ^2\Pi_{3/2}$ transition of BrO, J. Phys. Chem. 103, 8935-8945, 1999.

6. OClO

K. Chance, T.P. Kurosu, and L.S. Rothman
Smithsonian Astrophysical Observatory
Cambridge, MA, USA

OClO is a useful indicator for chlorine activation in the stratosphere. It was first measured from space by GOME, in the 363-393 nm range. To within current GOME measurement and retrieval uncertainties, it is found entirely within the polar vortices. Because of the high solar zenith angles associated with the occurrence, measurements to date have been limited to line-of-sight slant column measurements [*Wagner et al.*, 2001]. In addition to continuing the measurement record, providing an indicator for the trend in stratospheric chlorine loading, OMI will measure OClO at higher spatial resolution than GOME, which will help to elucidate the details of its formation, persistence, and correlation with PSCs and temperature.

Absorptions for OClO are quite small (substantially less than 1% in most cases), so that they are optically thin to a high degree of accuracy and so that interferences from other causes (e.g., O_3 absorption and the Ring effect) must be accounted for very precisely. The fitting for trace gases usually includes two major steps: (1) the fitting of a selected wavelength window of spectrum to determine the slant column density, N_{si}, for a particular species i, and (2) the determination of an appropriate air mass factor, M_i, to convert N_{si} to a vertical column density, N_{vi}:

$$M = N_{si} / N_{vi} , \qquad [\ 6\text{-}1\ ]$$

where M is a function of viewing geometry, geophysical condition (albedo, cloud coverage), and the vertical distribution of the gas. For OClO, the data products are slant column densities, so that this second step is not invoked. This is due to the fact that OClO is generally found at very high solar zenith angles, so that the determination of appropriate air mass factors for a given case requires substantial off-line analysis. The slant column determination is accomplished by a spectral fitting procedure, which will be optimized during the commissioning phase of the OMI instrument, and where various options described below are evaluated.

6.1. Slant column measurements

The determination of slant column abundances, N_s, is accomplished by fitting the measured radiance I, beginning with the measured irradiance E, molecular absorption cross sections, correction for the Ring effect, effective albedo, and a low-order polynomial for closure. This latter term accounts for small remaining differences in Rayleigh scattering versus wavelength over the fitting window, variation of ground albedo, and imperfect intensity calibration of the OMI radiance and irradiance measurements. The overall fitting strategy includes a number of options, which will be fully tested during OMI commissioning, with the ones that have proved most successful in the analysis of previous satellite measurements providing the baseline.

6.1.1. Nonlinear least-squares fitting

The Levenberg-Marquardt nonlinear least-squares fitting procedure (nlls) [*Marquardt*, 1963; *Press et al.*, 1986] is used in several of the subsequent steps in the analysis. In this procedure, the χ^2 merit function

$$\chi^2 = \sum_{i=1}^{N} \left[(y_i - F(x_i;a)) / \sigma_i \right]^2 \qquad [\,6\text{-}2\,]$$

is minimized with respect to the parameters a. The strategy for finding the minimum is to begin with a diagonally-dominant curvature matrix, corresponding to a steepest descent search procedure, and gradually changing continuously over to the inverse-Hessian (curvature) method search procedure as the minimum is neared.

Convergence is reached when χ^2 is less than a pre-set amount, when χ^2 decreases by less than a pre-set amount over several successive iterations, or when all parameters change by less than a pre-set fraction for several successive iterations. Iteration is also halted when the number of iterations reaches a pre-set maximum without successful convergence.

Estimated fitting uncertainties are given as $\sigma_i = \sqrt{C_{ii}}$, where C is the covariance matrix of the standard errors. This definition is strictly true only when the errors are normally distributed. In the case where the level-1 data product uncertainties are not reliable estimates of the actual uncertainties, spectral data are given unity weight over the fitting window, and the 1σ fitting error in parameter i is determined as

$$\sigma_i = \varepsilon_{rms} \sqrt{\frac{C_{ii}\ n_{points}}{n_{points} - n_{varied}}} \qquad [\,6\text{-}3\,]$$

where ε_{rms} is the root-mean-squared fitting residual, n_{points} is the number of points in the fitting window, and n_{varied} is the number of parameters varied during the fitting.

6.1.2. Re-calibration of wavelength scales

This is a baseline option, required by the fact that fitting to small root-mean-square differences between the measurements and the modeling (*rms*), comparable to the measurement SNRs requires better wavelength calibration than that provided in the level 1 data products (wavelength calibration for the specific fitting window is more accurate than that derived for the spectrum as a whole). The model for this procedure comes from the analysis of GOME data [*Caspar and Chance*, 1997; *Chance*, 1998]. The irradiance to be used in the subsequent spectrum fitting is re-calibrated in wavelength over the fitting window by nlls comparison to a high-resolution solar reference spectrum which is accurate in absolute vacuum wavelength to better than 0.001 nm [*Chance and Spurr*, 1997]. A slit width (instrument transfer function) parameter is fitted simultaneously. Radiance spectra are equivalently fitted, with the slit width parameter frozen to the values (versus CCD spectral field) determined in fitting the irradiance: Since the window regions for these four molecules are optically thin in all Telluric absorptions and contain only a few percent of inelastically-scattered Fraunhofer spectrum (Ring effect), the procedure works almost as well on radiances as on irradiances. Experience with GOME spectra (which are at higher spectral resolution) is that both are fitted to within about 1/50 spectral resolution element. Re-calibration normally involves only the determination of a single wavelength shift parameter for the fitting window (baseline option); inclusion of a wavelength "squeeze" parameter is a non-baseline option. The case for OMI is complicated by the fact that such calibrations are made for the separate spectral fields on the CCD detector array (GOME has linear Reticon detectors, which measure single spectra).

Wavelength calibrations are made for each OMI orbit as follows:

1. The set of irradiances, versus CCD position are calibrated in wavelength over the fitting window;
2. One set of radiances versus CCD position, selected by an input parameter, usually in the middle of the orbit, are calibrated in wavelength over the fitting window. This calibration is applied as the initial wavelength scale for all radiances in the orbit;
3. Further fine-tuning of the relative calibration of all radiances through the orbit to the irradiance is performed during the detailed spectrum fitting, as described below (baseline option).

6.1.3. Reference spectra

Reference spectra are degraded to the OMI resolution either in pre-tabulated form (baseline option) or using the parameterized slit function determined during the irradiance calibration (non-baseline option). They are then re-sampled to the radiance wavelength grid, using cubic spline interpolation [*Press et al.*, 1986]. The current baseline choices for reference spectra to fit OClO are Shown in Figure 6.1:

- NO_2 cross sections *Vandaele et al.*, 1997.
- BrO cross sections *Wilmouth et al.*, 1999.
- OClO cross sections *Wahner et al.*, 1987 (corrected to vacuum wavelength).
- O_3 cross sections (needed to correct for spectral interference) *Burrows et al.*, 1999.
- O_2-O_2 collision complex *Greenblatt et al.*, 1990 (corrected to vacuum wavelength).
- Ring effect: Determined specifically for OMI applications by J. Joiner *et al.*
- Undersampling correction: Calculated dynamically, if required

Fitting of GOME spectra gave systematic residuals that were much larger than the absorption of the trace gases until it was discovered that these are due to spectral undersampling by the instrument. High frequency spectral information is aliased into the spectrum when irradiances are re-sampled to the radiance wavelength scale (irradiances for GOME, and for OMI, are measured at slightly different Doppler shifts with respect to the sun) [*Chance*, 1998; *Slijkhuis et al.*, 1999]. The algorithm for OMI includes a non-baseline option (since OMI is not anticipated to significantly undersample) for calculating undersampling corrections at the time of reference spectrum sampling. This is accomplished by taking the high-resolution Fraunhofer reference spectrum, convolved with the instrument transfer function (as determined during the irradiance spectral calibration), which constitutes an oversampled irradiance and forming properly-sampled and undersampled representations of it, using cubic spline interpolation. The difference between the representation is the undersampling correction; for GOME this constitutes ca. 90% of the systematic residual.

6.1.4. Common-mode correction

Remaining systematic residuals which are, by definition, uncorrelated to the trace gas spectra may be averaged and included in the spectrum fitting as a ``common-mode" spectrum, to reduce the fitting *rms* and, proportionally, the fitting uncertainties. This is included as a non-baseline option for OMI. For GOME, this reduces the *rms* by about a factor of two for BrO and a factor of 3 for NO_2. The presumption is that the undersampling correction only imperfectly models the instrument transfer function and thus leaves some remaining systematic effects.

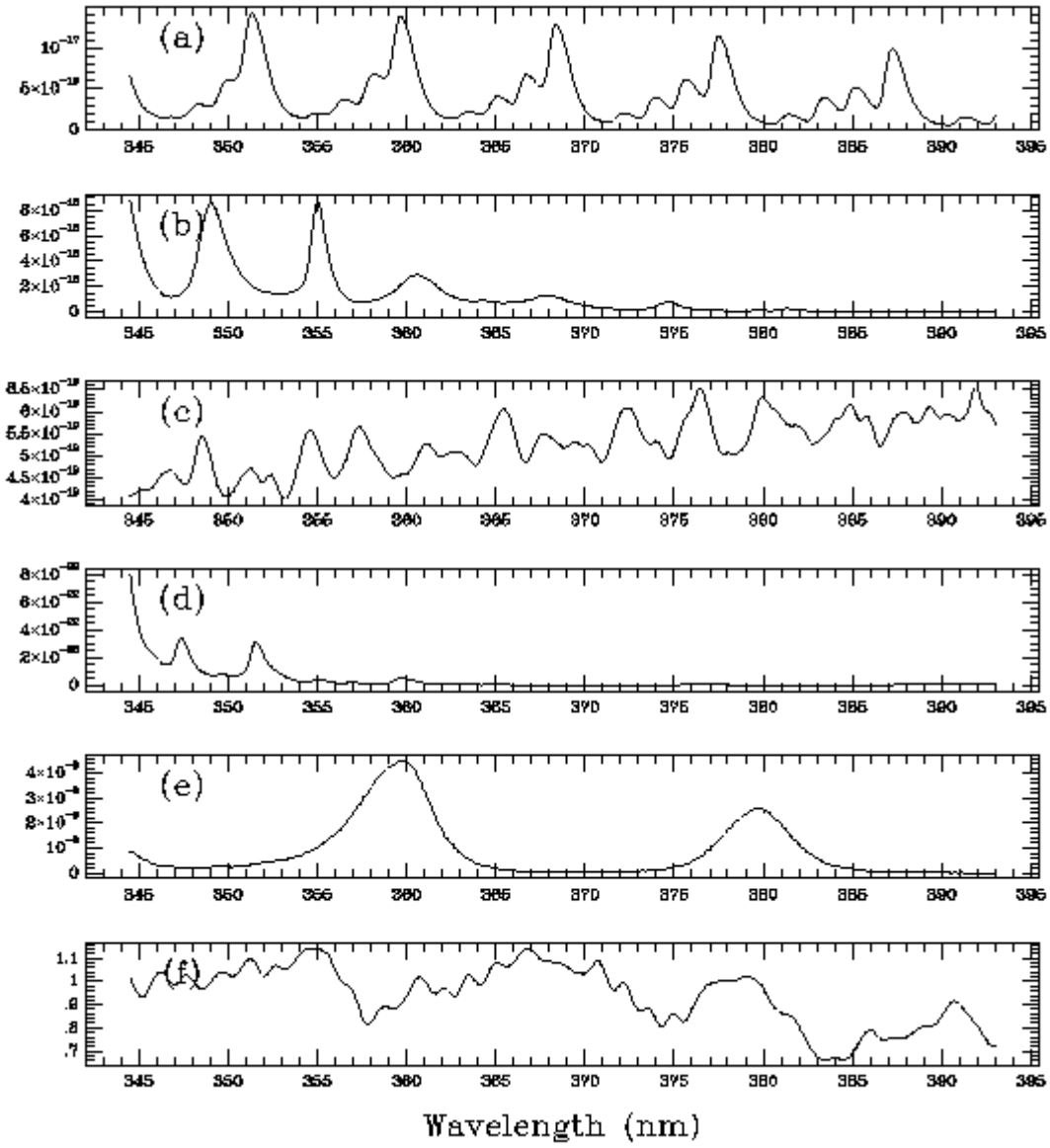

Figure 6.1 Reference spectra for fitting to determine slant column abundances of OClO: (a) OClO; (b) BrO; (c) NO_2; (d) O_3; (e) O_2-O_2 collision complex; (f) Ring effect.

Comparisons with GOME measurements of NO_2 for clean maritime (mostly stratospheric NO_2) conditions show that this reduced uncertainty is the appropriate choice.

6.1.5. Radiance fitting: BOAS (baseline option)

The radiance is nlls fitted to a modeled spectrum which includes the irradiance, and effective albedo, trace gas concentrations, Ring effect correction, and a low-order polynomial (up to cubic) closure term:

$$I(\lambda) = AE(\lambda)e^{-N_{s1}\sigma_1(\lambda)}\cdots e^{-N_{sn}\sigma_n(\lambda)} + c_R\sigma_R + c_0 + c_1(\lambda-\bar{\lambda}) + c_2(\lambda-\bar{\lambda})^2 + c_3(\lambda-\bar{\lambda})^3 \qquad [6\text{-}4]$$

The σ_i are the absorption cross sections, σ_R is the Ring effect correction, and the c_0 - c_3 are the coefficients of the closure polynomial. Each parameter may be individually selected to be varied during the fitting or frozen at a constant value. The baseline for OClO is to vary A, N_s (OClO), N_s

(BrO), N_s (NO_2), N_s (O_3), N_s (O_2-O_2), c_R, and $c_0 - c_3$. In addition, the linear wavelength scale of the irradiance is allowed to vary (baseline option) to correct for small wavelength changes in the radiance over the orbit. While it is actually the radiance scale that requires adjustment, the relative change in wavelength scale is much smaller than the instrument resolution or the variation of measurable features in the reference or Ring spectra: adjustment of the irradiance scale avoids changing the measured quantity (the radiance) during the fitting process. The baseline fitting window is 344.5-393 nm. Additionally, there is a baseline option to only fit spectra where *SZA* and latitude are within pre-set limits.

Smoothing (low-pass filtering) of the irradiances, radiances, and reference spectra is included as a non-baseline option. This procedure provides an alternate means to correct for spectral undersampling effects. It is implemented by applying a running 5-point filter (1/16, 1/4, 3/8, 1/4, 1/16) to each of the spectra.

Updating of the fitting parameters is included as a baseline option: For each spectrum after the first in a particular spectrum field of the CCD, the initial guesses for fitting parameters are updated to those fitted to the previous spectrum.

6.1.6. Radiance fitting: DOAS (non-baseline option)

This option converts the direct (BOAS) fitting of radiances to the DOAS method. The logarithm of the radiance divided by the irradiance is taken and the result high-pass filtered by the subtraction of a low-order polynomial (up to cubic, with the actual number of terms determined by the input parameter file):

$$H\left[ln(I/E)\right] = -N_{s1}H(\sigma_1) - \cdots - N_{sn}H(\sigma_n) + c_{R1}H(\sigma_{R1}/F) + c_{R2}H(\sigma_{R2}/F) + HOT, \qquad [6\text{-}5]$$

where H denotes high-pass filtering. The coefficients of the polynomial are determined by linear fitting to ln (I/E) [*Press et al.*, 1986]. Reference cross sections sampled at the OMI wavelength scale are also high pass filtered by subtraction of a low-order polynomial. The Ring effect correction is divided by the irradiance for each spectral field and the result high-pass filtered as well (note that this determines the first term in the expansion for the logarithmic quantity which includes the Ring effect; higher-order terms are not included - see Equation [1-4]). The fitting is then entirely analogous to the BOAS fitting, except that the fitted quantity is now H [ln (I/E)].

If the radiance/irradiance wavelength adjustment is not selected, then the DOAS fitting would be linear in the fitting parameters. However, since wavelength adjustment and BOAS fitting are both baseline options, it is not currently planned to implement separate linear fitting for this case; the additional computer time in fitting the linear case with the nonlinear method is inconsequential, and the results are virtually identical.

6.2. Air mass factors and vertical column abundances

It is not currently planned to implement these for OClO.

6.3. Error estimates

Estimated errors are given for a ground footprint of 40·40 km^2, which has been adopted as the standard for reporting OMI error estimates within EOS. S/N values for estimating fitting uncertainties come from the OMI-EOS Instrument Specification Document RS-OMIE-0000-FS-021, Tables 5.5 and 5.6, and are applied to he best fitting knowledge from GOME analysis, taking into account the difference in spectral resolution. All uncertainties are given here as 1σ.

The 1σ fitting error in parameter i is determined as

$$\sigma_i = \sqrt{C_{ii}} \qquad [\ 6\text{-}6\ ]$$

or

$$\sigma_i = \varepsilon_{rms} \sqrt{\frac{C_{ii}\ n_{points}}{n_{points} - n_{varied}}}, \qquad [\ 6\text{-}7\ ]$$

As discussed in Section 6.1.1; both definitions include the contributions from correlation of fitted parameters. *C* is the covariance matrix of the standard errors. The published uncertainty of the absorption cross sections are added to this in quadrature to obtain the final slant column fitting uncertainties. The average fitting uncertainty for OClO in enhanced, polar vortex concentrations is 9%. The uncertainty in cross sections is 10%. The total slant column uncertainty is then the quadrature sum: 9% + 10% = 13%.

The error excluding the systematic contribution from cross sections uncertainties is 9%, corresponding to $9 \cdot 10^{12}$ cm^{-2} slant column density. This can be compared to the requirement in the Science Requirements Document for OMI-EOS (RS-OMIE-KNMI-001, Version 2) of 10^{13} cm^{-2} vertical column density; performance as specified by the Instrument Specification Document is adequate to obtain the science requirement.

6.4. Outputs

Standard outputs include:

- Slant column abundance and 1σ fitting uncertainties for OClO and the other species varied in the fitting window;
- Correlation of other fitted species to OClO (from off-diagonal elements of the covariance matrix of the standard errors);
- Fitting *rms*;
- Convergence flags and number of iterations (successful? which convergence criterion?)
- Geolocation information;
- Version numbers of algorithm and parameter input file.

6.5. Validation

Ground-based UV/visible OClO column measurements provide the primary validation source. Vertically-integrated OClO profiles from balloon-based UV/visible SAOZ instruments will also prove useful. Ground-based measurements must be from high-latitude locations where conditions inside the polar vortex may be sampled.

6.6. References

Burrows, J.P., A. Richter, A. Dehn, B. Deters, S. Himmelmann, S. Voigt, and J. Orphal, Atmospheric remote sensing reference data from GOME - 2. Temperature-dependent absorption cross-sections of O_3 in the 231-794 nm range, J. Quant. Spectrosc. Radiat. Transfer 61, 509-517, 1999.

Caspar, C., and K. Chance, GOME wavelength calibration using solar and atmospheric spectra, *Proc. Third ERS Symposium on Space at the Service of our Environment*, Ed. T.-D. Guyenne and D. Danesy, European Space Agency publication SP-414, ISBN 92-9092-656-2, 1997.

Chance, K., and R.J.D. Spurr, Ring Effect Studies: Rayleigh Scattering, Including Molecular Parameters for Rotational Raman Scattering, and the Fraunhofer Spectrum, Appl. Opt. 36, 5224-5230, 1997.

Chance, K., Analysis of BrO Measurements from the Global Ozone Monitoring Experiment, Geophys. Res. Lett. 25, 3335-3338, 1998.

Greenblatt, G.D., J.J. Orlando, J.B. Burkholder, and A.R. Ravishankara, Absorption measurements of oxygen between 330 and 1140 nm, J. Geophys. Res. 95, 18,577-18,582, 1990.

Marquardt, D.L., An algorithm for least-squares estimation of non-linear parameters, J. Soc. Indust. Appl. Math. 2, 431-441, 1963.

Press, W.H., B.P. Flannery, S.A. Teukolsky, and W.T. Vetterling, *Numerical Recipes*, ISBN 0-521-30811-9, Cambridge University Press, 1986.

Slijkhuis, S., A. von Bargen, W. Thomas, and K. Chance, Calculation of undersampling correction spectra for DOAS spectral fitting, *Proc. ESAMS'99 - European Symposium on Atmospheric Measurements from Space*, 563-569, 1999.

Vandaele A.C., C. Hermans, P.C. Simon, M. Carleer, R. Colin, S. Fally, M.F. Mérienne, A. Jenouvrier, and B. Coquart, Measurements of the NO_2 absorption cross-section from 42000 cm^{-1} to 10000 cm^{-1} (238-1000 nm) at 220 K and 294 K, J. Quant. Spectrosc. Radiat. Transfer 59, 171-184, 1998.

Wagner, T., C. Leue, K. Pfeilsticker, and U. Platt, Monitoring of the stratospheric chlorine activation by Global Ozone Monitoring Experiment (GOME) OClO measurements in the austral and boreal winters 1995 through 1999, J. Geophys. Res. 106, 4971-4986, 2001.

Wahner, A., G.S. Tyndall, and A.R. Ravishankara, Absorption cross sections for OClO as a function of temperature in the wavelength range 240-480 nm, J. Phys. Chem. 91, 2734-2738, 1987.

Wilmouth, D.M., T.F. Hanisco, N.M. Donahue, and J.G. Anderson, Fourier transform ultraviolet spectroscopy of the $A\ ^2\Pi_{3/2} \leftarrow X\ ^2\Pi_{3/2}$ transition of BrO, J. Phys. Chem. 103, 8935-8945, 1999.